

# Resolution and calibration effects in high contrast polarimetric imaging of circumstellar scattering regions

H.M. Schmid<sup>1</sup>, and J. Ma<sup>2</sup>

<sup>1</sup> ETH Zurich, Institute for Particle Physics and Astrophysics, Wolfgang-Pauli-Strasse 27, CH-8093 Zurich, Switzerland  
e-mail: schmid@astro.phys.ethz.ch

<sup>2</sup> Univ. Grenoble Alpes, CNRS, IPAG, F-38000 Grenoble, France

Received ...; accepted ...

## ABSTRACT

**Context.** Many circumstellar dust scattering regions have been detected and investigated with polarimetric imaging. However, the quantitative determination of the intrinsic polarization and of dust properties is difficult because of complex observational effects.

**Aims.** This work investigates instrumental convolution and polarimetric calibration effect for high contrast imaging polarimetry with the aim to define measuring parameters and calibration procedures for accurate measurements of the circumstellar polarization.

**Methods.** We simulate the instrumental convolution and polarimetric cancellation effects for two axisymmetric point spread functions (PSF), a Gaussian PSF<sub>G</sub> and an extended PSF<sub>AO</sub> typical for a modern adaptive optics system, both with the same diameter  $D_{\text{PSF}}$  for the PSF peak. Further, polarimetric zero-point corrections (zp-corrections) are simulated for different cases like coronagraphic observations or systems with barely resolved circumstellar scattering regions.

**Results.** The PSF convolution reduces the integrated azimuthal polarization  $\Sigma Q_\phi$  for the scattering region while the net Stokes signals  $\Sigma Q$  and  $\Sigma U$  are not changed. For non-axisymmetric systems a spurious  $U_\phi$ -signal is introduced. These effects are strong for compact systems and for the convolution with an extended PSF<sub>AO</sub>. Compact scattering regions can be detected down to an inner working angle of  $r \approx D_{\text{PSF}}$  based on the presence of a net  $\Sigma Q_\phi$  signal. Unresolved central scattering regions can introduce a central Stokes  $Q$ ,  $U$  signal which can be used to constrain the scattering geometry even at separations  $r < D_{\text{PSF}}$ . The smearing by the halo of the PSF<sub>AO</sub> produces an extended, low surface brightness polarization signal. These effects change the angular distribution of the azimuthal polarization  $Q_\phi(\phi)$ , but the initial  $Q_\phi(\phi)$ -signal can be recovered partly with the analysis of measured Stokes  $Q$  and  $U$  quadrant pattern. A polarimetric zp-correction applied for the removal of offsets from instrumental or interstellar polarization depends on the selected reference region and can introduce strong bias effects for  $\Sigma Q$  and  $\Sigma U$  and the azimuthal distribution of  $Q_\phi(\phi)$ . Strategies for the zp-correction are described for different data types, like coronagraphic data or observations of partly unresolved systems. These procedures provide polarization parameter which can be reproduced easily with model simulations.

**Conclusions.** The simulations describe observational effects for imaging polarimetry in a systematic way, and they show when these effects are strong, and how they can be considered in the analysis. This defines suitable measuring parameters and procedures for the quantitative characterization of the intrinsic polarization of circumstellar scattering regions.

**Key words.** Techniques: polarimetric – high angular resolution – Stars: circumstellar matter – disks – scattering – dust

## 1. Introduction

Dust in circumstellar disks around young stars or dust in shells around red giants has been recognized in many systems as infrared excess in the spectral energy distribution. This dust plays an important role in the formation of stars and planetary systems (Birnstiel 2024), or the mass loss of evolved stars and the dust enrichment of the interstellar medium (Ferrarotti & Gail 2006).

In the last decade a lot of new information on circumstellar dust has been obtained with imaging observations of scattered stellar light in the near-IR and visual wavelength range. High-contrast instruments at large ground based telescopes achieve an angular resolution of up to 20 mas and this provides important information about the geometric distribution and the scattering properties of the circumstellar dust. In particular, the new information from scattered light observations is complementary to the extensive data already available from IR observations of the thermal emission of the dust around protoplanetary disks (e.g., Woitke et al. 2019), debris disk (e.g., Hughes et al. 2018; Chen et al. 2014), and red giants (e.g., Höfner & Olofsson 2018).

The detection of the scattered intensity from circumstellar dust is difficult because of the strong glare of the central star. This requires a careful separation of the stellar signal from the circumstellar signal, which can be achieved with high contrast techniques using space telescopes like HST (e.g., Kalas et al. 2013; Schneider et al. 2014; Zhou et al. 2023) or JWST (e.g., Gáspár et al. 2023; Lawson et al. 2023) or with ground based telescopes using adaptive optics (AO) systems (e.g., Milli et al. 2017; Ren et al. 2023).

High resolution imaging polarimetry is a very powerful method to separate the circumstellar polarization signal introduced by dust scattering from the direct light of the bright central source, which has usually no or only a small net linear polarization (e.g., Kuhn et al. 2001; Quanz et al. 2011). Large progress has been achieved with new instruments for imaging polarimetry in combination with AO systems at large ground based telescopes, including Subaru CIAO, HiCIAO and SCExAO instruments (Murakawa et al. 2004; Hodapp et al. 2008; Lucas et al. 2024), Gemini GPI (Perrin et al. 2015), and VLT NACO and SPHERE (Lenzen et al. 2003; Beuzit et al. 2019). Polarimetric

imaging of many objects has been obtained, including protoplanetary disks (e.g., Avenhaus et al. 2018; Benisty et al. 2023, and references therein), debris disks (e.g., Esposito et al. 2020; Crotts et al. 2024), circumstellar shells around red giants (e.g., Ohnaka et al. 2016; Khouri et al. 2020; Montargès et al. 2023), and post-AGB stars (e.g., Andrych et al. 2023).

High resolution imaging polarimetry is a quite new and not so simple observing technique because of PSF smearing and polarization cancellation effects, and noise in the weak differential signal (Schmid et al. 2006; Schmid 2022). In addition the polarimetric calibration of the complex high contrast imaging systems has to be considered (e.g. Tinbergen 2007; Schmid et al. 2018; de Boer et al. 2020; van Holstein et al. 2020) including the temporal PSF variations for ground based observations using AO systems (Tschudi & Schmid 2021; Ma et al. 2023). Despite this, many impressive results on the dust scattering geometry has been obtained, but for most objects no detailed analysis of the polarized intensity was attempted, mostly because this was not the focus of the study. For some special cases the polarized flux is derived more accurately to constrain the properties of the scattering dust, for example for extended circumstellar disks (Stolker et al. 2016; Monnier et al. 2019; Milli et al. 2019; Arriaga et al. 2020; Hunziker et al. 2021), axisymmetric systems (Pinilla et al. 2018; Tschudi & Schmid 2021; Ma et al. 2023), edge-on debris disks (e.g., Graham et al. 2007; Engler et al. 2017). It is highly desirable that such detailed studies on the circumstellar polarization are applied to a larger sample and are further improved for some key objects.

Accurate polarimetric measurements for circumstellar scattering regions require a good understanding of the observational aspects. Convolution effects degrade the measurable polarization signal as described for some cases in Schmid et al. (2006), Avenhaus et al. (2017), Heikamp & Keller (2019), Tschudi & Schmid (2021), and Ma et al. (2023, 2024b). Additional issues are polarization offsets introduced by instrumental effects, interstellar polarization, or an intrinsically polarized central star. These offsets can be eliminated with a polarimetric normalization, which sets the polarization for a certain region to zero (Quanz et al. 2011; Avenhaus et al. 2014). We call this procedure hereafter polarimetric zero-point correction (zp-correction).

A very useful and frequently used way to described the circumstellar signal is the azimuthal polarization  $Q_\phi$  (Schmid et al. 2006; Quanz et al. 2013). A convolution or an offset by a zp-correction introduces for  $Q_\phi$  quite complex changes and some of these effects have not been described in detail or have not been investigated at all. For example, it is clear that polarimetric offsets, or a zp-correction, change the polarization signal, but this work describes for the first time how this affects the azimuthal distribution of the circumstellar  $Q_\phi$  signal. Because of the lack of a systematic study, it is also difficult to extrapolate findings from the papers cited above to a more general picture.

For compact scattering regions near the star the mentioned effects are much stronger and they must even be considered for a qualitative interpretation of the polarization signal. Therefore, the scattering regions at small separations to the star  $r \lesssim 5 \lambda/D$ , or  $r \lesssim 200$  mas for large telescopes with AO systems, are often disregarded despite the fact that these regions are scientifically very interesting. They correspond for protoplanetary disks at  $\approx 100$  pc to the innermost  $< 20$  AU, where planets form (e.g., Birnstiel 2024) and for nearby red giant stars to a separation of a few stellar radii where dust particles condensate (e.g., Höfner & Olofsson 2018). In non-coronagraphic and non-saturated data, this region is sometimes masked in the data reduction process, because it looks "noisy", or shows an unexplained polarization

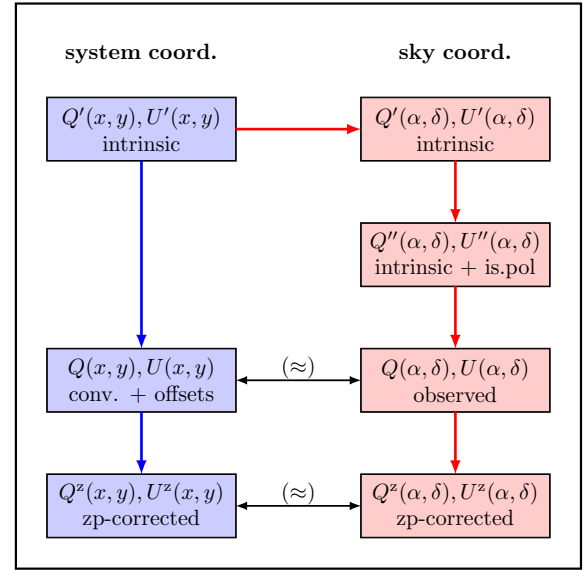


**Fig. 1.** Block diagram with the simplified description of the simulated imaging polarimetry given in blue. The red arrows show the full imaging process from the intrinsic model, the on-sky model including interstellar polarization, to the observed and possibly zp-corrected polarization signal.

pattern. However, these features might just be caused by a polarization offset or a convolution effect.

In coronagraphic observations the central region is hidden behind the focal plane mask to achieve more sensitive observations for the polarization signal further out. Also for this type of data, it is important to understand the impact of the convolution and of polarization offsets.

This work presents model simulations and a parameter framework for a systematic description of the PSF convolution effects and an investigation of the polarimetric offsets introduced by the instrument, the interstellar polarization, the central star, or by the zp-correction applied to the data. The results should provide a better understanding of these effects for the interpretation of observational results, and be useful for the definition of observing and measuring strategies for polarimetric imaging of circumstellar scattering regions.

This paper is organized as follows. The next section describes the model simulation and introduces the used polarimetric parameters. Section 3 describes the degradation of the scattering polarization by the PSF convolution for axisymmetric circumstellar scattering regions and for inclined disk models. The polarimetric calibration and zp-correction effects are investigated in Sect. 4, and discussed for coronagraphic observation and for data of partially resolved circumstellar scattering region. In Sect. 5 the results are summarized and discussed in the context of observational data. Detailed information, in particular numerical results for the presented simulations, are given in the appendix.

## 2. Model calculations

The block diagram in Fig. 1 gives an overview of the steps involved in imaging polarimetry using the Stokes  $Q = I_0 - I_{90}$  and  $U = I_{45} - I_{135}$  polarization parameters as example. The full process is described by the boxes connected with red arrows, from the intrinsic polarization model defined in system coordinates  $Q'(x, y), U'(x, y)$ , to the model in sky co-

ordinates  $Q'(\alpha, \delta), U'(\alpha, \delta)$ , including the contribution of interstellar polarization  $Q''(\alpha, \delta), U''(\alpha, \delta)$ , the observed signal  $Q(\alpha, \delta), U(\alpha, \delta)$ , and the result after a possible polarimetric zp-correction  $Q^z(\alpha, \delta), U^z(\alpha, \delta)$ . This is simplified in the simulations according to the blue path in Fig. 1 by calculating the observed polarization signal in system coordinates  $Q(x, y), U(x, y)$  considering only convolution and polarimetric offsets, and a zp-correction  $Q^z(x, y), U^z(x, y)$  for the calibration of the data. This approach still considers many of the key aspects of polarimetric imaging, but disregards second order effects and particular problems of individual instruments or data sets. The parameters for the  $x, y$ -coordinates are used for the description of the model simulations the  $x, y$ -coordinates, while some general polarimetric principle are discussed for on sky parameters using  $(\alpha, \delta)$ -coordinates. However, it is important to be aware of simplifying assumptions outlined in Fig. 1 for the interpretation of the model results.

## 2.1. Intrinsic scattering models

The intrinsic models for the circumstellar dust scattering region and a point like central star at  $x_0, y_0$  are described by 2-dimensional (2D) maps for each component of the Stokes vector

$$\mathbf{I}'(x, y) = (I'(x, y), Q'(x, y), U'(x, y)), \quad (1)$$

describing the intensity  $I'(x, y)$ , and the linear polarization  $Q'(x, y), U'(x, y)$  in  $x, y$ -coordinates aligned with the object. The circular polarization signal  $V'$  is expected to be much weaker for circumstellar scattering and is neglected. In principle, multiple scattering by dust can produce a circular polarization signal, in particular for (magnetically) aligned dust grains. Measurements for circumstellar circular polarization exist since many decades (e.g., Kwon et al. 2014; Bastien et al. 1989; Angel & Martin 1973), but the signals are weak, or originate from regions far away from the star, where interstellar magnetic fields may play a role. Considering this in our models is beyond the scope of this paper.

The models use  $\mathbf{I}'(x, y) = \mathbf{I}'_s + \mathbf{I}'_d(x, y)$  consisting of a star  $\mathbf{I}'_s(x, y) = \mathbf{I}'_s(0, 0) = \mathbf{I}'_s$ , with or without an intrinsic polarization  $Q'_s, U'_s$  and an extended dust scattering region  $\mathbf{I}'_d(x, y)$  according to the vector components

$$I'(x, y) = I'_s + I'_d(x, y), \quad (2)$$

$$Q'(x, y) = Q'_s + Q'_d(x, y), \quad (3)$$

$$U'(x, y) = U'_s + U'_d(x, y). \quad (4)$$

In most models the star is not polarized and  $Q'_s$  and  $U'_s$  are set to zero or  $Q'(x, y) = Q'_d(x, y)$  and  $U'(x, y) = U'_d(x, y)$ .

**Scattering geometries.** We consider the axisymmetric models Ring0 and Disk0 representing circumstellar disks seen pole-on or spherical dust shells as illustrated by the intensity maps  $I'_d(x, y)$  in the upper row of Fig. 2. The intrinsic polarization flux  $P'_d$  is proportional to the intensity  $P'_d(x, y) = 0.25 \cdot I'_d(x, y)$ .

The Ring0 models have a mean radius  $r_0$  and a Gaussian radial profile with full width at half maximum (FWHM) of  $\Delta r = 0.2 r_0$  and  $r_0$  is varied from 3.15 mas to 806.4 mas. The Disk0 models are axisymmetric scattering regions extending from an inner  $r_{\text{in}}$  to an outer radius  $r_{\text{out}}$ , with a surface brightness (SB) described by the power law

$$I'_d(r) = A_I (r/r_{\text{ref}})^\alpha, \quad (5)$$

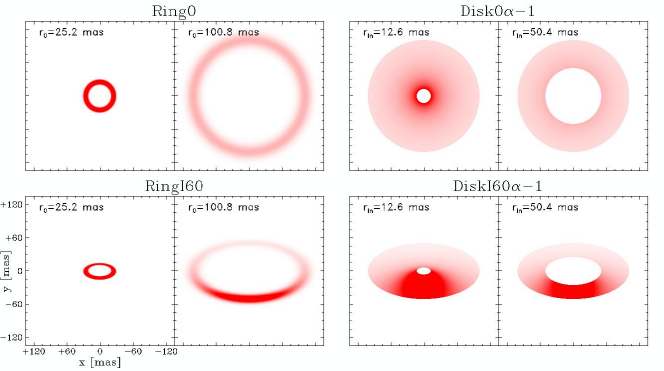


**Fig. 2.** Maps for the intrinsic disk intensity  $I'_d(x, y)$  for the four used types of circumstellar scattering models.

with reference radius  $r_{\text{ref}}$ . Three cases, Disk0 $\alpha$ 0, Disk0 $\alpha$ -1, and Disk0 $\alpha$ -2, are considered with  $\alpha = 0$  for a constant SB and  $\alpha = -1$  and  $-2$  for a brightness decreasing with distance. For all cases the outer radius is  $r_{\text{out}} = 100.8$  mas while the radius of the inner cavity is varied between  $r_{\text{in}} = 3.15$  mas and 50.4 mas to investigate the differences between fully resolved and partially resolved scattering regions. Figure 2 shows  $I'_d(x, y)$  maps for Disk0 $\alpha$ -1 with  $r_{\text{in}} = 12.6$  mas and 50.4 mas.

Simulations for non-axisymmetric scattering geometries are obtained by adopting the Ring0 and Disk0 geometries for inclined, flat disks with  $i = 60^\circ$ . The dust density in the disk plane  $\rho_d(r_d)$  of the inclined models RingI60 and DiskI60 $\alpha$ 0, DiskI60 $\alpha$ -1, DiskI60 $\alpha$ -2 are described by the same radial parameters as for the axisymmetric models. The scattering angle in the inclined disk model varies as function of azimuthal angle  $\phi$  on the disk, and therefore also the scattered intensity and polarization depend on  $\phi$ . This is simulated as in Schmid (2021) for flat, optically thin disks with a dust scattering phase function described by a Henyey-Greenstein function for the intensity with asymmetry parameter  $g = 0.6$  and a Rayleigh scattering like dependence for the fractional polarization with  $p_{\text{max}} = 0.25$ . With these settings the resulting model maps  $\mathbf{I}'(x, y)$  depend only on  $r_0$  for the RingI60 model and on  $\alpha$  and the radius of the central cavity  $r_{\text{in}}$  for the DiskI60 models. Figure 2 shows the maps for RingI60 and DiskI60 $\alpha$ -1 with the same  $r_0$  and  $r_{\text{in}}$  parameters as for the pole-on models. The major and minor axes of the inclined disks are aligned with the  $x$  and  $y$  coordinates and the backside of the disk is in the  $+y$  direction. Because of the strong forward scattering ( $g = 0.6$ ) the intensity signal is enhanced on the front-side, and this is a frequently observed property for inclined disks (e.g., Ginski et al. 2023).

## 2.2. Sky coordinates and interstellar polarization

Observations are obtained in sky coordinates  $(\alpha, \delta)$  and the intrinsic maps in system coordinates  $Q'(\alpha, \delta), U'(\alpha, \delta)$  can be transformed into the sky coordinates  $Q''(\alpha, \delta), U''(\alpha, \delta)$  by a rotation of the geometry and the polarization vector (e.g., Schmid 2021). The signal reaching Earth  $Q''(\alpha, \delta), U''(\alpha, \delta)$  is often affected by interstellar polarization introduced by dichroic absorption of magnetically aligned interstellar grains (e.g. Draine 2003). This introduces a fractional polarization offset, which can be described for the usual, low polarization case ( $Q', U' \ll I'$  and  $q, u \ll 1$ ) by

$$Q''(\alpha, \delta) \approx Q'(\alpha, \delta) + q_{\text{is}} I'(\alpha, \delta), \quad (6)$$

$$U''(\alpha, \delta) \approx U'(\alpha, \delta) + u_{\text{is}} I'(\alpha, \delta), \quad (7)$$

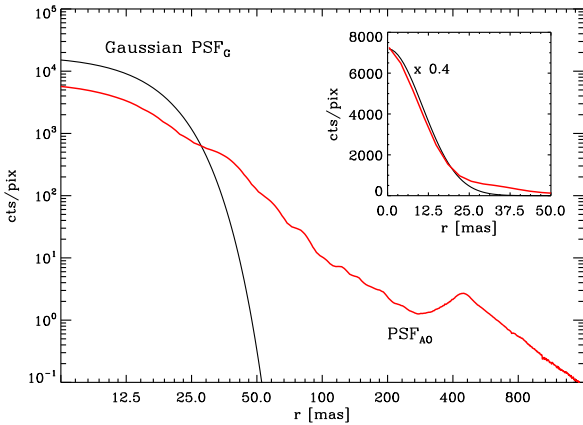


**Fig. 3.** Radial profiles for the extended  $\text{PSF}_{\text{AO}}$  (red) and the Gaussian  $\text{PSF}_G$  (black). In the main panel the total flux is normalized to  $10^6$  counts. In the inset  $\text{PSF}_G$  is reduced by a factor 0.4 for a comparison of the PSF cores. The pixel size is  $3.6 \text{ mas} \times 3.6 \text{ mas}$ .

where  $q_{\text{is}}, u_{\text{is}}$  are the components of the fractional interstellar polarization  $p_{\text{is}} = (q_{\text{is}}^2 + u_{\text{is}}^2)^{-1/2}$  with position angle  $\theta_{\text{is}} = 0.5 \cdot \text{atan}2(u_{\text{is}}, q_{\text{is}})$ <sup>1</sup> defined in sky coordinates. We use flux ratios to quantify the resulting intensity or polarization so that the interstellar transmission losses can be neglected. Extreme dichroic extinction by the interstellar medium can convert linear polarization partly to circular polarization (e.g., Kwon et al. 2014), but this is not considered in this work.

### 2.3. Signal degradation by ground-based AO observations.

The turbulence in the Earth atmosphere leads to a strong seeing convolution of the incoming signal ( $I'', Q'', U''$ ). With an AO system the seeing can be strongly reduced but there remain smearing and polarimetric cancellation effects which can change strongly the spatial distribution of the observed signal  $I(\alpha, \delta), Q(\alpha, \delta), U(\alpha, \delta)$  when compared to the incoming signal (e.g., Perrin et al. 2003; Fétick et al. 2019). The effects are particularly strong for not well resolved structures near the star. The AO correction depends on the atmospheric turbulence and instrument properties and therefore the observational point spread function (PSF) changes with time and shows various types of non-axisymmetric structures (e.g., Cantaloube et al. 2019). In addition, AO instruments are complex and they usually introduce instrumental polarization offsets which are difficult to calibrate accurately (Tinbergen 2007). These observational effects are investigated in this work.

**PSF convolution.** Axisymmetric PSFs are adopted so that the convolved scattering signal does not depend on the orientation of the observed system. Therefore we can apply the convolution directly to the models described in disk coordinates  $(x, y)$ . Real PSFs are variable and deviate from axisymmetry but assuming a stable, axisymmetric PSF is a reasonable approximation for PSFs with high Strehl ratio or for the averaged PSF obtained after a number of polarimetric cycles taken in field rotation mode.

We use  $\text{PSF}_{\text{AO}}(x, y)$  representing an AO system with a narrow core with FWHM or diameter of  $D_{\text{PSF}} = 25.2 \text{ mas}$  and an extended halo. This profile is obtained by averaging azimuthally the PSF described in Schmid et al. (2018) for the standard star

<sup>1</sup> Defined as in the FORTRAN function atan2(y,x) for Cartesian to polar coordinate conversions.

HD 161096 taken under excellent condition with the AO instrument VLT/SPHERE/ZIMPOL in the N\_I filter ( $\lambda_c = 817 \text{ nm}$ ) with a Strehl ratio of about 0.4. The radial profile of  $\text{PSF}_{\text{AO}}$  is plotted in Fig. 3 together with a Gaussian profile  $\text{PSF}_G$  with the same diameter  $D_{\text{PSF}}$ , which is used to investigate the impact of the extended halo in  $\text{PSF}_{\text{AO}}$  on the convolved signal. Convolution with a Gaussian PSF with  $D_{\text{PSF}} \approx \lambda/D$  could also represent roughly diffraction limited imaging polarimetry with a space telescope with diameter  $D$  or ground based seeing limited imaging polarimetry with  $D_{\text{PSF}}$  of the order  $\approx 1000 \text{ mas}$ .

**Polarimetric calibration.** Many types of instrumental effects are introduced in observations taken with high-contrast imaging polarimetry and there exist established procedures to calibrate the data, for example for SPHERE/IRDIS (de Boer et al. 2020; van Holstein et al. 2020) and SPHERE/ZIMPOL polarimetry (Schmid et al. 2018; Hunziker et al. 2020; Tschudi et al. 2024). Individual instruments show also particular effects but these aspects are beyond the scope of this paper.

A very general and important observational effect are the offsets introduced by the interstellar  $p_{\text{is}}$  or by the instrument polarization  $p_{\text{inst}}$  of the kind described in Eqs. 6 and 7. Because the intensity of the star  $\Sigma I_s$  is much higher than the polarization from the circumstellar dust  $\Sigma Q_d, \Sigma U_d$ , by about a factor 100 or even more, already a small fractional polarization offset for the central star of about  $p \approx 0.001$  can strongly disturb the circumstellar signal, while  $p \approx 0.01$  can completely mask that signal. In addition, there could also be a contribution from an intrinsic polarization of the central star. The effects of polarimetric offsets do not depend on the orientation of the selected coordinate system and therefore they can also be treated in the  $(x, y)$ -coordinate system.

Unfortunately, it can be quite difficult to disentangle the different contributions to the overall polarimetric offset and therefore an “ad-hoc” zp-correction for the polarization is often applied to the data, based on the assumption that the polarization of the target in a selected integration region is zero or at least very small (Quanz et al. 2011; Avenhaus et al. 2014). A polarimetric offset sets the integrated Stokes parameters in a certain region to zero  $\Sigma Q^z = \int Q^z(\alpha, \delta) d\alpha d\delta = 0$  and similar for  $\Sigma U^z = 0$ , but this procedure can introduce a bias. For coronagraphic observations the central star cannot be included for the determination of the zp-correction, and this is adding another complication which will also be described.

### 2.4. Analysis of diagnostic polarization parameters

The impact of the convolution and the polarimetric zp-correction, follows from the comparisons between the simulated observational maps  $I(x, y), Q(x, y), U(x, y)$  or the corresponding zp-corrected polarization  $Q^z(x, y), U^z(x, y)$  with the initial maps  $I'(x, y), Q'(x, y), U'(x, y)$ .

Circumstellar scattering produces predominantly a linear polarization in azimuthal direction  $Q_\phi$  with respect to the central star located at  $x_0, y_0$ . Therefore  $Q_\phi$  is a very useful polarization parameter which is defined by

$$Q_\phi(x, y) = -Q(x, y) \cos(2\phi_{xy}) - U(x, y) \sin(2\phi_{xy}), \quad (8)$$

$$U_\phi(x, y) = +Q(x, y) \sin(2\phi_{xy}) - U(x, y) \cos(2\phi_{xy}), \quad (9)$$

with  $\phi_{xy} = \text{atan}2((x - x_0), (y - y_0))$  according to the description of Schmid et al. (2006) for the radial Stokes parameters  $Q_r, U_r$  and using  $Q_\phi = -Q_r$  and  $U_\phi = -U_r$ . The  $U_\phi(x, y)$  parameter gives the linear polarization component rotated by  $45^\circ$  with respect to

azimuthal component  $Q_\phi(x, y)$ . The different polarized intensities for a given point  $(x, y)$  in the polarization maps are related to the polarized flux for the linear polarization according to

$$P(x, y) = (Q^2(x, y) + U^2(x, y))^{1/2} = (Q_\phi^2(x, y) + U_\phi^2(x, y))^{1/2}. \quad (10)$$

Figure 4 illustrates the relation between  $Q_\phi$  and the Stokes parameters  $Q$  and  $U$  for a pole-on disk ring. In this model the  $U_\phi$  component is zero and  $P(x, y) = Q_\phi(x, y)$  because of the axisymmetric geometry. Non-axisymmetric geometries can produce an intrinsic  $U'_\phi(x, y)$  signal, for example by multiple scattering (Canovas et al. 2015), but for the simple (single scattering) models adopted in this work the intrinsic  $U'_\phi(x, y)$ -signal is also zero for inclined disks. However, the convolution and polarimetric offsets will introduce also for these models a  $U_\phi$  signal, which is equivalent to a non-azimuthal polarization component (Fig. 9).

The observational  $Q(x, y)$ ,  $U(x, y)$  or  $Q_\phi(x, y)$ ,  $U_\phi(x, y)$  maps have in high contrast imaging polarimetry often a lower signal per pixel than the photon noise  $\sigma(x, y)$  or other pixel to pixel noise sources. Therefore, the polarized flux  $P(x, y)$  is biased, because it is always positive, and the measured values follow a Rice probability distribution. For a low polarization  $P(x, y) \lesssim \sigma(x, y)$  the noise will introduce on average a signal of about  $P(x, y) \approx +\sigma(x, y)$  (Simmons & Stewart 1985), and this can add up to a very significant spurious signal for the polarized flux  $\Sigma P$  in an integration region  $\Sigma$  containing many tens or more pixels. This noise problem is avoided by using  $Q_\phi(x, y)$  for measuring the strength of the spatially resolved linear polarization (Schmid et al. 2006). This is a reasonable approximation, because circumstellar scattering produces predominantly a polarization in azimuthal direction with  $Q_\phi(x, y) \gg 0$  and  $U_\phi(x, y) \approx 0$  and therefore one can consider  $Q_\phi$  as rough proxy for  $P$  according to

$$P(x, y) = (Q_\phi^2(x, y) + U_\phi^2(x, y))^{1/2} \approx Q_\phi(x, y). \quad (11)$$

Enhanced random noise in the data does not change the mean  $Q_\phi$  signal for a pixel region, but  $P$  is for observational data often very significantly affected by the bias problem described above. The simulations in this work do not consider statistical noise in the data. However, there are other systematic differences between  $Q_\phi(x, y)$  and  $P(x, y)$ , because of the  $U_\phi(x, y)$  signal introduced by the PSF convolution and polarization offsets as will be described by the simulation results.

The convolution and zp-correction effects are quantified using polarization parameters integrated in well defined apertures

$$\Sigma X = \int X(x, y) dx dy, \quad (12)$$

where  $X$  is a place holder for the PSF convolved radiation parameters, like  $X = \{I, Q, U, P, Q_\phi, U_\phi\}$ , and similarly for  $X'$  or  $X''$  for the intrinsic models or zp-corrected models, respectively.  $\Sigma$  defines a circular aperture centered on the star for the determination of the system integrated parameters. Later, we consider also other axisymmetric circular and annular apertures for the parameters of radial subregions (see Sect. 4.3.1). Axisymmetric apertures are very useful for quantifying the convolution by an axisymmetric PSF and polarization offsets for an intensity signal dominated by the axisymmetric stellar PSF.

For a given integration region  $\Sigma$  an “aperture” polarization  $\mathcal{P}(\Sigma) = ((\Sigma Q)^2 + (\Sigma U)^2)^{1/2}$  with the corresponding position angle  $\theta(\Sigma)$  can be defined like for aperture polarimetry. These parameters are useful to specify the polarization of the star, or the fractional polarization  $p = \mathcal{P}(\Sigma)/\Sigma I$  and the fractional Stokes

parameters  $q, u$  to quantify polarization offsets and zp-correction factors (see Sect. A).

The polarization parameters are usually normalized to the integrated intrinsic polarization  $\Sigma Q'_\phi$ , like  $\Sigma Q/\Sigma Q'_\phi$ ,  $\Sigma Q^2/\Sigma Q'_\phi$ , because  $\Sigma Q'_\phi$  provides a good reference for the characterization of the impact of the convolution or of offsets on polarization parameters.

For the characterization of the azimuthal distribution of the polarization  $Q(\phi)$  and  $U(\phi)$  the four Stokes  $Q$  quadrants  $Q_{xxx} = \{Q_{000}, Q_{090}, Q_{180}, Q_{270}\}$ , and the four Stokes  $U$  quadrants  $U_{xxx} = \{U_{045}, U_{135}, U_{225}, U_{315}\}$  are used (Schmid 2021), while  $X_{xxx}$  stands for all eight parameters. They represent the Stokes  $Q$  and  $U$  polarization in the four wedges of  $90^\circ$ , which form for well resolved circumstellar scattering regions the positive-negative  $Q$  and  $U$  quadrant patterns. The signals in these quadrants are changed by the convolution and polarization offsets, and they are useful to quantify the corresponding changes for the azimuthal distribution of the polarization signal  $Q_\phi(\phi)$ .

An overview on the used polarization parameters is given in Sect. A (Tables A.1 and A.2).

### 3. Polarization degradation by the PSF convolution

This section describes the basic PSF smearing and cancellation effects for imaging polarimetry of circumstellar scattering regions. The convolution is always applied to the intrinsic intensity  $I'$  and Stokes  $Q'$ ,  $U'$  maps, or from maps with a polarization offset like the  $Q''$ ,  $U''$  maps, and from the resulting  $Q$  and  $U$  one can then derive according to Eq. 8, 9, and 10 the convolved maps for the polarization parameters  $Q_\phi$ ,  $U_\phi$  and  $P$  (e.g., Tschudi & Schmid 2021). Alternatively, one could also apply the convolution to the  $I'_0$ ,  $I'_{90}$ ,  $I'_{45}$ , and  $I'_{135}$  polarization components and derive from this the convolved intensity and polarization maps, because the convolution operation is distributive ( $\text{PSF} * A + \text{PSF} * B = \text{PSF} * (A + B)$ ). However, a direct convolution of the intrinsic azimuthal polarization ( $\text{PSF} * Q'_\phi$ ) or of the polarized flux ( $\text{PSF} * P'$ ) gives wrong results.

#### 3.1. Convolution for axisymmetric scattering models

##### 3.1.1. Narrow pole-on rings

The convolution depends strongly on the spatial resolution, specifically on the angular size of the scattering signal compared to the PSF widths. This can be described by an axisymmetric scattering geometry like for a dust disk seen pole-on or a spherical dust shell.

Simulations for the convolution of the Ring0 models are shown in Fig. 4 for three ring sizes with  $r_0 = 12.6$  mas, 25.2 mas, and 50.4 mas and using the Gaussian PSF<sub>G</sub>. Maps for the intrinsic dust scattering intensities  $I'_d(x, y)$ , and convolved intensities  $I_d(x, y)$  and the polarization  $Q_d(x, y)$ ,  $U_d(x, y)$ ,  $Q_{\phi,d}(x, y)$  are given. The central star is unpolarized in this model and there is  $Q_d = Q$ ,  $U_d = U$  and  $Q_{\phi,d} = Q_\phi$ . All three models have the same intrinsic flux  $\Sigma I'_d$  and  $\Sigma Q'_\phi$  and therefore the peak fluxes scale like  $\max(I'_d(x, y)) \propto 1/r_0^2$  and is higher for smaller  $r_0$ . The star is unpolarized and therefore does not contribute to the polarization maps. The star  $I_s$  is not included in the intensity maps because for realistic cases it would dominate strongly the scattering intensity  $I_d$ . For the intrinsic model there is  $Q'_\phi(x, y) = P'(x, y)$  and  $U'_\phi(x, y) = 0$ . For axisymmetric models this property is not changed by the convolution and therefore the maps for  $P(x, y)$  and  $U_\phi(x, y)$  are not shown in Fig. 4.

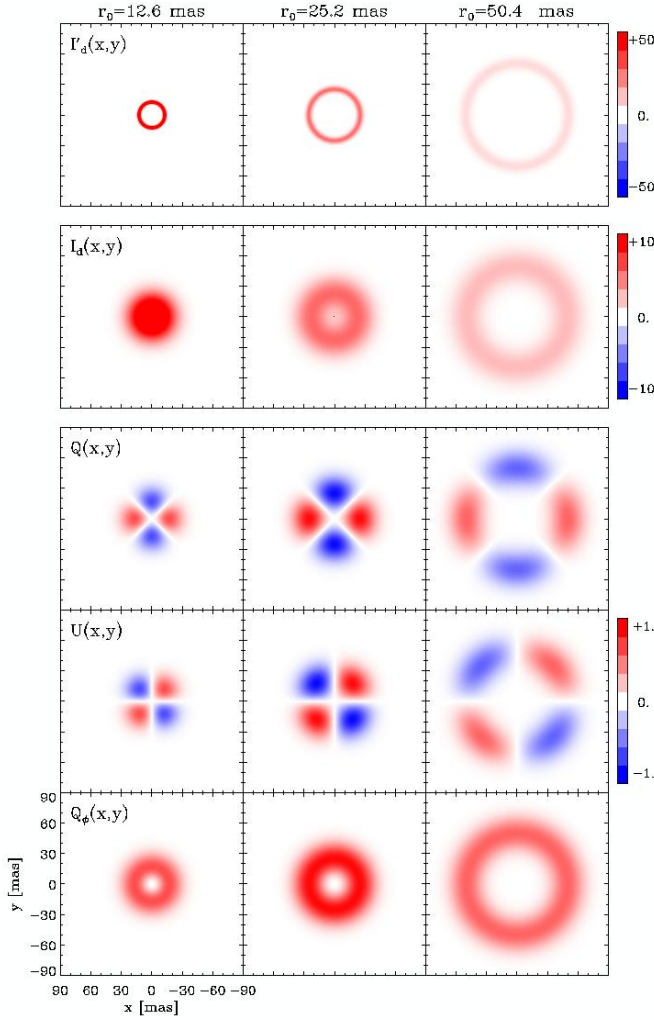


**Fig. 4.** Maps for the Ring0 models with  $r_0 = 12.6$  mas (left),  $25.2$  mas (middle), and  $50.4$  mas (right) for the intrinsic circumstellar intensities  $I'_d(x, y)$ , and the  $PSF_G$  convolved intensity  $I_d(x, y)$  and polarization  $Q_d(x, y)$ ,  $U_d(x, y)$  and  $Q_\phi(x, y)$ .  $\Sigma I'_d$  is the same for all models, and  $\pm 1$  for the color scale represent the same fluxes per pixel for all panels.

Radial profiles for the intensity and azimuthal polarization  $I_d(r)$  and  $Q_\phi(r)$  are plotted in Fig. 5 for the Ring0 model convolved with the Gaussian  $PSF_G$  and the extended  $PSF_{AO}$ . The profiles are normalized to the intrinsic peak flux  $I'_{d,\max} = \max(I'_d(r))$  and  $Q'_{\phi,\max} = \max(Q'_\phi(r))$  respectively, to illustrate the signal degradation. The intensity is smeared by the convolution and this reduces the peak SB of the rings but the total intensity is preserved  $\Sigma I_d = \Sigma I'_d$ . For the smallest model with  $r_0 = 12.5$  mas the ring structure is no more visible (Fig. 4) and there is a strong maximum at the center.

The convolved polarization signal shows also a smearing and in addition a mutual polarimetric cancellation between the positive and negative quadrants in the  $Q$  and  $U$  maps (Schmid et al. 2006). This reduces strongly the polarization signal for  $Q_d(x, y)$ ,  $U_d(x, y)$ , and  $Q_\phi(x, y)$  close to the star and produces also for compact rings a central zero (Figs. 4, 5).

The integrated polarization  $\Sigma Q_\phi$  is reduced for the  $PSF_G$  convolved models by factors  $\Sigma Q_\phi / \Sigma Q'_\phi = 0.91$ ,  $0.66$ , and  $0.28$  for ring radii of  $r_0 = 50.4$  mas,  $25.2$  mas and  $12.6$  mas, respectively (Table 1). We measure the apparent ring size using the radius for the maximum SB  $r(\max(Q_\phi))$  and the size of

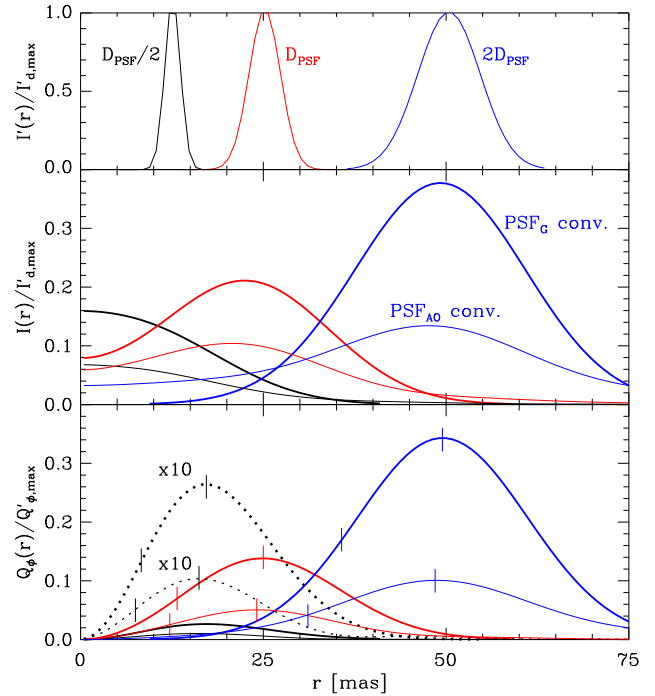


**Fig. 5.** Normalized radial profiles for the intrinsic  $I'_d(r)/I'_{d,\max}$  (top panel), and the  $PSF_G$  (thick lines) and  $PSF_{AO}$  convolved (thin lines) intensity  $I_d(r)/I'_{d,\max}$  (middle panel) for the Ring0 models with  $r_0 = 12.6$  mas (black),  $25.2$  mas (red), and  $50.4$  mas (blue). The bottom panel shows the convolved polarization  $Q_\phi(r)/Q'_{\phi,\max}$ , where the black dotted lines are the black solid lines multiplied by a factor of 10. The radii for the profile peaks  $r(\max(Q_\phi(r)))$  and the central holes  $r_h(Q_\phi)$  given in Table 1 are indicated with vertical marks.

**Table 1.** Results for Ring0 models with different radii  $r_0$ .

$r_0$ [mas]	$\Sigma Q_\phi / \Sigma Q'_\phi$		$r(\max(Q_\phi))$		$r_h(Q_\phi)$		
	$PSF_G$ [ $D_{PSF}$ ]	$PSF_{AO}$ [%]	$PSF_G$ [ $D_{PSF}$ ]	$PSF_{AO}$ [ $D_{PSF}$ ]	$PSF_G$ [ $D_{PSF}$ ]	$PSF_{AO}$ [ $D_{PSF}$ ]	
3.15	.125	2.5	1.0	0.62	0.59	0.31	0.26
6.30	.25	8.3	3.4	0.64	0.59	0.32	0.27
12.6	.5	28.2	11.6	0.68	0.67	0.33	0.30
25.2	1	66.2	28.4	0.99	0.96	0.52	0.48
50.4	2	90.9	46.9	1.96	1.92	1.42	1.23
100.8	4	97.7	60.1	3.98	3.95	3.34	3.19
201.6	8	99.9	66.1 <sup>a</sup>	$\approx r_0$	$\approx r_0$		
403.2	16	99.9	70.1 <sup>a</sup>				
806.4	32	100.	77.9 <sup>a</sup>				
error		$\pm 0.2$	$\pm 0.2$	$\pm 0.02$	$\pm 0.02$	$\pm 0.01$	$\pm 0.01$

**Notes.** Values are given for the integrated azimuthal polarization  $\Sigma Q_\phi / \Sigma Q'_\phi$  for Ring0 models after convolution with the Gaussian  $PSF_G$  and the extended  $PSF_{AO}$ . For compact models also the radii for the peak flux  $r(\max(Q_\phi))$  and for the central hole  $r_h(Q_\phi)$  are listed. The column  $D_{PSF}$  gives the ring radius in units of the FWHM of the PSF. <sup>(a)</sup> Significant amounts of polarization signal not contained in the used aperture with  $r = 1.5''$ .

the central cancellation hole by the radius  $r_h$  at half maximum  $Q_\phi(r_h) = 0.5 \cdot (\max(Q_\phi))$ . For  $r_0 \lesssim 0.5 D_{PSF}$  the peak radius for the convolved ring is significantly larger than  $r_0$ . For larger rings  $r_0 \gtrsim D_{PSF}$  these two radii agree well ( $r(\max(Q_\phi)) \approx r_0$ ).

The  $\Sigma Q_\phi / \Sigma Q'_\phi$  values in Table 1 are significantly lower for the  $PSF_{AO}$  convolved models because of the much stronger

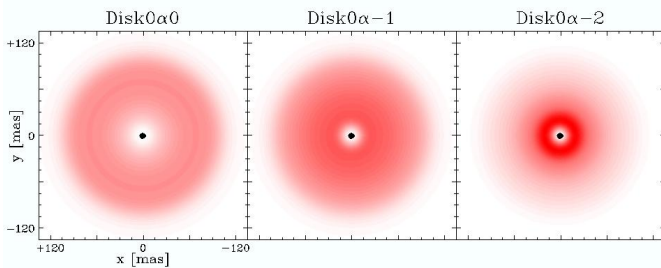


**Fig. 6.** Central cancellation holes in the  $Q_\phi(x, y)$  maps for the models Disk0 $\alpha$ 0, Disk0 $\alpha$ -1, and Disk0 $\alpha$ -2 after convolution with the extended PSF<sub>AO</sub>. The size of the inner cavity  $r_{\text{in}} = 0.125 D_{\text{PSF}}$  (3.15 mas) is the same for all three models and indicated by the black dot.

smearing effects introduced by the PSF halo. For  $r_0 < 4 D_{\text{PSF}}$  the reduction is about a factor of 0.5 lower with respect to a convolution with PSF<sub>G</sub>, or very roughly at the level of the Strehl ratio for PSF<sub>AO</sub> simulated for the AO system.

For very small rings with  $r_0 = 0.25 D_{\text{PSF}}$  and  $0.125 D_{\text{PSF}}$  only a very small amount of the  $Q_\phi$  polarization remains and the radial  $Q_\phi$  profile has for these two cases roughly the same shape as the convolved Ring0 with  $r_0 = 0.5 D_{\text{PSF}}$  with a peak at  $r(\max(Q_\phi)) \approx (2/3) D_{\text{PSF}}$  and a hole radius  $r_h \approx (1/3) D_{\text{PSF}}$ . This represents the simulated inner working angle for the detection of a resolved polarization signal for a circumstellar scattering region. For observational data these limits might be less good because of PSF variation and alignment errors.

Importantly, the spatial resolution is practically not reduced by the convolution with PSF<sub>AO</sub> when compared to PSF<sub>G</sub> and the radii  $r(\max(Q_\phi))$  and  $r_h(Q_\phi)$  for PSF<sub>AO</sub> are very similar for the two cases because both PSF have the same peak width  $D_{\text{PSF}}$ . Therefore, the shape of the radial profiles in Fig. 5 are very similar for the two cases and the morphology of the strong polarization structures in the PSF<sub>G</sub> model maps of Fig. 4, would look practically the same for a convolution with PSF<sub>AO</sub>. The halo of the PSF<sub>AO</sub> introduces faint, extended polarization artefacts for axisymmetric geometries as described in the Appendix (Sect. B), but they are very weak with a surface brightness of  $\lesssim 1\%$  when compared to the peak signal of the ring.

### 3.1.2. Radially extended scattering regions

Axisymmetric, radially extended disks or shells models are just superpositions of concentric ring signals, and the polarimetric cancellation effects will be strong for the innermost regions and much reduced further out. Therefore, the convolved polarization signal strongly underestimates the scattering near the central star and can mimic the presence of a central cavity even if no such cavity is present. The effect is illustrated in Fig. 6 with PSF<sub>AO</sub> convolved  $Q_\phi(x, y)$  maps for the models Disk0 $\alpha$ 0, Disk0 $\alpha$ -1, and Disk0 $\alpha$ -2, with radial brightness profiles  $Q'_\phi(r) = A_\phi, A_\phi(r/r_{\text{ref}})^{-1}$ , and  $A_\phi(r/r_{\text{ref}})^{-2}$ , respectively. In all three cases the intrinsic disk extends from  $r_{\text{in}} = 3.15$  mas or  $0.125 D_{\text{PSF}}$  to  $r_{\text{out}} = 100.8$  mas. The radius of the convolution hole ( $r_h(Q_\phi)$ ) is slightly smaller than  $0.4 D_{\text{PSF}}$  for the  $\alpha = -2$  case and slightly larger than  $0.4 D_{\text{PSF}}$  for the  $\alpha = -1$  disk with a flatter brightness distribution (Table C.1).

**Constant surface brightness.** The convolution effects for Disk0 $\alpha$ 0 are shown in Fig. 7 with radial profiles for the intrinsic parameters  $I'_d(r) = I'_0$ ,  $Q'_\phi(r) = A_\phi = 0.25 I'_0$  and the convolved intensity  $I_d(r)$  and polarization  $Q_\phi(r)$  for different inner

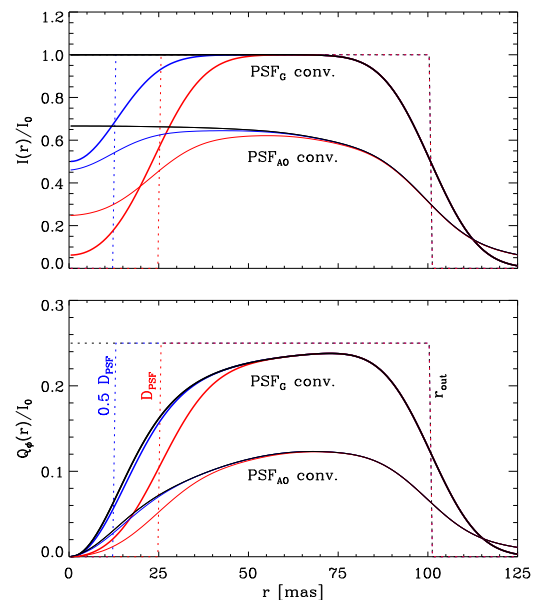


**Fig. 7.** Normalized profiles  $I(r)/I'_0$  and  $Q_\phi(r)/I'_0$  for the Disk0 $\alpha$ 0 models with  $r_0 = D_{\text{PSF}}$  (red),  $0.5 D_{\text{PSF}}$  (blue) and without cavity (black) for PSF<sub>G</sub> (thick) and PSF<sub>AO</sub> (thin) convolution, and for the intrinsic model (dotted).

disk radii  $r_{\text{in}}$  and for PSF<sub>G</sub> and PSF<sub>AO</sub> convolution. The profiles  $I_d(r)$  show for increasing cavity size  $r_{\text{in}}$  an increasing central dip depth and width. The surface brightness (SB)  $I_d(r)$  is strongly reduced after convolution with PSF<sub>AO</sub> while the central cavity is less pronounced. The convolution does not change  $\Sigma I_d$  but for PSF<sub>AO</sub> a lot of the signal is redistributed to radii  $r \gg 100$  mas.

The convolved  $Q_\phi(r)$  profiles show for all cases a central zero  $Q_\phi(0) = 0$ , even for the disk without central cavity. Only models with  $r_{\text{in}} \approx D_{\text{PSF}}$  or larger show an obvious difference when compared to the model without cavity. The  $Q_\phi(r)$  profiles do not reach the intrinsic  $Q'_\phi(r)$  level even for the convolution with a narrow PSF<sub>G</sub>, because of the polarimetric cancellation. For the convolution with PSF<sub>AO</sub> there is an additional reduction of the  $Q_\phi(r)$  level by about 40 % but despite this, the radial shape of the profiles is very similar for the two cases as follows also from hole radii  $r_h(Q_\phi)$  given in Table C.1.

**Centrally bright scattering regions.** Many circumstellar disks and shells show a steep SB profile increasing strongly towards smaller radii. Therefore, the polarimetric cancellation suppresses efficiently the intrinsically very bright but barely resolved central signal (e.g., Avenhaus et al. 2018; Garufi et al. 2020; Khouri et al. 2020; Andrych et al. 2023).

Simulations of radial profiles are shown in Fig. 8 for PSF<sub>AO</sub> convolved models DiskI60 $\alpha$ -2 with intrinsic SB profile for the polarization  $Q'_\phi(r) = A_\phi(r/r_{\text{ref}})^{-2}$  with  $r_{\text{ref}} = 12.6$  mas and  $A_\phi = 20.7$  similar to Eq. 5 and for different cavity sizes  $r_{\text{in}}$ . The convolved profiles  $Q_\phi(r)$  show clearly how the central hole size decreases for smaller  $r_{\text{in}}$ , and how the measurable peak polarization signal  $\max(Q_\phi(r))$  increases. Despite the strongly increasing intrinsic  $Q'_\phi$  signal at small radii the convolved  $Q_\phi(r)$  curves converge to a limiting model case with  $r_i \approx 0.2 D_{\text{PSF}}$  ( $\approx 5$  mas), because even large amounts of intrinsic signal in the center are fully cancelled by the convolution (Table C.1). The  $Q_\phi(r)$  profiles are still quite sensitive for constraining the intrinsic  $Q'_\phi(r)$  signal around  $r \approx D_{\text{PSF}}$  based on the location of the flux max-

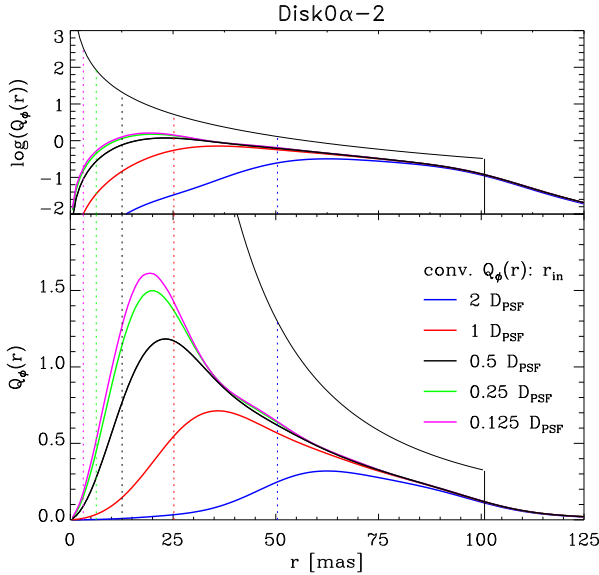


**Fig. 8.** Radial profiles  $Q_\phi(r)$  for the Disk0 $\alpha$ -2 model convolved with PSF<sub>AO</sub> on a log-scale (upper panel) and a linear scale (lower panel) for different inner cavities  $r_0$  as indicated by the colors. The thin black line is the intrinsic SB  $Q_\phi(r) \propto r^{-2}$ .

imum  $r(\max(Q_\phi))$  and the amount of  $Q_\phi(r)$  signal near this location. A careful analysis of  $Q_\phi(r)$  can therefore constrain an inner cavity for a dust scattering region and this could be potentially useful for estimates on the dust sublimation radius for disks around young stars or the dust condensation radius for circumstellar shells around mass losing stars.

Details of the profiles  $Q_\phi(r)$  depend also on the power law index  $\alpha$  for the SB. The peak radii  $r(\max(Q_\phi(r))$  and central hole radii  $r_h$  for a given  $r_{\text{in}}$  are a bit larger for Disk0 $\alpha$ -1 than Disk0 $\alpha$ -2 (Table C.1), because in this model the contributions of smeared signal from larger separations are more important than for Disk0 $\alpha$ -2 and this reduces the apparent sharpness of the central cancellation hole.

### 3.2. Convolution for inclined disk ring models

The scattering geometry for a rotationally symmetric system with an inclined symmetry axis is not axisymmetric and then new features appear in the intensity and polarization maps. This is illustrated in Fig. 9 by the PSF<sub>G</sub> convolved maps for the scattered intensity  $I_d$  and the polarization parameters  $Q$ ,  $U$ ,  $Q_\phi$ ,  $U_\phi$ , and  $P$  for RingI60 models with an inclination of  $i = 60^\circ$  and  $r_0 = 12.5$  mas, 25.2 mas and 50.4 mas and including the intrinsic maps for the last case. The central star is assumed to be unpolarized, or  $Q = Q_d$ ,  $U = U_d$  and  $P = P_d$ , and the stellar intensity is not included in the  $I_d(x, y)$  intensity maps. All RingI60 models have the same intrinsic polarization  $\Sigma Q'$ .

The ring front side is much brighter because of the adopted forward scattering parameter  $g = 0.6$  for the dust and this is clearly visible for the  $I'(x, y)$  and  $I(x, y)$  maps for  $r_0 = 50.4$  mas. This changes for the less resolved systems into a front-side intensity arc for  $r_0 = 25.2$  mas or  $r_0 = D_{\text{PSF}}$  and a slightly elongated spot offset towards the front side for  $r_0 = 12.6$  mas ( $0.5 D_{\text{PSF}}$ ).

The inclined models show a left-right symmetry for the intensity  $I_d(x, y) = I_d(-x, y)$ , for Stokes  $Q$ , the azimuthal polarization  $Q_\phi$ , and the polarized flux  $P$ . The Stokes  $U$ -parameter has

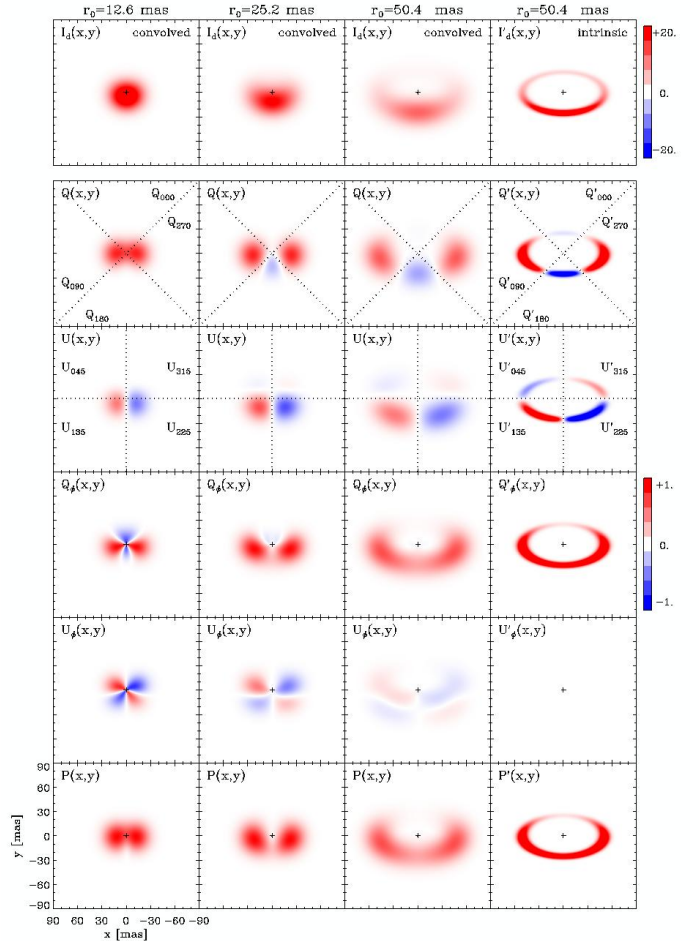


**Fig. 9.** Maps for the intensity  $I_d$  and polarization  $Q_\phi$ ,  $Q$ ,  $U$ ,  $Q_\phi$ ,  $U_\phi$ , and  $P$  (from top to bottom) for RingI60 models with  $r_0 = 12.6$  mas, 25.2 mas and 50.4 mas after convolution with the Gaussian PSF<sub>G</sub> (first three columns). The last column gives the same for the intrinsic model with  $r_0 = 50.4$  mas. Stokes quadrant parameters are indicated in some  $Q$  and  $U$  maps.

a left-right antisymmetry  $U_d(x, y) = -U_d(-x, y)$ , as well as the  $U_\phi$ -signal introduced by convolution effects.

The intrinsic Stokes parameters  $Q'(x, y)$  and  $U'(x, y)$  show positive and negative regions which can be characterized by the quadrant polarization parameters  $Q'_{000}$ ,  $Q'_{090}$ ,  $Q'_{180}$ , and  $Q'_{270}$  for Stokes  $Q'$  and  $U'_{045}$ ,  $U'_{135}$ ,  $U'_{225}$ , and  $U'_{315}$  for Stokes  $U'$  as indicated in Fig. 9. They are useful for the characterization of the azimuthal distribution of the polarization based on the natural Stokes patterns produced by circumstellar scattering (Schmid 2021). Quadrant parameters have been calculated for simple models of debris disks (Schmid 2021) and of transition disks (Ma & Schmid 2022).

The intrinsic RingI60 models have strong positive  $Q_{090}$  and  $Q_{270}$  quadrants centered on the major axis of the projected disk, because of the high fractional polarization produced by scatterings with  $\theta \approx 90^\circ$ . The front side quadrant  $Q_{180}$  shows for well resolved systems a clear negative component, which is however less dominant than in intensity, because the fractional polarization of forward scattering is lower than for  $90^\circ$  scattering.

The negative  $Q_{000}$  and  $Q_{180}$  components disappear for not well resolved disks because the PSF smearing of the two strong positive components  $Q_{090}$  and  $Q_{270}$  cancel the signal of the negative Stokes  $Q$  quadrants. For the convolved RingI60 model with

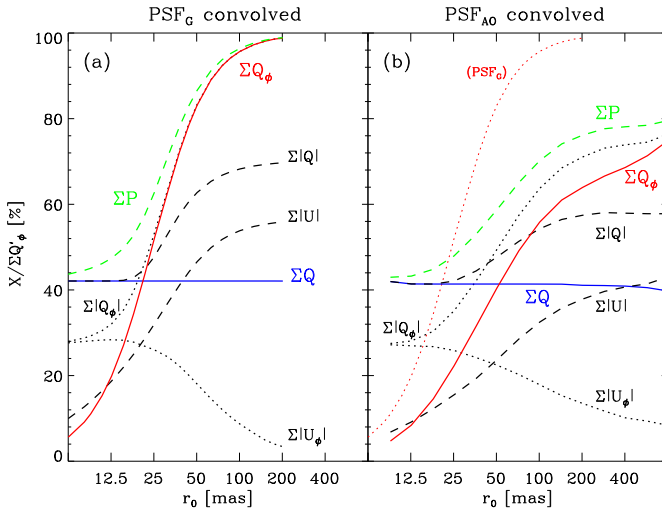


**Fig. 10.** Integrated polarization parameters for the RingI60 model as function of the ring radius  $r_0$  after convolution with PSF<sub>G</sub> (a) and PSF<sub>AO</sub> (b). All parameters are normalized to the intrinsic value  $\Sigma Q'_\phi = 100$  %. In panel (b) the  $\Sigma Q'_\phi$  curve from panel (a) is repeated as dotted line.

$r_0 = 12.6$  mas there remain only two positive  $Q_d$ -spots but their relative position still indicates the orientation of the projected major axis. The brighter disk front side produces in the Stokes  $U_d$  map a left side dominated by the positive  $U_{135}$  signal and a right side by the negative  $U_{225}$  component. This feature is still visible for barely resolved disks and this indicates the location of the disk front-side.

The intrinsic disk polarization of our models is everywhere azimuthal and therefore the map  $Q'_\phi(x, y)$  is equal  $P'(x, y)$ , while  $U'_\phi(x, y) = 0$  according to Eq. 10. The convolved maps  $Q_\phi(x, y)$  for  $r_0 = 50.4$  mas represents well the intrinsic map apart from the smearing, but for less well resolved disks  $Q_\phi(x, y)$  starts to display negative values above and below the center and for  $r_0 = 12.6$  mas a strong, central quadrant pattern for  $Q_\phi(x, y)$  is visible as expected for an unresolved, central source with a positive Stokes  $\Sigma Q$  signal and  $\Sigma U = 0$ .

The convolution of the non-axisymmetric scattering polarization produces a  $U_\phi$  signal and we call this effect the convolution cross-talks for the azimuthal polarization<sup>2</sup>  $Q_\phi \rightarrow U_\phi$ . This effect increases with decreasing spatial resolution and therefore the  $U_\phi(x, y)$  signal becomes stronger for less well resolved disks. For an unresolved disk the quadrant patterns for the azimuthal polarization  $Q_\phi(x, y) = -Q(x, y) \cos(2\phi_{xy})$  and  $U_\phi(x, y) = Q(x, y) \sin(2\phi_{xy})$  are equally strong but rotated by 45°. For the polarized flux  $P$  the convolved signal for large rings is roughly equal to the azimuthal polarization  $P(x, y) \approx Q_\phi(x, y)$ , and for barely resolved rings it evolves towards  $P(x, y) \approx Q(x, y)$ , (Fig. 9).

### 3.2.1. Convolution and integrated polarization parameters

The convolution with a normalized PSF does not change the integrated Stokes polarization or the integrated intensity. Thus, there is for the RingI60 models  $\Sigma Q = \Sigma Q' = 0.421 \Sigma Q'_\phi$  and  $\Sigma U = \Sigma U' = 0$ , independent of the disk size or the spatial resolution. Contrary to this, the integrated polarization parameters

$\Sigma Q_\phi$ ,  $\Sigma U_\phi$ , and  $\Sigma P$  and the sums of absolute values  $\Sigma |Q|$  and  $\Sigma |U|$ ,  $\Sigma |Q_\phi|$  and  $\Sigma |U_\phi|$  depend on the resolution and the PSF convolution. The dependencies are plotted for the RingI60 models as function of ring radius  $r_0$  convolved with PSF<sub>G</sub> and PSF<sub>AO</sub> in Fig. 10, and Table D.1 lists numerical values.

The red curves in Fig. 10 show  $\Sigma Q_\phi$ , which is large for well resolved disks and approaches zero for small, unresolved disks  $r_0 \rightarrow 0$  when the  $Q_\phi$  map shows a perfect positive-negative quadrant pattern with no net  $\Sigma Q_\phi$  polarization. For the intrinsic disk there is  $\Sigma P' = \Sigma Q'_\phi = \Sigma |Q'_\phi|$  and  $\Sigma |U'_\phi| = 0$  and these relations are still approximately valid for well resolved disks convolved with PSF<sub>G</sub> because the convolution effects are small (Fig. 10(a)). The convolution with PSF<sub>AO</sub> introduces even for very extended disks strong smearing, because of the extended PSF halo (Fig. 10(b)). Therefore,  $\Sigma P$  is for well resolved disks larger than  $\Sigma Q_\phi$  by about 5 % for the model with  $r_0 \approx 800$  mas and about 18 % for  $r_0 = 201.6$  mas (Table D.1).

For an unresolved scattering region  $r_0 \ll D_{\text{PSF}}$  there remains only an unresolved polarized source with  $\Sigma P$ . Because of the alignment of the RingI60 models with the  $(x, y)$  disk coordinates, there is  $\Sigma Q = \Sigma |Q| = \Sigma P$  and  $\Sigma U = \Sigma |U| = 0$ . The azimuthal polarization is then zero  $\Sigma Q_\phi \approx 0$  and the integrated absolute values for the azimuthal polarization are  $\Sigma |Q_\phi| = \Sigma |U_\phi| = (2/\pi) |\Sigma P|$  for the quadrant pattern of an unresolved source (Schmid 2021).

In the models a net signal in azimuthal polarization  $\Sigma Q_\phi > 0$  or an integrated absolute signal  $\Sigma |Q_\phi|$  larger than  $\Sigma |U_\phi|$  indicates the presence of at least a marginally resolved circumstellar polarization signal (Fig. 10). In observational data,  $\Sigma Q_\phi$  signals can also be produced by noise effects and one needs to derive for a given data set the limits for a significant detection of a resolved circumstellar  $\Sigma Q_\phi$ -signal. However, one can expect for random noise sources introduced for example by the atmospheric turbulence, photon and read-out noise, that they produce also random positive and negative  $Q_\phi$  and  $U_\phi$  signals, and different systematic effects like polarization offsets (see Sect. 4) or alignment errors produce no or only small positive or negative  $\Sigma Q_\phi$  and  $\Sigma U_\phi$  signals. Therefore, the two criteria  $\Sigma Q_\phi > 0$  and  $\Sigma |Q_\phi| > \Sigma |U_\phi|$  are reliable indicators for the presence of resolved circumstellar polarization. Contrary to this, the  $\Sigma P$  signal is systematically enhanced by random noise and also polarization offsets change typically  $\Sigma P$  substantially.

### 3.2.2. Halo signals produced by an extended PSF<sub>AO</sub>

The extended halo in the PSF<sub>AO</sub> of an adaptive optics system smears substantially the net Stokes polarization  $\Sigma Q$ ,  $\Sigma U$  of a system over a large area producing an extended  $P(x, y)$  halo of linear polarization for  $r \gg r_0$ . This halo effect is illustrated in Fig. 11 for the PSF<sub>AO</sub> convolved RingI60 model with  $r_0 = 50.4$  mas, where the smeared  $\Sigma Q$  signal produces a polarized speckle ring ghost around  $r \approx 0.4''$  and a halo. The Stokes  $U$  signal in the halo is much weaker because there is no net  $U$ -signal for this model, and only a much weaker artefact pattern of the kind described in Sect. B is visible. The  $Q$ -halo produces extended  $Q_\phi(x, y)$ ,  $U_\phi(x, y)$  quadrant patterns including the relatively strong speckle ring around  $r \approx 0.4''$ , which shows the small scale imprint of the polarization from the bright ring.

The surface brightness (SB) of the halo is low and it can be difficult to recognize it in real data because of observational noise. Nonetheless, for the RingI60 model shown in Fig. 11 the  $Q$ -halo integrated in an annulus from  $r = 0.2''$  to  $1.5''$  is almost 30 % of the system integrated  $\Sigma Q$ -signal (Table D.1). Therefore,

<sup>2</sup> This convolution cross-talk is different from instrumental polarization cross-talks which are introduced by optical components (e.g., Tinbergen 2007).

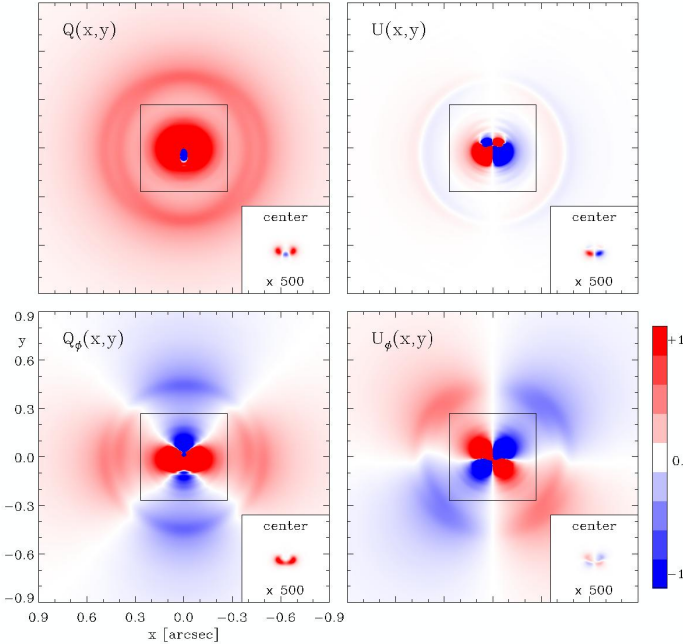


**Fig. 11.** Large scale halo signals for the Stokes parameters  $Q$ ,  $U$ , and the azimuthal polarization  $Q_\phi(x, y)$ ,  $U_\phi(x, y)$  for the RingI60 model with  $r_0 = 50.4$  mas convolved with  $\text{PSF}_{\text{AO}}$ . The inset on the lower right in each panel shows the disk ring in the center with a  $500\times$  reduced color scale.

it is important to use large integration apertures for the determination of  $\Sigma Q$  and  $\Sigma U$  for data convolved by an extended PSF.

The  $Q_\phi$  signal in the halo integrated from  $r = 0.2''$  to  $1.5''$  contributes less than 0.2 % to the total  $\Sigma Q_\phi$  (Tab. D.1), because this signal has a positive-negative  $Q_\phi$ ,  $U_\phi$  quadrant patterns with zero net signal. Therefore, the measurement of  $\Sigma Q_\phi$  for a compact circumstellar scattering region should be restricted to a circular aperture which excludes the outer halo regions containing no net  $Q_\phi$  signal but possibly substantial observational noise.

### 3.2.3. Convolution cross-talk $Q_\phi \rightarrow U_\phi$ or intrinsic $U_\phi$ signal

The models considered in this work use a simplified description of the dust scattering which does not produce an intrinsic  $U'_\phi(x, y)$  polarization. However, it was pointed out in Canovas et al. (2015) that multiple-scattering by dust in optically thick protoplanetary disks with a non-axisymmetric scattering geometry can produce intrinsic  $U'_\phi$  signals representing non-azimuthal polarization components. Their simulations give  $U'_\phi(x, y)$  signals of up to about  $\pm 5$  % of the azimuthal polarization  $Q_\phi(x, y)$  and this  $U'$ -polarization can be useful to constrain the dust scattering properties and the disk geometry. This effect was also recognized in the disk models presented by Ma & Schmid (2022, Fig. 6).

As discussed above, also the PSF convolution can produce very substantial  $U_\phi(x, y)$  signals for models with zero intrinsic  $U'_\phi(x, y)$ . This fact was already mentioned by Canovas et al. (2015) but they did not quantify this effect and their modelling used only a Gaussian PSF for the convolution.

The RingI60 simulations can be used to quantify the  $Q_\phi \rightarrow U_\phi$  convolution signal for different disk sizes  $r_0$ . We use as simple metric for this effect the ratio  $\Sigma|U_\phi|/\Sigma|Q_\phi|$  given in Table D.1 (see also the  $\Sigma|U_\phi|$  and  $\Sigma|Q_\phi|$  curves in Fig. 10). For an unresolved disk the convolution gives as extreme limit a ratio  $\Sigma|U_\phi|/\Sigma|Q_\phi| = 1$ . The ratio is 0.22 and still high for the  $\text{PSF}_G$

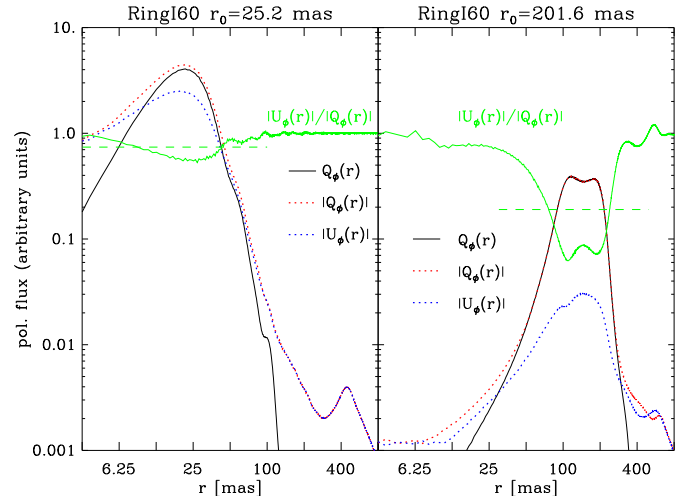


**Fig. 12.** Azimuthally averaged profiles for  $Q_\phi(r)$ ,  $|Q_\phi(r)|$  and  $|U_\phi(r)|$  for the RingI60 models with  $r_0 = 25.2$  mas and  $201.6$  mas convolved with  $\text{PSF}_{\text{AO}}$ . The green curve for the ratio  $|U_\phi(r)|/|Q_\phi(r)|$  provides a rough measure for the convolution cross talk and the dashed line indicates the system integrated value  $\Sigma|U_\phi|/\Sigma|Q_\phi|$  from Table D.1

convolved disk with  $r_0 = 50.4$  mas plotted in Fig. 9. A larger disk of about  $r_0 = 201.6$  mas is required to reach a low ratio of 0.03 so that an intrinsic  $U_\phi$ -signal could be detectable.

The situation is worse for disk models convolved with  $\text{PSF}_{\text{AO}}$  producing substantially more  $Q_\phi \rightarrow U_\phi$  cross-talk and the ratio  $\Sigma|U_\phi|/\Sigma|Q_\phi|$  is 0.19 for  $r_0 = 201.6$  mas and still larger than 0.1 for  $r_0 = 806.4$  mas. The strong smearing of the Stokes  $Q$ -signal produces in the halo a ratio  $\Sigma|U_\phi|/\Sigma|Q_\phi| \approx 1$ . For a more detailed analysis the radial dependence of the ratio  $|U_\phi(r)|/|Q_\phi(r)|$  should be considered, and such profiles are shown in Fig. 12 for  $\text{PSF}_{\text{AO}}$  convolved RingI60 models with  $r_0 = 25.2$  mas and  $201.6$  mas. For the compact disk the  $|Q_\phi(r)|$  signal is only at the separation of the ring  $r \approx 12 - 35$  mas substantially larger than  $|U_\phi(r)|$ , but nowhere more than a factor of 2. For the unresolved polarization near the center and for the smeared halo signal the ratio is  $|U_\phi(r)|/|Q_\phi(r)| \approx 1$ . For the larger disk, the  $Q_\phi(r)$  signal dominates the  $U_\phi(r)$  cross-talk signal by about a factor of 20 at the location of the inclined ring  $r \approx 100 - 200$  mas.

This indicates that an intrinsic  $U'_\phi$  polarization at the level of 0.05  $Q'_\phi$  is only detectable for large disks  $r_0 \gtrsim 200$  mas in high quality data for currently available AO systems, otherwise the convolution cross talks dominate. Helpful is, that the expected geometric structure of the observable  $U_\phi(x, y)$  signal produced by multiple scattering (see Canovas et al. 2015; Ma & Schmid 2022) is different from the  $Q_\phi \rightarrow U_\phi$  convolution artefacts, which can even be constrained strongly from the observed  $Q_\phi(x, y)$  signal. In any case, the detection of the presence of intrinsic  $U'_\phi(x, y)$  polarization requires high quality data of an extended scattering region and a very careful assessment of the convolution cross talk effects.

$U_\phi$  signal and  $Q_\phi$  uncertainty. In many studies the  $U_\phi$  signal is used as a proxy for the observational uncertainty for the measured  $Q_\phi$  signal. This is a reasonable approach for cases with small  $Q_\phi \rightarrow U_\phi$  cross talk, like axisymmetric or close to axisymmetric scattering geometries, and very extended systems like RingI60 models with  $r \gtrsim 200$  mas. The spurious signals introduced by speckle noise, read-out and photon noise, and small

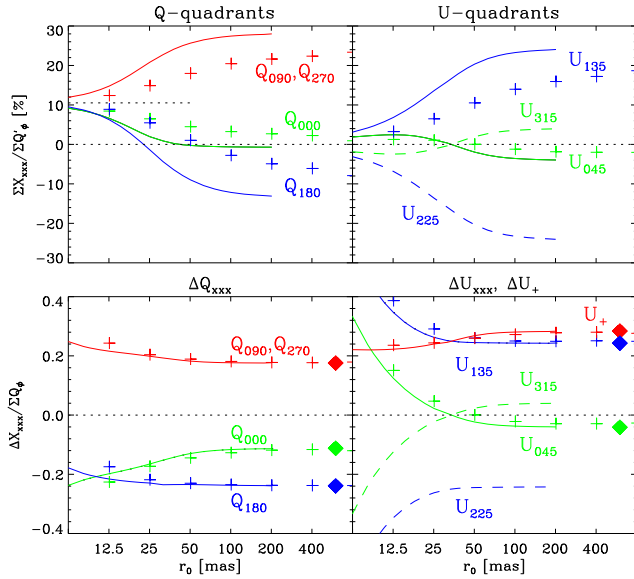


**Fig. 13.** Quadrant polarization parameters  $\Sigma X_{XXX}$  normalized to the intrinsic azimuthal polarization  $\Sigma Q_\phi$  (upper panels) and differential quadrant parameters  $\Delta X_{XXX}$  normalized to the convolved  $\Sigma Q_\phi$  (lower panels) for RingI60 models as function of radius  $r_0$ . Full lines give the values for  $\text{PSF}_G$  convolved, and crosses for  $\text{PSF}_{AO}$  convolved models while the filled diamonds are the intrinsic values. For clarity not all  $\Delta U_{XXX}$  values are given.

scale instrumental artefacts in the  $U_\phi$  map are then larger than the convolution cross-talk and therefore also representative for observational uncertainties in the  $Q_\phi$  map.

However, for non-axisymmetric compact scattering regions the  $U_\phi$  signal consist mainly of the well defined systematic convolution cross-talk signal with high ratios  $|U_\phi(r)|/|Q_\phi(r)| \gtrsim 0.5$  like the RingI60  $r_0 = 25.2$  mas model in Fig. 12. Despite this the azimuthal polarization signal  $Q_\phi$  can still be highly significant, because for high quality data the observational noise in  $Q_\phi$  is much smaller than the systematic  $Q_\phi \rightarrow U_\phi$  cross talk. In such cases another metric than the  $U_\phi$  signal must be used for the assessment of the observational uncertainties, like the dispersion of the measured results for different data sets or a detailed analysis of speckle and pixel to pixel noise in the data.

Nonetheless, a low  $|U_\phi|$  signal can be used to identify high quality data within a series of measurements taken under variable observing conditions. Because the systematic cross talk  $Q_\phi \rightarrow U_\phi$  is anti-correlated with the quality of the observational PSF one can select the polarization cycles with low  $|U_\phi|$  and this may provide a higher quality  $Q_\phi$  map for a target.

### 3.2.4. Convolution and quadrant polarization parameters

The convolution can change for not well resolved RingI60 models strongly the azimuthal distribution of the polarization signal  $Q_\phi(\phi)$  and  $U_\phi(\phi)$ . This can be quantified with the quadrant polarization parameters which provide a simple formalism for the description of polarimetric convolution effects. We use the symbol  $X_{XXX}$  for all quadrant parameters, and  $Q_{XXX}$  or  $U_{XXX}$  for the four Stokes  $Q$  or Stokes  $U$  quadrants, respectively. The quadrant values are related to the integrated Stokes parameters according to

$$\Sigma Q = \Sigma Q_{000} + \Sigma Q_{090} + \Sigma Q_{180} + \Sigma Q_{270}, \quad \text{and} \quad (13)$$

$$\Sigma U = \Sigma U_{045} + \Sigma U_{135} + \Sigma U_{225} + \Sigma U_{315}. \quad (14)$$

For the mirror-symmetric RingI60 models, there is also  $\Sigma Q_{000} = \Sigma Q_{270}$ ,  $\Sigma U_{045} = -\Sigma U_{315}$  and  $\Sigma U_{135} = -\Sigma U_{225}$  (Schmid 2021).

The convolution changes the flux in the different Stokes quadrants because of smearing and mutual cancellation as can be seen in Fig. 9. This degradation is also illustrated for the normalized quadrant parameters  $\Sigma X_{XXX}/\Sigma Q'_\phi$  for the  $\text{PSF}_G$  and  $\text{PSF}_{AO}$  convolved RingI60 models as function of  $r_0$  in the upper panels of Fig. 13 (see also Table D.1). For smaller and less resolved disks all  $Q$ -quadrants approach the same value  $\Sigma Q_{XXX} = \Sigma Q_d/4$  as expected for an unresolved system with an integrated polarization  $\Sigma Q_d$ . For the Stokes  $U$  quadrants the effects are equivalent on both sides of the  $y$ -axis, and strong smearing turns the sign of the weaker back-side quadrants values  $U_{045}$  and  $U_{135}$  to the sign of the strong front side quadrants. This produces for compact disks positive signals for  $U_{045}$  and  $U_{135}$  “on the left side” of the star, and negative signals for  $U_{225}$  and  $U_{315}$  “on the right” side in (Fig. 9) for the RingI60 model with  $r_0 = 12.6$  mas.

**Differential quadrant parameters.** Despite the smearing and polarimetric cancellation the information about the relative intrinsic strengths of the quadrant parameters can still be recovered to some degree as long as the scattering region is partially resolved. This is possible, because the mutual compensation of the polarization signal changes opposite sign quadrants roughly by similar amounts (Fig. 13 upper panel), and in step with the degradation of the total azimuthal polarization  $\Sigma Q_\phi$  shown in Fig. 10 for the same models.

Therefore, good values to constrain the intrinsic  $\Sigma Q'_{XXX}$  fluxes are the relative differential values

$$\frac{\Delta Q_{XXX}}{\Sigma Q_\phi} = \frac{\Sigma Q_{XXX} - (\Sigma Q/4)}{\Sigma Q_\phi}, \quad (15)$$

which quantify how much the individual Stokes  $Q$  quadrants contribute to the total Stokes  $Q$  signal (Eq. 13), or how much more or less than the average contribution  $Q/4$ . According to Fig. 13 (lower left and Table D.2) the  $\Delta Q_{XXX}/\Sigma Q_\phi$  values are quite independent of the resolution for disks with  $r_0 \geq 50$  mas and one can still recognize for a RingI60 model disk with  $r_0 \approx 25$  mas that the front side deviates more from the average than the back side. They are also practically the same for a convolution with  $\text{PSF}_G$  and  $\text{PSF}_{AO}$  and in very good agreement with the intrinsic values

$$\frac{\Delta Q_{XXX}}{\Sigma Q_\phi} \approx \frac{\Delta Q'_{XXX}}{\Sigma Q'_\phi}. \quad (16)$$

The equivalent quantities for the Stokes  $U$  quadrants are just ratios  $\Sigma U_{XXX}/\Sigma Q_\phi$  because the average value  $\Sigma U/4$  is zero. Figure 13 (lower right) shows, that the relative Stokes  $U$  quadrant ratios deviate for small disks with  $r_0 \lesssim 25$  mas substantially from a constant. This is caused by the morphology of the Stokes  $U$  map for the RingI60 model, which has one dominant positive  $U_{135}$  and one dominant negative  $U_{225}$  quadrant. Smearing and cancellation affect the weak quadrants  $\Sigma U_{045}$  and  $\Sigma U_{315}$  stronger than the reference value  $\Sigma Q_\phi$ , while the effects between the strong components  $U_{135}$  and  $U_{225}$  are smaller than for  $\Sigma Q_\phi$ , because the separation between the strong components is relatively large.

A useful alternative are the relative differential values between the  $U$  quadrants on the positive or negative  $x$ -axis side

$$\frac{\Delta U_+}{\Sigma Q_\phi} = \frac{\Sigma U_{135} - \Sigma U_{045}}{\Sigma Q_\phi} \quad \text{and} \quad \frac{\Delta U_-}{\Sigma Q_\phi} = \frac{\Sigma U_{225} - \Sigma U_{315}}{\Sigma Q_\phi}. \quad (17)$$

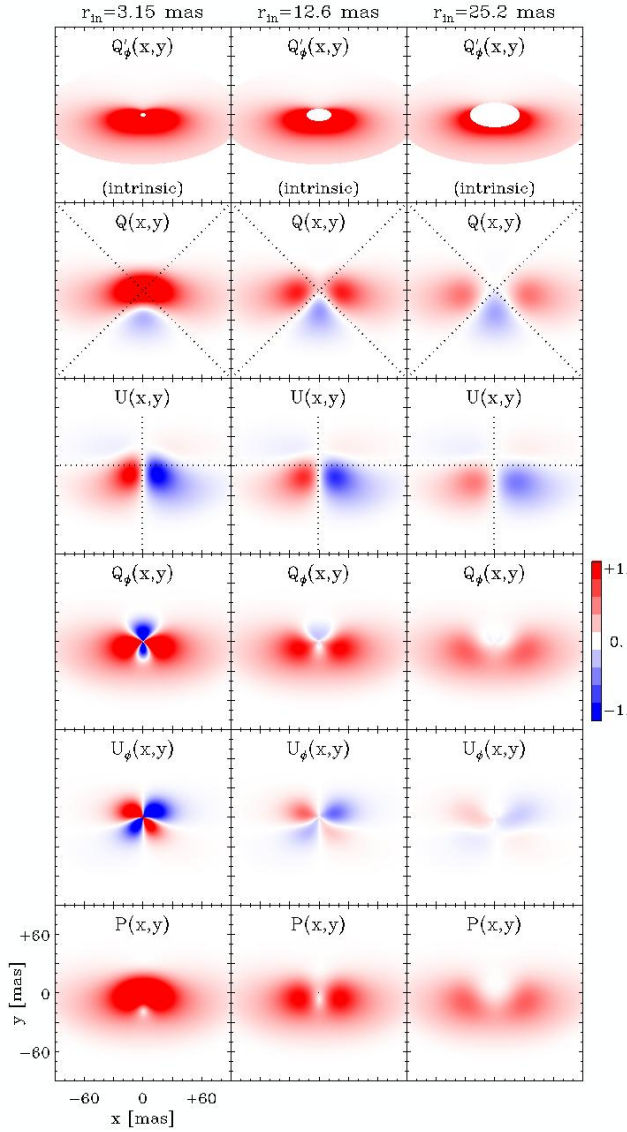


**Fig. 14.** Intrinsic maps  $Q'_\phi$  and PSF<sub>G</sub> convolved maps for  $Q$ ,  $U$ ,  $Q_\phi$ ,  $U_\phi$ , and  $P$  for DiskI60 $\alpha$ -2 models with different cavity sizes  $r_{\text{in}}$ . The radius  $r_{\text{out}} = 100.8$  mas and the intrinsic surface brightness (SB) profile  $Q'_\phi(r) \propto r^{-2}$  are the same for the three models.

There is  $\Delta U_+ = -\Delta U_-$  because of the symmetry of the RingI60 models. The ratio  $\Delta U_+/\Sigma Q_\phi$  is almost independent of the disk size  $r_0$  and the used PSF, according to the red line and points in Fig. 13 (lower right) and the values in Table D.2, very similar to the parameters  $\Delta Q_{\text{xxx}}/\Sigma Q_\phi$ . This demonstrates that differential quadrant parameters are useful to push the characterization of  $Q_\phi(\phi)$  and  $U_\phi(\phi)$  for circumstellar scattering regions towards smaller separations.

### 3.3. Convolution of inclined extended disks.

Extended disks with unresolved or partially unresolved central regions are frequently observed (e.g., Garufi et al. 2022) and it is of interest to investigate regions close to the star  $r < D_{\text{PSF}}$  because they correspond to the zone of terrestrial planet formation  $\lesssim 3$  AU for systems in nearby star forming regions. In particular, the polarization of the unresolved part of the disk at  $r \lesssim 0.5 D_{\text{PSF}}$  ( $< 12.6$  mas) can be compared with the polarization of the re-

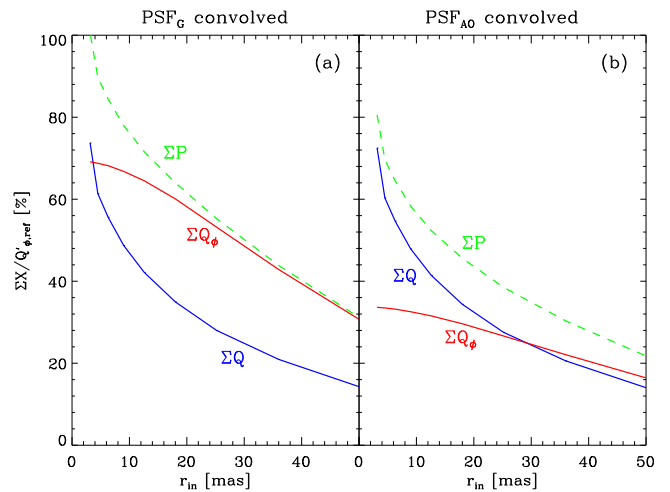


**Fig. 15.** Integrated polarization parameters  $\Sigma Q_\phi$ ,  $\Sigma P$ ,  $\Sigma Q'_\phi$  for the inclined DiskI60 $\alpha$ -2 model as function of the radius of the inner cavity  $r_{\text{in}}$  and for PSF<sub>G</sub> and PSF<sub>AO</sub> convolution. All values are normalized to the intrinsic value  $\Sigma Q'_\phi(r_{\text{in}} = 0.5 D_{\text{PSF}})$  (or  $r_{\text{in}} = 12.6$  mas).

solved region  $r \gtrsim D_{\text{PSF}}$  to constrain the presence or absence of significant changes in the scattering properties between the two regions.

Polarization maps for the inclined and extended DiskI60 $\alpha$ -2 models are plotted in Fig. 14 with radii for the inner cavities of  $r_{\text{in}} = 0.125 D_{\text{PSF}}$ ,  $0.5 D_{\text{PSF}}$ , and  $D_{\text{PSF}}$ , or  $3.15$  mas,  $12.6$  mas, and  $25.2$  mas, respectively. The inner disk rim is very bright for these models, and therefore the convolved disk maps look similar to the images in Fig. 9 for small disk rings. The model with  $r_{\text{in}} = D_{\text{PSF}}$  in Fig. 14 shows a resolved  $Q_\phi$  disk image with small cross-talk residuals in  $U_\phi$ , while the disk with a very small cavity of  $r_{\text{in}} = 0.125 D_{\text{PSF}}$  has strong quadrant patterns for  $Q_\phi$  and  $U_\phi$  as expected from the net  $Q$ -signal of a bright, unresolved central disk region.

The integrated polarization parameters for the DiskI60 $\alpha$ -2 models depend strongly on the inner disk radius  $r_{\text{in}}$  according to Fig. 15 or the numerical values given in Table D.3. The parameters are all normalized to the intrinsic azimuthal polarization  $Q'_{\phi,\text{ref}} = \Sigma Q'_\phi$  for the disk with  $r_{\text{in}} = 0.5 D_{\text{PSF}}$ . The intrinsic polarization parameters  $\Sigma Q'_\phi = \Sigma P'$  and  $\Sigma Q = \Sigma Q' = 0.421 \Sigma Q'_\phi$  are much larger for disks with small inner radii, for example by a factor 1.7 for  $r_{\text{in}} = 0.125 D_{\text{PSF}}$  when compared to  $r_{\text{in}} = 0.5 D_{\text{PSF}}$ . The convolution does not change the integrated Stokes polarization  $\Sigma Q = \Sigma Q'$  but only redistributes spatially the signal  $Q'(x, y) \rightarrow Q(x, y)$  and therefore the  $\Sigma Q$  curves are identical in the two panels of Fig. 15 for the models convolved with PSF<sub>G</sub> and PSF<sub>AO</sub>.

Contrary to this, the PSF convolution reduces or even cancels the strong  $\Sigma Q'_\phi$ -signal of the central region and the effect is more important for PSF<sub>AO</sub> than for PSF<sub>G</sub>. Therefore,  $\Sigma Q_\phi$  reaches for a given convolution PSF a limiting value for models with a cavity smaller than  $r_{\text{in}} < 0.5 D_{\text{PSF}}$ , despite the fact that the intrinsic  $\Sigma Q'_\phi$  and  $\Sigma Q'$  increase steeply for  $r_{\text{in}} \rightarrow 0$  for the DiskI60 $\alpha$ -2 model.

The central quadrant patterns in the convolved  $Q_\phi$  and  $U_\phi$  maps have a strength proportional to the net  $Q$  signal from the unresolved inner disk region. The central Stokes signal  $\Sigma Q_c \approx \Sigma Q(r \lesssim 0.5 D_{\text{PSF}})$  and  $\Sigma U_c$  can be used to constrain the amount of polarization  $P_c$  and the averaged polarization position angle ( $\theta_c = 0.5 \cdot \arctan 2(\Sigma U_c, \Sigma Q_c)$ ) for the unresolved part. Differences between  $\theta_c$  and the averaged polarization position angle

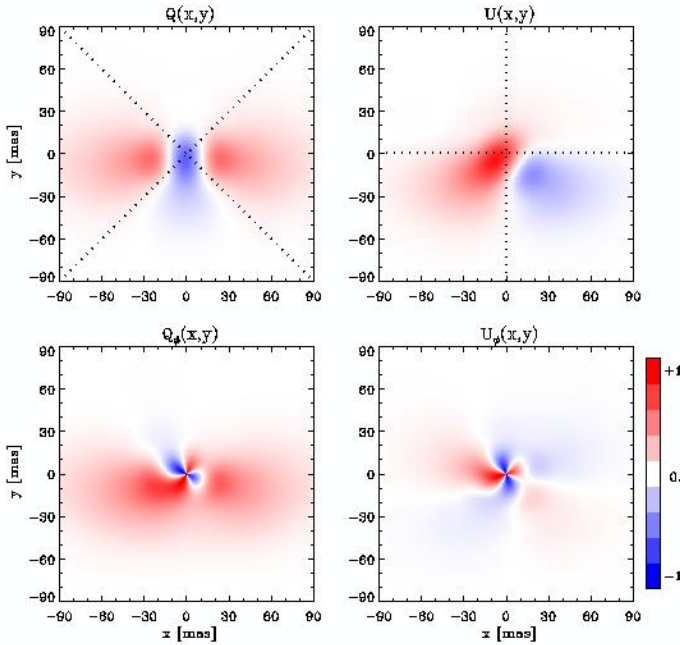


**Fig. 16.** Polarization maps  $Q$ ,  $U$ ,  $Q_\phi$ ,  $U_\phi$  for model DiskI60 $\alpha$ -2 ( $r_{\text{in}} = 0.5 D_{\text{PSF}}$  or 12.6 mas) and a polarized central star with  $\Sigma P'_s = 0.2 \cdot \Sigma Q'_{\phi,d}$  and  $\theta'_s = 67.5^\circ$  convolved with  $\text{PSF}_{\text{AO}}$ .

of the resolved signal  $\theta_d$  for  $\Sigma Q(r \gtrsim 0.5 D_{\text{PSF}})$  can point to a structural change between the unresolved and the resolved part of the scattering region, or to a contribution from interstellar or instrumental polarization as discussed in the next section.

The intrinsic profile  $Q'_\phi(r)$  for the DiskI60 $\alpha$ -2 models is steep and therefore the ratio of convolved parameters  $\Sigma Q / \Sigma Q_\phi$  changes strongly with the radius of the inner cavity  $r_{\text{in}}$  (Fig. 10). According to Table D.3 the dependence is smaller for the DiskI60 $\alpha$ -0 and DiskI60 $\alpha$ -1 models. Nonetheless,  $\Sigma Q / \Sigma Q_\phi$  could be a good parameter to derive from observational data the radius  $r_{\text{in}}$  of an unresolved central cavity or other disk properties at  $r < D_{\text{PSF}}$ , in particular when using constraints about disk inclination and SB profile from the resolved part of the disk at  $r \gtrsim D_{\text{PSF}}$ .

#### 3.4. The contribution of a polarized central star

The simulations presented up to now assume that the central star is unpolarized ( $Q'_s = 0$  and  $U'_s = 0$  in Eqs. 3,4), and therefore it does not affect the polarization signal of the circumstellar scattering region. However, often the stars with resolved circumstellar dust scattering regions have also unresolved components, as inferred for example from the thermal emission of hot dust. This dust can produce for the central, unresolved point-like source an intrinsic polarization, if scattering occurs in a non-symmetric structure. The central star can also be polarized by uncorrected contributions from interstellar or instrumental polarization. As the star is typically much brighter than the resolved circumstellar scattering already a small fractional polarization of the order  $p_s = \Sigma Q_s / \Sigma I_s \approx 0.001$  can have a strong impact on the observable polarization, and the following Sect. 4 will address the question on how to correct for this.

In this subsection we explore the impact of a polarized central source on the imaging polarimetry of a circumstellar scattering region. For this, we have to distinguish between the stellar

$Q_s$ ,  $U_s$  and circumstellar  $Q_d$ ,  $U_d$  polarization components. We consider a central point source with a fractional polarization  $p_s = (q_s^2 + u_s^2)^{1/2}$  and position angle  $\theta_s = 0.5 \cdot \text{atan2}(u_s, q_s)$  defined in disk coordinates  $(x, y)$ . The convolved intensity distribution of the central source is  $I_s(x, y) = \Sigma I_s \cdot \text{PSF}(x, y)$  and the corresponding Stokes parameter maps are  $Q_s(x, y) = q_s I_s(x, y)$  and  $U_s(x, y) = u_s I_s(x, y)$ . The integrated azimuthal polarization signals of the star are zero  $\Sigma Q_{\phi,s} = \Sigma U_{\phi,s} = 0$ , but the corresponding convolved signal maps show the quadrant patterns

$$Q_{\phi,s}(x, y) = -p_s I_s(x, y) \cos(2(\phi_{xy} - \theta_s)) \quad (18)$$

$$U_{\phi,s}(x, y) = +p_s I_s(x, y) \sin(2(\phi_{xy} - \theta_s)). \quad (19)$$

The strengths of these  $Q_{\phi,s}$  and  $U_{\phi,s}$  quadrant patterns are independent of  $\theta_s$  but their orientation is defined by  $\theta_s$ . The impact of the polarized intensity of the star  $\Sigma P_s = p_s \Sigma I_s$  on the disk polarization map in convolved data depends of course on the relative strength between  $\Sigma P_s$  and  $\Sigma Q_{\phi,d}$ .

Figure 16 shows as example a disk plus star system with an intrinsic ratio of  $\Sigma P'_s / \Sigma Q'_{\phi,d} = 0.2$  for a system with disk intensity  $\Sigma I'_d = 0.05 \Sigma I'_s$ , disk polarization  $\Sigma Q'_{\phi,d} = 0.1 \Sigma I'_d$ , and a stellar polarization of  $\Sigma P'_s = 0.001 \Sigma I'_s$ . The scattering region is simulated with the inclined disk model DiskI60 $\alpha$ -2 with  $r_{\text{in}} = 0.5 D_{\text{PSF}}$ . The star polarization has an orientation  $\theta_s = 67.5^\circ$  ( $q_s = -0.71 p_s$ ,  $u_s = +0.71 p_s$ ) and the whole system is convolved with  $\text{PSF}_{\text{AO}}$ . This reduces the azimuthal polarization  $Q_{\phi,d}$  of the disk and it results a ratio of  $\Sigma P_s / \Sigma Q_{\phi,d} = 0.635$  for the convolved model.

The polarization of the star has a strong impact on the polarization maps, despite the fact that  $\Sigma P_s$  is weaker than the circumstellar polarization  $\Sigma Q_{\phi,d}$ . This is apparent in the maps in Fig. 16, in particular when compared to the disk maps of Fig. 14 without stellar polarization. The star produces in the center of the Stokes  $Q(x, y)$  map a strong negative signal, and in  $U(x, y)$  the antisymmetric appearance for the inner disk region is distorted. For the azimuthal polarization strong quadrant patterns for  $Q_\phi(x, y)$  and  $U_\phi(x, y)$  are visible around the position of the central star.

The azimuthally averaged radial profiles for  $p_s I_s(r)$  and  $Q_{\phi,d}(r)$  in Fig. 17 show that the stellar polarization dominates strongly for  $r < 20$  mas, where the stellar intensity  $I_s(r)$  is much higher than the disk intensity  $I_d(r)$ , while the disk polarization is the main polarization component in the range  $r \approx 30$  to 120 mas.

There are three important properties for the interpretation of the polarization signal: (i) the integrated Stokes parameters do not depend on the PSF convolution and therefore the disk and star signal are just adding up

$$\Sigma Q = \Sigma P_s \cos(2\theta_s) + \Sigma Q_d, \quad (20)$$

$$\Sigma U = \Sigma P_s \sin(2\theta_s) + \Sigma U_d; \quad (21)$$

(ii)  $\Sigma Q_\phi$  and  $\Sigma U_\phi$  do not depend on the polarization signal of an unresolved central object, because the introduced quadrant patterns add no net signal  $\Sigma Q_{\phi,s} = 0$  and  $\Sigma U_{\phi,s} = 0$ ; (iii) the orientation of the central  $Q_\phi$  and  $U_\phi$  quadrant patterns are defined by  $\theta_s$  of the central source.

If the polarization of the central source is aligned with the resolved disk  $\theta_s = \theta_d$ , then we expect a left right symmetry  $Q_\phi(x, y) = Q_\phi(-x, y)$  for the overall Stokes  $Q_\phi$  map and an antisymmetry  $U_\phi(x, y) = -U_\phi(-x, y)$  for Stokes  $U_\phi$  like for the partially resolved disks shown in Fig. 14. Deviations from these properties are indicative for a more complicated polarization structure with a stellar polarization component not aligned with the disk polarization.

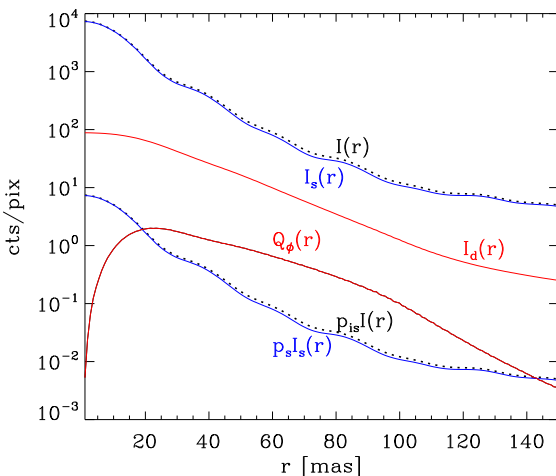


**Fig. 17.** Azimuthally averaged intensity profiles for the disk  $I_d(r)$ , the star  $I_s(r)$ , and the total  $I(r)$ , for the disk polarization  $Q_\phi(r)$ , and the intrinsic stellar polarization  $p_s I_s(r)$  or interstellar polarization  $p_{is} I(r)$  introduced by a fractional offset of  $p = 0.1\%$ . The same disk model, polarization offset  $p_s I_s(r)$ , and PSF<sub>AO</sub> convolution as in Fig. 16 is used, while the interstellar offset for  $p_{is} I(r)$  is applied to the total intensity.

**Interstellar and instrumental polarization.** The impact of polarization offsets from interstellar  $p_{is} I(x, y)$  or instrumental  $p_{inst} I(x, y)$  polarization are proportional to the total intensity, while an offset from an intrinsically polarized star  $p_s I_s(x, y)$  is proportional to the PSF of the star. However, for many typical cases one can approximate  $p_s I_s(x, y) \approx p_s I(x, y)$  because the difference between stellar and total intensity, which is equivalent to the scattered intensity from the dust  $I_d(x, y)$ , is very small for circumstellar scattering regions.

This is supported by the azimuthal profiles in Fig. 17 for the disk plus star model described above (Fig. 16). In this example the disk polarization in the range  $r \approx 30$  to 120 mas is much larger than the difference between the polarization offsets of  $p = 0.001$  for the total intensity and the stellar intensity  $Q_\phi(r) \gg (p(I(r) - I_s(r))$ . Therefore it makes for this example practically no difference for the disk polarization signal  $Q_\phi(x, y)$  whether one uses  $p I(x, y)$  or  $p I_s(x, y)$  for the polarization offset correction.

This approximation is also valid for faint circumstellar scattering regions, if the fractional scattering polarization is at the same level  $\Sigma Q_\phi \approx 0.1 \Sigma I_d$  as in the example shown above, because the difference for the two cases of polarization offsets scales still with  $\Sigma I_d$  according to  $p(I(r) - I_s(r)) = p I_d(r)$ . The approximation  $I \approx I_s$  is less good for a bright scattering region  $I_d$ , in particular if the polarization offsets is large  $p \gtrsim 0.01$  and the scattering region weakly polarized  $\Sigma Q_\phi / \Sigma I_d \lesssim 0.1$ , and combination of these cases.

We treat in this study an intrinsic stellar polarization like an interstellar polarization offset. Interstellar and instrumental polarization offsets can be corrected using  $p_{is} I(x, y)$  or  $p_{inst} I(x, y)$  with the advantage, that the system intensity  $I(x, y)$  can be derived from unsaturated observations of the target. In the best case  $I(x, y)$  is obtained simultaneously with the polarization signal  $Q(x, y)$  and  $U(x, y)$  so that atmospheric variations can be taken accurately into account (e.g., Tschudi & Schmid 2021). Using the system intensity  $I(x, y)$  also as approximation for the correction of an intrinsic stellar polarization  $p_s I(x, y) \approx p_s I_s(x, y)$  overestimates slightly the offset, but avoids the difficult procedure of splitting  $I(x, y)$  into a stellar PSF component  $I_s(x, y)$  and

a disk component  $I_d(x, y)$ . Using  $I_s(x, y)$  instead of  $I(x, y)$  would provide in many cases only a marginal improvement for the offset correction when considering other PSF calibration issues in high contrast imaging polarimetry.

## 4. Polarimetric calibration and zp-correction

### 4.1. The impact of a fractional polarization offset

Already a small fractional polarization offset of the order  $p \approx 0.1\%$  from an intrinsic polarization of the central star, from interstellar polarization, or from instrumental polarization can have a strong impact on the observed polarization maps of circumstellar scattering regions (Fig. 16). Unfortunately, the different polarization effects are often not well known and after a calibration there can remain non-negligible polarization residuals  $p_{res}$  with an arbitrary position angle  $\theta_{res}$ , or residual fractional Stokes values  $q_{res}$  and  $u_{res}$

$$Q_{obs}(\alpha, \delta) \approx Q(\alpha, \delta) + q_{res} I(\alpha, \delta), \quad (22)$$

$$U_{obs}(\alpha, \delta) \approx U(\alpha, \delta) + u_{res} I(\alpha, \delta). \quad (23)$$

This can also be expressed by integrated parameters

$$\Sigma Q_{obs} = \Sigma Q + q_{res} \Sigma I \quad (24)$$

and equivalent for Stokes  $U$ . The residual offset  $p_{res} \Sigma I$  can strongly disturb or even dominate the weak polarization signal  $Q_d, U_d$  of the circumstellar scattering region. The standard method to improve the situation is a polarimetric zp-correction, which cancels the integrated Stokes signals

$$\Sigma Q^z = \Sigma Q_{obs} - \langle q_{obs} \rangle \Sigma I = 0, \quad (25)$$

$$\Sigma U^z = \Sigma U_{obs} - \langle u_{obs} \rangle \Sigma I = 0, \quad (26)$$

in a certain aperture  $\Sigma$  using the fractional Stokes parameters  $\langle q_{obs} \rangle = \Sigma Q_{obs} / \Sigma I$  and  $\langle u_{obs} \rangle = \Sigma U_{obs} / \Sigma I$  (e.g., Quanz et al. 2011; Avenhaus et al. 2014). This is a powerful method to find the circumstellar polarization component in data dominated by residual interstellar, instrumental, or stellar polarization offsets.

The zp-correction is also very useful for data, where a circumstellar polarization is detected, but where the signal might be affected by an unknown offset  $q_{res}$ . Because  $\langle q_{obs} \rangle = \Sigma Q / \Sigma I + q_{res}$  according to Eq. 24 and using Eq. 25 gives

$$\Sigma Q^z = \Sigma Q - \langle q \rangle \Sigma I = 0 \quad (27)$$

with  $\langle q \rangle = \Sigma Q / \Sigma I$  and equivalent for  $\Sigma U^z$ . This means, that the zp-corrected signals of a Stokes map with a fractional polarization offset, e.g. because of calibration uncertainties, is equal to the zp-corrected signal of the map without offsets like for perfectly calibrated data. Therefore, the zp-correction provides data with a well defined offset correction, which can be re-calibrated later  $Q^z(\alpha, \delta) \rightarrow Q(\alpha, \delta)$  in a second step once the intrinsic offset value  $\langle q \rangle$  is known from more accurate polarimetry or constraints from scattering models. For example, for a given object the same zp-corrected Stokes signals  $\Sigma Q^z, \Sigma U^z$  should result for data affected by different instrumental polarization offsets  $p_{res}$ . The Stokes maps  $Q^z(\alpha, \delta), U^z(\alpha, \delta)$  still depend on the observational PSF.

The zp-correction has practically no impact on the integrated azimuthal polarization  $\Sigma Q_\phi$ , and there is

$$\Sigma Q_\phi^z \approx \Sigma Q_\phi. \quad (28)$$

because a fractional Stokes polarization offset introduces for the  $Q_\phi(\alpha, \delta)$  and  $U_\phi(\alpha, \delta)$  maps positive-negative quadrant patterns

with a zero net signal. Therefore,  $\Sigma Q_\phi$  is a very robust quantity, which is hardly affected by polarization offsets introduced by calibration uncertainties. However, it is important to note that the zp-correction changes the signal distribution in the Stokes maps  $Q^z(\alpha, \delta)$ , and  $U^z(\alpha, \delta)$  and this can produce a strong bias for the measured azimuthal distribution of the  $Q_\phi^z(\phi)$  polarization which must be considered for the interpretation of zp-corrected data.

#### 4.2. Cases without zp-correction bias

Polarimetric calibration uncertainties can be corrected with a zp-correction without introducing a bias, if the central source is intrinsically unpolarized ( $\Sigma Q'_s \approx 0$ ,  $\Sigma U'_s \approx 0$  or  $\Sigma Q_d = \Sigma Q$ ,  $\Sigma U_d = \Sigma U$ ) and can be used as zero polarization reference. The zp-correction value  $\langle q_1 \rangle = \Sigma_1 Q / \Sigma_1 I$  derived for a small stellar aperture  $\Sigma_1$  accounts then for the polarization offsets  $q_{\text{res}}$  introduced by the interstellar and instrumental polarization according to

$$Q^{z1}(\alpha, \delta) = Q(\alpha, \delta) + q_{\text{res}} I(\alpha, \delta) - \langle q_1 \rangle I(\alpha, \delta) \approx Q(\alpha, \delta) \quad (29)$$

and equivalent for Stokes  $U^{z1}$ . This approximation assumes that the scattering region does not contribute to the polarization signal in  $\Sigma_1$ .

The central star cannot be used as calibration source for coronagraphic observations. However, if the object has an axisymmetric scattering geometry with zero or close to zero net polarization  $\Sigma_2 Q \approx 0$  and  $\Sigma_2 U \approx 0$ , measured in an annular aperture  $\Sigma_2$ , then this signal can be used as zero polarization reference. Good examples for such axisymmetric systems are circumstellar disks seen pole-on, like for TW Hya, HD 169142 or RX J1604 (Rapson et al. 2015; van Boekel et al. 2017; Poteet et al. 2018; Tschudi & Schmid 2021; Ma et al. 2023).

#### 4.3. Bias introduced by the polarimetric zp-correction

The zp-correction is usually applied to the  $Q(\alpha, \delta)$  and the  $U(\alpha, \delta)$  frames in the sky coordinate system. We investigate the zp-correction effects in the  $(x, y)$  coordinate system of inclined disks, because the impact of polarization offsets does not depend on the orientation of the selected coordinate system. This simplifies the comparison of  $Q^z(x, y)$ ,  $U^z(x, y)$  with the signal of the convolved models  $Q(x, y)$ ,  $U(x, y)$  representing perfectly calibrated data. The corrected signal depends on the selected correction region  $\Sigma_{\text{zp}}$  and different cases are considered including the zp-correction of coronagraphic data, or systems with partly unresolved disks.

##### 4.3.1. ZP-correction for an inclined disk ring model

We consider the inclined model RingI60 with  $r_0 = 100.8$  mas in  $(x, y)$ -coordinates convolved with the extended PSF<sub>AO</sub>, apply a zp-correction, and compare the corrected Stokes signal  $Q^z(x, y)$  with the corresponding disk signal  $Q(x, y)$  without offsets. An overview on the used polarization parameters for zp-corrected models is given in Table A.2.

The zp-correction offset derived from a large aperture  $\Sigma_{\text{zp}} = \Sigma$  with a radius of  $r = 1.5''$  yields for the corrected signal integrated in the same aperture  $\Sigma Q^z = \Sigma Q - \langle q \rangle \Sigma I = 0$  according to Eq. 27. This procedure compensates the positive disk polarization  $\Sigma Q$  by a negative offset  $-\langle q \rangle \Sigma I$ . The spatial distribution of the Stokes  $Q$  signal differs between the zp-corrected and the initial signals by

$$\Delta Q(x, y) = Q^z(x, y) - Q(x, y) = -\langle q \rangle I(x, y). \quad (30)$$

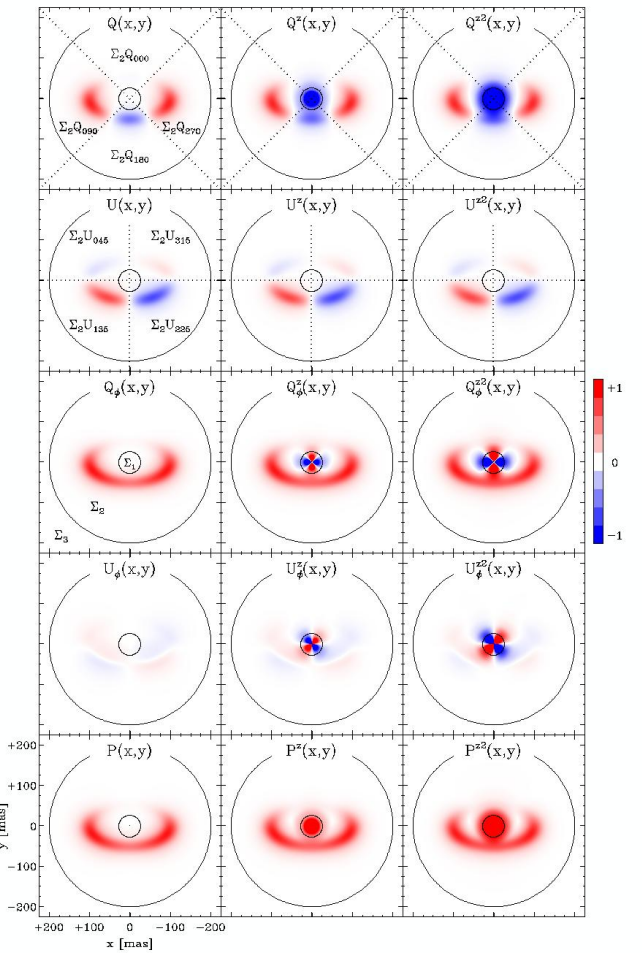


**Fig. 18.** Polarization maps for the RingI60 model with  $r_0 = 100.8$  mas convolved with PSF<sub>AO</sub>. The columns shows from left to right the convolved maps  $X(x, y)$ , the maps  $X^z(x, y)$  for a system zp-correction, and  $X^{z2}(x, y)$  for disk zp-correction. The circles describe the integration regions  $\Sigma_1$ ,  $\Sigma_2$ , and  $\Sigma_3$  as indicated in the  $Q_\phi(x, y)$  panel and quadrant regions  $\Sigma_2 X_{\text{xxx}}$  are identified in the  $Q(x, y)$  and  $U(x, y)$  panels.

For Stokes  $U$  there is  $U^z(x, y) = U(x, y)$  for the RingI60 models because  $\Sigma U = 0$  and therefore  $\langle u \rangle = 0$ . Thus, a Stokes  $Q$  zp-correction has no impact on the Stokes  $U$  signal and contrariwise. Therefore the zp-correction effects described for Stokes  $Q$  can be generalized to an offset with  $Q$  and  $U$  components.

The zp-correction effects are illustrated in Fig. 18 with RingI60 maps of the polarization parameters  $X = \{Q, U, Q_\phi, U_\phi, P\}$  for the convolved model  $X(x, y)$ , the  $\Sigma_{\text{zp}} = \Sigma$  corrected model  $X^z(x, y)$ , and the  $\Sigma_2$  corrected case  $X^{z2}(x, y)$  to be discussed later (Sect. 4.3.3). For Stokes  $Q$  a strong negative signal is introduced in the  $Q^z(x, y)$  map at the position of the star, and because of the extended PSF<sub>AO</sub>, there are also negative contributions further out. Therefore, the corrected polarization  $Q^z$  is also lower than  $Q$  at the location of the disk ring, while there is no difference between  $U^z(x, y)$  and  $U(x, y)$ . The zp-corrected azimuthal polarizations  $Q_\phi^z(x, y)$  and  $U_\phi^z(x, y)$  show the additional quadrant patterns for a convolved central point source with a negative Stokes  $Q$  polarization. For the polarized intensity  $P$  the offset  $-\langle q \rangle \Sigma I$  adds predominantly a positive component to the  $P^z(x, y)$  map.

The impact of the zp-correction in the Stokes polarization maps depends on the separation from the center and therefore

we consider besides the total system integration region  $\Sigma_{\text{int}} = \Sigma$  also three radial integration regions  $\Sigma_1$ ,  $\Sigma_2$ , and  $\Sigma_3$  indicated in Fig. 18 in the  $Q_\phi(x, y)$  panel. They represent the star, the disk and the halo regions, respectively, and there is  $\Sigma = \Sigma_1 + \Sigma_2 + \Sigma_3$ .

In the following a detailed description for the system corrected map  $Q^z(x, y)$  in Fig. 18 is given. The negative signal  $\Sigma_1 Q^z$  in the stellar aperture  $\Sigma_1$  with  $r < 0.027''$  introduced by the zp-correction can be estimated using  $\Sigma_1 Q^z = \Sigma_1 Q - \langle q \rangle \Sigma_1 I$ , which is Eq. 27 applied to the integration region  $\Sigma_1$ . The disk contribution is very small  $\Sigma_1 Q \approx 0$  and the PSF<sub>AO</sub> convolved intensity  $\Sigma_1 I$  is about 40 % of the total intensity  $\Sigma I$  (see Table E.1 for accurate values) and we obtain

$$\Sigma_1 Q^z \approx -\langle q \rangle \Sigma_1 I \approx -0.4 \Sigma Q \quad (31)$$

In the halo region  $\Sigma_3$  ( $0.2'' < r < 1.5''$ ) there is roughly everywhere the same fractional polarization  $Q(x, y)/I(x, y) \approx \Sigma_3 Q/\Sigma_3 I \approx \langle q \rangle$  for the convolved model, because far from the center the PSF<sub>AO</sub> smearing of the intrinsic Stokes signal  $Q'(x, y)$  of a compact disk is very similar to the smearing of the total intensity  $I'(x, y)$  dominated by the central star. Therefore, the halo signal is practically cancelled by the zp-correction and Eq. 27 for  $\Sigma_3$  can be approximated by

$$\Sigma_3 Q^z \approx 0. \quad (32)$$

Of importance for the analysis of the disk polarization is the annular aperture  $\Sigma_2$  with  $0.027'' < r < 0.2''$  covering the disk and there is (using Eq. 27 for  $\Sigma_2$ )

$$\Sigma_2 Q^z = \Sigma_2 Q - \langle q \rangle \Sigma_2 I. \quad (33)$$

Because  $\Sigma Q^z = 0$  for the entire system  $r < 1.5''$ , and  $\Sigma_3 Q^z \approx 0$  for the halo, the polarization for the zp-corrected disk region  $\Sigma_2 Q^z$  is equal to the the negative signal of the central star or

$$\Sigma_2 Q^z \approx -\Sigma_1 Q^z \approx \langle q \rangle \Sigma_1 I, \quad (34)$$

where the second relation is equal to Eq. 31. The Stokes  $Q$  polarization is after zp-correction  $\Sigma_2 Q^z \approx +0.44 \Sigma Q$ , which is significantly lower than for the non-corrected disk  $\Sigma_2 Q \approx +0.71 \Sigma Q$  (Table E.1). Thus, the zp-correction introduces for the PSF<sub>AO</sub> convolved RingI60 model a strong bias for Stokes  $Q$ , changing also the angular distribution of the azimuthal polarization  $Q_\phi^z(\phi)$ .

#### 4.3.2. ZP-correction and quadrant polarization parameters

The intrinsic angular distribution of the azimuthal polarization  $Q_\phi(\phi)$  is changed in polarimetric observations, first by the instrumental convolution as described by the quadrant parameters  $\Sigma X_{xxx}$  in Sect. 3.2.4, and, if applied, also by the polarimetric zp-correction. A Stokes  $Q$  zp-correction adds a signal  $-\langle q \rangle I(x, y)$ , and because we adopted only axisymmetric PSFs and approximate  $I(x, y) \approx I_s(x, y)$ , this introduces for all Stokes quadrants  $\Sigma_{\text{int}} Q_{xxx}$  practically the same offset. These simple dependencies of the quadrant parameters is very useful to describe the convolution and zp-correction effects of the observed azimuthal polarization signal  $Q_\phi(\phi)$ , which contains important information about the scattering geometry and the dust scattering properties.

The impact of the convolution and zp-correction are illustrated in Fig. 19 (upper panels) for the RingI60 ( $r_0 = 100.8$  mas) model with the quadrant polarization parameters  $\Sigma_2 X_{xxx}$  (diamonds) measured inside the integration region  $\Sigma_2$  extending from  $r = 27$  mas to 200 mas as defined in Fig. 18 (panels  $Q(x, y)$  and  $U(x, y)$ ). The quadrant values  $X_{xxx}$  represent different azimuthal parts  $\phi_{xxx}$  of the polarizaton signal  $Q_\phi(\phi)$ , but one needs

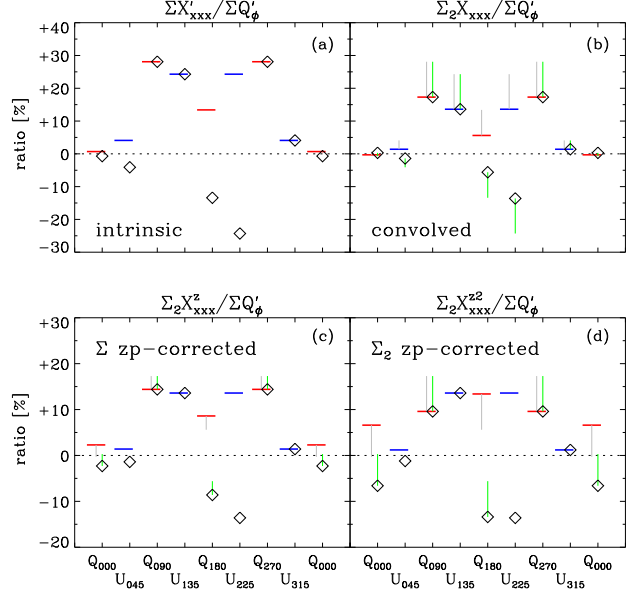


**Fig. 19.** Relative quadrant polarization parameters  $\Sigma_2 X_{xxx}$  ( $\diamond$ ) and their azimuthal values  $\Sigma_2 X_{xxx}|_\phi$  (horizontal bars) for the disk integration region  $\Sigma_2$  for RingI60 with  $r_0 = 100.8$  mas: (a) intrinsic model, (b) convolved model, (c)  $\Sigma$  corrected, and (d)  $\Sigma_2$  corrected models. The green and grey lines in (b) indicate the change of  $\Sigma_2 X_{xxx}$  and  $\Sigma_2 X_{xxx}|_\phi$ , respectively, with respect to panel (a), and in the panels (c) and (d) with respect to panel (b). All values are normalized to  $\Sigma Q'_\phi$ .

also to consider whether the sign of  $X_{xxx}$  corresponds to a positive or negative contributions to the azimuthal polarization  $Q_\phi$ . Therefore, we define azimuthal quadrant values  $\Sigma_i X_{xxx}|_\phi$ , which account for the sign of the Stokes polarization with respect to  $Q_\phi(\phi_{xxx})$  as follows:

- for the Stokes  $Q$  quadrants  $\Sigma_i Q_{000}|_\phi = -\Sigma_i Q_{000}$ ,  $\Sigma_i Q_{090}|_\phi = +\Sigma_i Q_{090}$ ,  $\Sigma_i Q_{180}|_\phi = -\Sigma_i Q_{180}$ , and  $\Sigma_i Q_{270}|_\phi = +\Sigma_i Q_{270}$ ,
- and for the Stokes  $U$  quadrants  $\Sigma_i U_{045}|_\phi = -\Sigma_i U_{045}$ ,  $\Sigma_i U_{135}|_\phi = +\Sigma_i U_{135}$ ,  $\Sigma_i U_{225}|_\phi = -\Sigma_i U_{225}$ , and  $\Sigma_i U_{315}|_\phi = +\Sigma_i U_{315}$ .

The  $\Sigma_i X_{xxx}|_\phi$  values are plotted in Fig. 19 as horizontal bars. For the intrinsic disk model they are just equal to the absolute value of the quadrant values  $\Sigma X'_{xxx}|_\phi = |\Sigma X'_{xxx}|$ , but this is not always the case for convolved and corrected models. From the change of the  $\Sigma_i X_{xxx}|_\phi$  values for the different cases one can estimate the change of the azimuthal distribution of  $Q_\phi(\phi)$  for angles  $\phi_{xxx}$  representative for a particular quadrant.

The convolution changes the relative strengths of the quadrants as already described in Sect. 3.2.4 for the total system integration region  $\Sigma$ . In this section, we concentrate on the quadrant signals in the disk integration region  $\Sigma_2$  of the model RingI60 ( $r_0 = 100.8$  mas) and in Fig. 19 (panel b) the differences between the intrinsic and the convolved quadrant values  $\Sigma_2 X_{xxx}$  (diamonds) are illustrated by the vertical green lines and for the azimuthal quadrant values  $\Sigma_2 X_{xxx}|_\phi$  (bars) by grey lines. The mutual cancellation and the smearing of signal into the halo region  $\Sigma_3$  reduces the signal in  $\Sigma_2$  for the positive quadrants and enhances it for the negative quadrants and this corresponds to a substantial reduction of the absolute quadrant values  $|\Sigma_2 X_{xxx}|$  and of the corresponding azimuthal values  $\Sigma_2 X_{xxx}|_\phi$  in step with reduction for  $\Sigma Q_\phi$  (see also Table E.1).

The zp-correction compensates the disk polarization  $\Sigma_2 Q$  by adding a negative signal  $-\Sigma_2 Q$  with a distribution like  $I(x, y)$  and

this reduces the polarization in  $\Sigma_2$  by  $\Delta_2 Q = \Sigma_2 Q^z - \Sigma_2 Q = -\langle q \rangle \Sigma_2 I$  according to Eq. 33. For the RingI60 model with  $r_0 = 100.8$  mas the effect is equal to  $\Delta_2 Q / \Sigma_2 Q'_\phi = -11.2\%$  (Table E.1). All the Stokes  $Q$  quadrant values are changed by roughly the same amount

$$\Sigma_2 Q_{xxx}^z \approx \Sigma_2 Q_{xxx} + (\Delta_2 Q) / 4, \quad (35)$$

with  $(\Delta_2 Q / 4) / \Sigma_2 Q'_\phi \approx -2.8\%$ . The Stokes  $U$  quadrants are not changed, because  $\Sigma_2 U = 0$  for the used model. Also the integrated azimuthal polarization  $\Sigma_2 Q_\phi$  is practically not changed by the zp-correction offset.

Because of the correspondence between  $Q_\phi(\phi)$  for different  $\phi$ -wedges and the azimuthal quadrant parameters, the negative  $\Sigma_2 Q / 4$  contribution is equivalent to a positive contribution for  $\Sigma_2 Q_{000} |_\phi$  and  $\Sigma_2 Q_{180} |_\phi$ , and a negative contribution for  $\Sigma_2 Q_{090} |_\phi$  and  $\Sigma_2 Q_{270} |_\phi$  as illustrated by the grey vertical lines in panel (c) of Fig. 19. This zp-correction enhances the relative signal of the disk front side by more than 50% or from  $\Sigma_2 Q_{180} |_\phi / \Sigma_2 Q'_\phi = 5.6\%$  to  $\Sigma_2 Q_{180}^z |_\phi / \Sigma_2 Q'_\phi = 8.6\%$  between the “non-corrected” and the zp-corrected disk maps (Table E.1). If one compares the ratio  $\Sigma_2 Q_{180} |_\phi / \Sigma_2 Q_{090} |_\phi$  between the signal on the front side with respect to the signal in the left or right quadrants, which are reduced by the zp-correction then the initial ratio is boosted from  $\Sigma_2 Q_{180} |_\phi / \Sigma_2 Q_{090} |_\phi = 0.32$  to  $\Sigma_2 Q_{180}^z |_\phi / \Sigma_2 Q_{090} |_\phi = 0.60$ , or almost a factor of two. This example illustrates that the azimuthal distribution of the polarization signal  $Q_\phi(\phi)$  can be very significantly changed by a polarimetric zp-correction.

#### 4.3.3. ZP-correction for coronagraphic observations

Annular apertures must be used for the zp-correction of coronagraphic observations or data with detector saturation at the position of the bright central star. Thus, one needs to consider other zp-correction regions than  $\Sigma_{zp} = \Sigma$  for the whole system. The resulting zp-corrected maps, integrated Stokes parameters, or quadrant parameters are identified with a superscript like  $Q^{z^2}$ ,  $Q^{z^3}$  or  $Q^{z^{2+3}}$  for zp-corrections applied to the annuli  $\Sigma_{zp} = \Sigma_2$ ,  $\Sigma_3$  or  $\Sigma_{2+3}$  representing the disk region, the halo region, or the disk plus halo region, respectively. Table E.1 gives an overview on how the polarization parameters for different integration regions  $\Sigma_i$  depend on the used correction region  $\Sigma_{zp}$  for the model RingI60 with  $r_0 = 100.8$  mas. Important are the resulting polarization values for the annular aperture  $\Sigma_2$  which includes the disk ring.

The zp-correction applied to a given annulus  $\Sigma_{zp} = \Sigma_i$  sets the corrected Stokes value in this region  $\Sigma_i Q^{zi}$  to zero according to  $\Sigma_i Q^{zi} = \Sigma_i Q - \langle q_{zi} \rangle \Sigma_i I = 0$ , which is a generalization of Eq. 27. Selecting different zp-correction regions introduces different offsets  $\langle q_{zi} \rangle$  factors and for the RingI60 models the  $\langle q_{zi} \rangle$  values behave like

$$\langle q_2 \rangle > \langle q_{2+3} \rangle > \langle q_3 \rangle \quad \text{and} \quad \langle q_3 \rangle \approx \langle q \rangle. \quad (36)$$

**ZP-correction for the disk.** The largest offset  $\langle q_2 \rangle$  results for a zp-correction based on the disk region with a strong positive  $\Sigma_2 Q$  polarization. This sets  $\Sigma_2 Q^{z^2}$  polarization to zero, or the positive quadrants ( $\Sigma_2 Q_{090}^{z^2} + \Sigma_2 Q_{270}^{z^2}$ ) equal to the negative quadrants  $-(\Sigma_2 Q_{000}^{z^2} + \Sigma_2 Q_{180}^{z^2})$  and produces apparently a very strong  $\Sigma_2 Q_{180}^{z^2} |_\phi$  signal for the disk front side as shown in panel (d) of Fig. 19 (Table E.1). This is only a zp-correction effect and should not be interpreted as real azimuthal distribution of the  $Q_\phi(\phi)$  signal, as would be expected for a disk with highly forward scattering dust.

Moreover, the derived correction offset  $\langle q_2 \rangle \Sigma_2 I = \Sigma_2 Q$  depends on the quality of the PSF. It is difficult to account for this, particularly for extended disks without sharp structures as in the RingI60 models. Thus, whenever possible one should avoid a zp-correction based on the disk region. This can be problematic for coronagraphic observation of faint disks with large outer radii  $r_0$ , where the halo region  $r > r_0$  has not enough signal for a well defined offset correction.

A zp-correction based on the whole region outside the coronagraphic mask  $\Sigma_{zp} = \Sigma_{2+3}$  reduces the correction offset (Table E.1). In the halo the smeared stellar intensity dilutes more efficiently the smeared disk Stokes signal, and there is  $\langle q_{2+3} \rangle < \langle q_2 \rangle$ . Thus, the zp-correction offset is reduced, but it depends still significantly on the PSF profile.

**ZP-correction for the halo.** For the halo there is  $\langle q_3 \rangle \approx \langle q \rangle$  because the smearing of a  $\Sigma Q$  signal of a compact disk model like RingI60 with  $r_0 = 100.8$  mas is very similar to the smearing of the intensity, which is dominated by the star. Therefore the halo zp-corrected disk polarization is practically identical to the system zp-corrected signal (Table E.1), or

$$\Sigma_2 Q^{z^3} \approx \Sigma_2 Q^z. \quad (37)$$

The offset defined by the system zp-correction  $-\langle q \rangle \Sigma I$  does not depend on the PSF profile, and this is also the case for the halo corrected models. This also applies, at least approximately, for coronagraphic observations and they should be corrected based on the halo region  $\Sigma_{zp} = \Sigma_3$  outside the disk because of the well defined and relatively small bias offset.

For coronagraphic observations or data with detector saturation at the position of the star there is the fundamental issue that the PSF profile and the total intensity of the system  $\Sigma I$  cannot be derived from the same data. Flux and PSF calibrations are therefore required for quantitative measurements to allow for a correction of the convolution effects and to relate the measured polarization signal to the intensity of the central star, which is typically a good flux reference.

**Coronagraphic observations of a large ring.** A RingI60 model with  $r_0 = 403.2$  mas convolved with PSF<sub>AO</sub> provides a good example for the effects of a zp-correction for coronagraphic observations of an extended disk taken with a currently available instrument. Figure 20 shows the Stokes  $Q(x, y)$  map, and the zp-corrected maps  $Q^{z^3}(x, y)$ ,  $Q^{z^{2+3}}(x, y)$ , and  $Q^{z^2}(x, y)$  while corresponding numerical values are given in Tab. E.2. The  $\Sigma_1$  region with the central star is defined by  $r < 100$  mas and assumed to be covered by a coronagraphic mask. The region  $\Sigma_2$  with the circumstellar disk is described by the annulus  $0.1'' < r < 0.5''$  and  $\Sigma_3$  for the halo by  $0.5'' < r < 1.5''$ . A very narrow color scale was selected to illustrate the weak extended signal.

The intrinsic disk has a positive net signal  $\Sigma Q$  and this produces in the convolved map  $Q(x, y)$  an extended halo with a faint, positive  $Q$  signal (Fig. 20(a)). A zp-correction applied to the coronagraphic data  $\Sigma_{zp} = \Sigma_{2+3}$  cancels the net positive polarization in the  $\Sigma_{2+3}$  region and this turns the positive background in  $Q(x, y)$  into a negative background in the corrected map for  $Q^{z^{2+3}}$  (Fig. 20(c)). Moreover, the subtraction  $-\langle q_{2+3} \rangle I(x, y)$  produces a quite significant ring of negative  $Q$  polarization at the position of the PSF speckle ring typical for AO systems. This correction artifact can disturb significantly the analysis despite the fact that the disk signal is very well resolved. The bias effects is smaller, if the halo region is used for the zp-correction

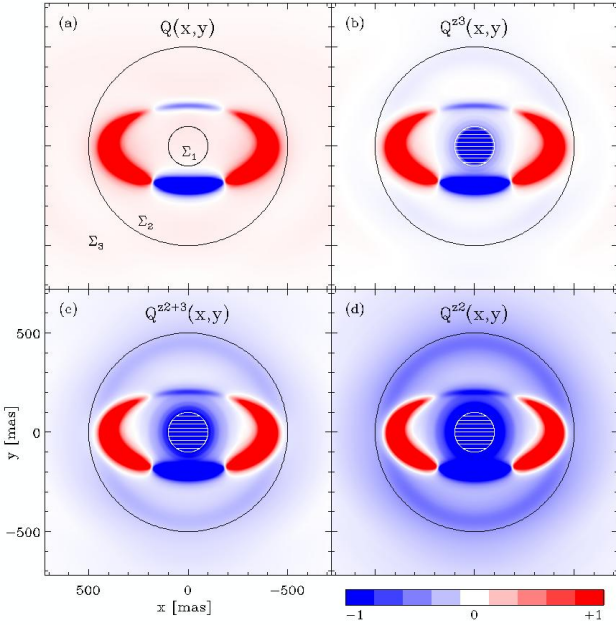


**Fig. 20.** Effects of the zp-correction for Stokes  $Q$  for the  $\text{PSF}_{\text{AO}}$  convolved Ring160 model with large  $r_0 = 403.2$  mas for observations with a coronagraphic mask as indicated by the hatched central area. Panel (a) show the convolved signal  $Q(x, y)$ , (b) the map after a correction based on the halo  $Q^{z3}$ , (c) on the disk plus halo  $Q^{z2+3}$ , and (d) on the disk  $Q^{z2}$ . The peak  $Q$  signal is in all panels between 22 to 23 units with respect to the indicated color scale.

$\Sigma_{\text{zp}} = \Sigma_3$  and larger, if only the disk region is used  $\Sigma_{\text{zp}} = \Sigma_2$  (see Fig. 20(b,d) or Tab. E.2).

Determining the zp-offset  $\langle q_3 \rangle$  from the halo is therefore also for coronagraphic observations of extended disks, like the example in Fig. 20, a good approach for a well defined  $\langle q_3 \rangle \approx \langle q \rangle$  zero point correction. For this, one should select a region which represents well the average fractional polarization of the system, like the region outside the AO speckle ring. This feature should be avoided, because it overrepresents the stellar contribution.

**Speckle ring as stellar polarization signal.** The AO speckle ring in high contrast coronagraphic data can be strong and could be used to measure or estimate the polarization of the star  $\Sigma Q_s / \Sigma I_s$  and  $\Sigma U_s / \Sigma I_s$ . The requirement is, that stellar light in the speckle ring can be separated well from the circumstellar scattering signal.

This could be the case for a small scattering region located clearly between coronagraphic mask and the stellar speckle ring in particular if the disk polarization has a small net Stokes  $Q$  and  $U$  signal so that the smeared halo of the disk is almost unpolarized. The polarization of the stellar speckle ring can probably also be measured quite well a circumstellar regions similar to the coronagraphic model in Fig. 20, because the speckle halo at  $\Delta y \pm 450$  mas above and below the star is well separated from the disk signal.

The derived fractional polarization from the stellar speckles can then be used as approximation for  $\Sigma Q_s / \Sigma I_s$  and  $\Sigma U_s / \Sigma I_s$  and be used for a polarimetric zp-correction. If the star is unpolarized, then one would get well calibrated coronagraphic polarization data  $Q(x, y)$  and  $U(x, y)$  like for the case described in Sect. 4.2. Applying specific procedures for a given data set must probably be considered to achieve the best results, but this is beyond the scope of this paper.

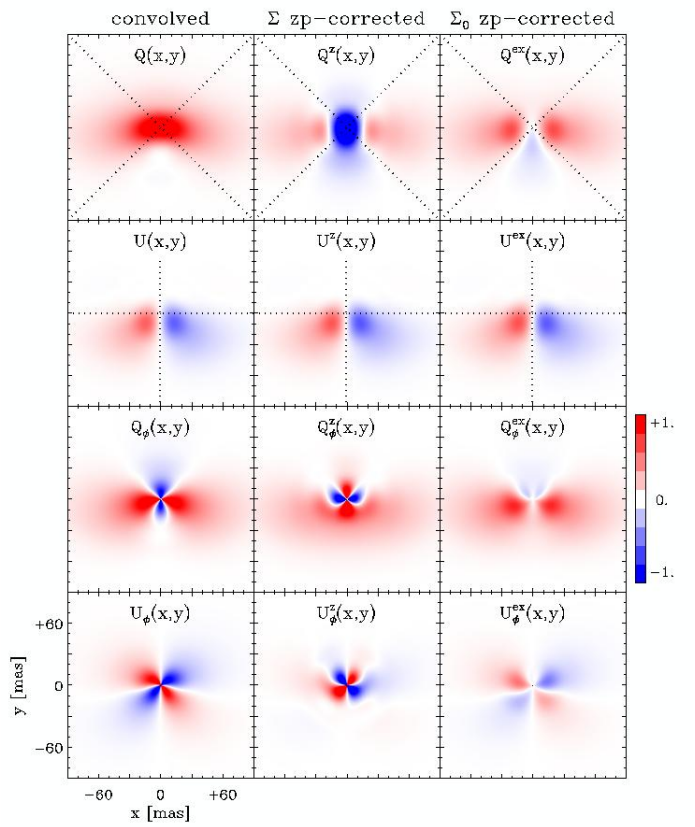


**Fig. 21.** ZP-correction effects for DiskI60 $\alpha$ -2 with small  $r_{\text{in}} = 0.125D_{\text{PSF}}$  (3.15 mas) and strong unresolved scattering polarization. The panel columns give from left to right polarization maps for the  $\text{PSF}_{\text{AO}}$  convolved disk  $X(x, y)$ , system corrected maps  $X^z(x, y)$ , and center corrected maps for the extended polarization region  $X^{\text{ex}}(x, y)$ .

#### 4.4. Partially resolved circumstellar scattering regions

Many circumstellar disks and shells are too small to be fully separated from the star. The  $\text{PSF}_{\text{AO}}$  convolved DiskI60 $\alpha$ -2 model with a small inner cavity  $r_{\text{in}} = 3.15$  mas represents such a situation. The circumstellar scattering in this model produces a substantial amount of unresolved Stokes  $Q_d$  signal in the center (Fig. 21, left panels). The zp-correction for the system (middle panels) sets the integrated  $\Sigma Q^z$  signal to zero and produces therefore a strong  $-Q$  signal in the center and correspondingly strong central quadrant patterns for the  $Q_\phi$  and  $U_\phi$  map with opposite sign when compared to the convolved model. In both cases the strong central  $Q$  signal disturbs substantially the relatively faint signal of the spatially resolved part of the disk, and it is difficult to separate the two polarization components.

##### 4.4.1. ZP-correction for the center.

The polarization offset introduced by the central source can be removed with a star peak or center zp-correction, where the offsets  $\langle q_0 \rangle = \Sigma_0 Q / \Sigma_0 I$  and  $\langle u_0 \rangle = \Sigma_0 U / \Sigma_0 I$  are derived from a few pixels centered on the intensity peak. This sets the polarization signal at the center to zero

$$Q^{z0}(0, 0) = Q(0, 0) - \langle q_0 \rangle I(0, 0) = 0, \quad (38)$$

and equivalent for Stokes  $U^{z0}(0, 0)$  and removes in Fig. 21 the strong central Stokes  $Q$ -component and quadrant patterns in the  $Q_\phi$  and  $U_\phi$  maps. The center correction leaves an extended polar-

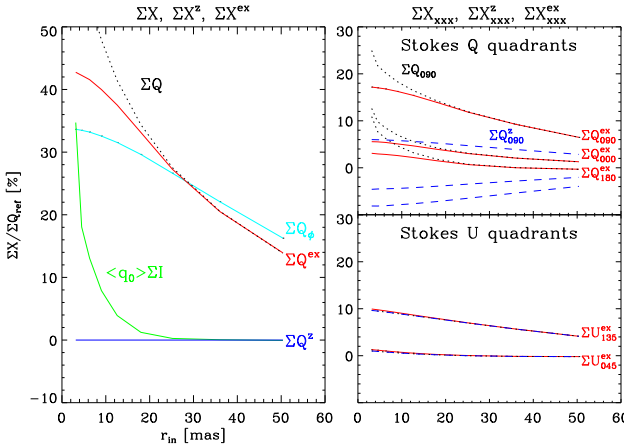


**Fig. 22.** Dependence of the polarization  $\Sigma X / Q_{\phi, \text{ref}}$  and quadrant parameters  $\Sigma X_{\text{XXX}} / Q_{\phi, \text{ref}}$  for DiskI60 $\alpha$ -2 as function of  $r_{\text{in}}$  for the PSF<sub>AO</sub> convolved, system corrected  $X^z$ , and center corrected  $X^{\text{ex}}$  model parameters. All disks have the same outer boundary  $r_{\text{out}} = 100.8$  mas. For Stokes  $Q$  quadrants there is  $\Sigma U_{\text{XXX}} = \Sigma U_{\text{XXX}}^z = \Sigma U_{\text{XXX}}^{\text{ex}}$ .

ization signal from circumstellar scattering called hereafter  $Q^{\text{ex}}$ ,  $U^{\text{ex}}$  according to

$$Q^{z0}(\alpha, \delta) = Q(\alpha, \delta) - \langle q_0 \rangle I(\alpha, \delta) = Q^{\text{ex}}(\alpha, \delta), \quad (39)$$

$$U^{z0}(\alpha, \delta) = U(\alpha, \delta) - \langle u_0 \rangle I(\alpha, \delta) = U^{\text{ex}}(\alpha, \delta). \quad (40)$$

The polarization in the PSF peak  $\langle q_0 \rangle I(0, 0)$  and  $\langle u_0 \rangle I(0, 0)$  can include contributions from the following components: (i) offsets introduced by (residual) interstellar and instrumental polarization  $(q_{\text{is}} + q_{\text{inst}}) I$ ,  $(u_{\text{is}} + u_{\text{inst}}) I$ , and (ii) the intrinsic central polarization  $Q_c = q_s I_s + q_{d,c} I_s$  and  $U_c = u_s I_s + u_{d,c} I_s$  from the star and the unresolved part of the scattering region.

The offset from the center correction is proportional to  $I(\alpha, \delta)$  and corrects therefore exactly the signal introduced by the interstellar and instrumental polarization. In addition also the contribution from the intrinsic stellar polarization  $Q_c$ ,  $U_c$  are corrected, but only approximately because the intensity distribution of the convolved central signal is  $\propto \text{PSF}(\alpha, \delta)$  and differs slightly from  $I(\alpha, \delta)$  used for the correction offset. This introduces a small overcorrection at the level of  $(q_s + q_{d,c}) I^{\text{ext}}(\alpha, \delta) / I_s(\alpha, \delta)$  and similar for Stokes  $U$ , where  $I^{\text{ext}}$  corresponds to the resolved part of the scattering intensity. There is typically  $(q_s + q_{d,c}) I^{\text{ext}}(r) \ll Q_c(r)$  based on similar arguments as discussed in Sect. 3.4, and therefore we can assume that the center correction accounts for many cases well for all contributions to the polarization of the central source.

The center corrected maps  $X^{\text{ex}}(x, y)$  for the DiskI60 $\alpha$ -2 model with small cavity  $r_{\text{in}} = 0.125 D_{\text{PSF}}$  in Fig. 21 look very similar to the non-corrected DiskI60 $\alpha$ -2 model with a larger inner cavity with  $r_0 = 0.5 D_{\text{PSF}}$  plotted in Fig. 14. Thus, the effect of the center zp-correction is very similar to the removal of the polarization signal from the non-resolved inner disk region  $r < 0.5 D_{\text{PSF}}$  (Table E.3).

The zp-correction for the center splits the integrated polarization into a central unresolved component and an extended resolved component

$$\Sigma Q = \Sigma Q_0 + \Sigma Q^{\text{ex}} \quad \text{and} \quad \Sigma U = \Sigma U_0 + \Sigma U^{\text{ex}}. \quad (41)$$

For simulations with a given intrinsic model but using different PSFs for the convolution the total Stokes signals  $\Sigma Q$  and  $\Sigma U$  are conserved but the splitting between the  $\Sigma Q_0$  and  $\Sigma Q^{\text{ex}}$  or the  $\Sigma U_0$  and  $\Sigma U^{\text{ex}}$  components depends on the PSF profile. For a

more extended PSF a larger fraction of the polarization signal will contribute to the unresolved central source and a smaller fraction to the extended (resolved) component.

The impact of the center correction for the  $\Sigma Q$  splitting is illustrated in the left panel of Fig. 22 for DiskI60 $\alpha$ -2 models with different  $r_{\text{in}}$ . For large central cavities  $r_{\text{in}} > D_{\text{PSF}}$  ( $> 25$  mas) there is practically no difference between  $\Sigma Q^{\text{ex}}$  and  $\Sigma Q$  because of the lack of a central component. For small cavity  $r_{\text{in}} < D_{\text{PSF}}$  the unresolved central signal  $\Sigma Q_0 \approx \langle q_0 \rangle \Sigma I$  plotted by the green curve increases strongly for  $r_{\text{in}} \rightarrow 0$ , while the extended polarization  $\Sigma Q^{\text{ex}}$  approaches a limiting value.

Equation 41 for Stokes  $Q$  can also be written as  $\Sigma Q^{\text{ex}} / \Sigma I = \Sigma Q / \Sigma I - \Sigma Q_0 / \Sigma I = \langle q \rangle - \langle q_0 \rangle \Sigma I_0 / \Sigma I$  and the same applies for Stokes  $U$ . In observational data, one can often assume that the central object dominates the total intensity of the system, and use the rough approximation  $\Sigma I_0 / \Sigma I = 1 - \epsilon \approx 1$ . For such cases one can then derive the approximative Stokes flux  $Q^{\text{ex}}$  for the resolved scattering region from the total intensity and the difference between the fractional polarization measured for the whole system and the center according to

$$\Sigma Q^{\text{ex}} \approx (\langle q_{\text{obs}} \rangle - \langle q_0, \text{obs} \rangle) \Sigma I, \quad (42)$$

and equivalent for the  $\Sigma U^{\text{ex}}$ . The two fractional polarization values  $\langle q_{\text{obs}} \rangle$  and  $\langle q_0, \text{obs} \rangle$  depend equally or practically equally on the various polarization offsets listed above. Therefore the differential value is barely affected by polarimetric offset, even if their nature is unclear. This could provide for many cases useful Stokes  $\Sigma Q^{\text{ex}}$  and  $\Sigma U^{\text{ex}}$  parameters for the spatially resolved circumstellar scattering polarization.

The resulting values for the Stokes parameters  $\Sigma Q^{\text{ex}}$  and  $\Sigma U^{\text{ex}}$  describe like  $\Sigma Q_\phi$  properties of the resolved part of the circumstellar scattering and all three parameters depend on the spatial resolution of the observations. Simulations of the convolution can be used to obtain from the ratios of convolved or observed polarization values  $\Sigma Q^{\text{ex}} / \Sigma Q_\phi$  and  $\Sigma U^{\text{ex}} / \Sigma Q_\phi$  stronger constraints on the intrinsic polarization  $Q'(x, y)$ ,  $U'(x, y)$ , and  $Q'_\phi(x, y)$ .

#### 4.4.2. Quadrant parameters for the extended polarization

The maps for the extended polarization  $Q^{\text{ex}}$  and  $U^{\text{ex}}$  are useful for the characterization of the azimuthal polarization  $Q_\phi(\phi)$ . This is illustrated for the DiskI60 $\alpha$ -2 models in the right panels of Fig. 22, which show  $\Sigma X_{\text{XXX}} / Q_{\phi, \text{ref}}$  for the convolved models, and also for the system corrected  $\Sigma X_{\text{XXX}}^z / Q_{\phi, \text{ref}}$ , and center corrected  $\Sigma X_{\text{XXX}}^{\text{ex}} / Q_{\phi, \text{ref}}$  models plotted by black dotted, blue dashed and solid red lines respectively (see also Tab. E.3).

The behaviour of the  $Q$  quadrants is very similar to the integrated Stokes parameter  $\Sigma Q$ , with  $\Sigma Q_{\text{XXX}}^{\text{ex}} = \Sigma Q_{\text{XXX}}$  for  $r_{\text{in}} > D_{\text{PSF}}$ , with a strong increase of  $\Sigma Q_{\text{XXX}}$  for  $r_{\text{in}} < D_{\text{PSF}}$ , and much lower values for the system corrected quadrants  $\Sigma Q_{\text{XXX}}^z$ . The Stokes  $U$  quadrant values are for all three cases the same because they are not affected by Stokes  $Q$  zp-corrections.

The differences between the lines for  $Q$  quadrants with  $xxx = 090, 000$  and  $180$  are the same for the three cases, and this is equivalent to the differential quadrant values (Eq. 35), which practically do not depend on a polarization offset. Thus, the differential quadrant values and the corresponding information on the azimuthal distribution of  $Q_\phi(\phi)$  is preserved by the zp-correction for the central peak.

**Central zero.** A most important advantage of the center corrected maps  $Q^{\text{ex}}(x, y)$  is the central zero (Fig. 21) with facil-

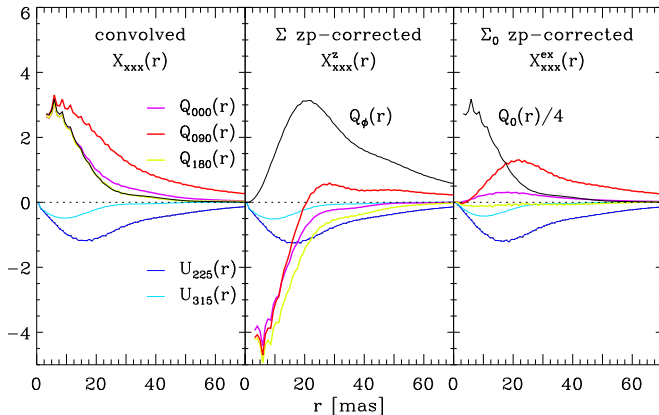


**Fig. 23.** Radial profiles for the polarization signal in the Stokes quadrants for the DiskI60 $\alpha$ -2 model with  $r_{\text{in}} = 0.125 D_{\text{PSF}}$  (3.15 mas). The panels give  $X_{xxx}(r)$  for the convolved,  $X_{xxx}^z(r)$  for the system corrected, and  $X_{xxx}^{ex}(r)$  for the center corrected models. For all three cases the Stokes  $U_{xxx}(r)$  profiles are practically the same.

tates for observational data very significantly the splitting of the  $Q^{\text{ex}}$ -signal into quadrant values. This is illustrated in Fig. 23 with radial profiles for the polarization signal  $X_{xxx}(r)$  obtained by averaging azimuthally the polarization signal within the 90° wedges of the individual quadrants. The profiles show for small  $r$  some sampling noise because of the used finite pixel size of 0.9 mas  $\times$  0.9 mas for the model maps.

The strong central  $Q_c$  signal, which is positive for the convolved map and negative for the map with a system zp-correction, dominates at small  $r$  strongly the  $Q_{xxx}(r)$  and  $Q_{xxx}^z(r)$  profiles. In these cases the determination of quadrant values  $\Sigma Q_{xxx}$  and  $\Sigma Q_{xxx}^z$  depend critically on the splitting of the strong central signal. This can introduce significant uncertainties for AO data with a variable and not exactly axisymmetric PSF core (e.g., Cantalloube et al. 2019). The splitting of the Stokes signal into quadrant values is less critical for the center corrected  $Q^{\text{ex}}$  map with a signal close to zero in the center, where the borderlines between the quadrants intersect. Therefore, the center zp-correction is be very helpful for the derivation of the azimuthal distribution of the Stokes parameters  $Q(\phi)$  and  $U(\phi)$  using quadrant parameters and for the azimuthal parameters  $Q_{\phi}(\phi)$  and  $U_{\phi}(\phi)$  for barely resolved observational data. This is also supported by recent results for observations of the circumstellar dust around post-AGB stars (Andrych et al. 2024, 2025).

## 5. Summary and discussion

High resolution imaging polarimetry is a very attractive differential technique for the detection of a circumstellar scattering regions because the produced polarization signal can be separated from the strong radiation of the central star (e.g., Kuhn et al. 2001; Perrin et al. 2004; Hinkley et al. 2009). However, imaging polarimetry is affected by observational convolution effects and by calibration offsets which must be taken into account for a quantitative analysis (e.g., Schmid et al. 2006; Monnier et al. 2019; Hunziker et al. 2021; Tschudi & Schmid 2021; Ma et al. 2024b). This work investigates these effects systematically and provides guide lines for the derivation of quantitative polarimetric results from observational data. Basic effects are treated with simple model simulations using axisymmetric PSFs, considering only axisymmetric or mirror symmetric scattering geometries aligned with the Stokes  $Q$  polarization direction, and cir-

cular or annular apertures for the determination of zp-correction offsets and integrated flux parameters.

The convolved azimuthal polarization for intrinsically axisymmetric models is also axisymmetric  $Q_{\phi}(r)$  and depends on the PSF profile. The mirror-symmetric models RingI60 and DiskI60 for inclined disks have an azimuthal dependence for  $Q'_{\phi}(\phi)$  and they produce a net Stokes  $\Sigma Q$  signal. The PSF convolution and polarization offsets both change the azimuthal distribution of the signal, which is described by Stokes quadrant polarization parameters  $\Sigma X_{xxx}$ . Because only faint disks are considered  $\Sigma I_d \lesssim 0.05 \Sigma I_s$  a polarimetric offset for Stokes  $Q$  is close to axisymmetric  $q I(x, y) \approx q I(r)$  and this changes the four quadrants  $\Sigma Q_{xxx}$  practically equally, while the Stokes  $U$  signal is not changed by a Stokes  $Q$  offset. Observational data are more complex than the presented simple simulations and instrumental effects introduce additional noise, but many basic results of this study are still applicable or approximately valid for the interpretation of real data.

**Presence of circumstellar polarization.** In all models a net positive azimuthal polarization  $\Sigma Q_{\phi} > 0$  indicates the presence of resolved circumstellar scattering polarization. Measurements of  $\Sigma Q_{\phi}$  are ideal for the detection of faint, extended circumstellar scattering regions, because the signal is not biased by pixel to pixel noise and can be summed up for large image areas (Schmid et al. 2006). For observational data one needs to define  $\Sigma Q_{\phi}$  detection limits considering spurious signals from PSF variations or systematic instrumental noise (e.g., Cantalloube et al. 2019; Tschudi et al. 2024). According to the presented noise free simulations a measurable  $\Sigma Q_{\phi}$ -signal can be obtained for very compact scattering regions down to a separation of about  $r \approx D_{\text{PSF}}$  and this has also been achieved for observational data (e.g., Avenhaus et al. 2017; Schmid et al. 2018; Andrych et al. 2025) In addition the  $\Sigma Q_{\phi}$  value is not significantly changed by a polarization offset  $p I(r)$  because this adds for  $Q_{\phi}(x, y)$  only a positive-negative quadrant pattern with practically no net  $\Sigma Q_{\phi}$  signal.

**Degradation of the  $Q_{\phi}$  signal.** The PSF convolution degrades the  $\Sigma Q_{\phi}$  signal because of the smearing and polarimetric cancellation (Schmid et al. 2006). The effect is particularly strong for small separations from the star and there results practically no net  $\Sigma Q_{\phi}$  signal for a scattering regions with separation  $r \lesssim 0.5 D_{\text{PSF}}$  from the star. For resolved but compact scattering regions  $0.5 D_{\text{PSF}} < r < 5 D_{\text{PSF}}$  the degradation depends strongly on the PSF structure and is about a factor of a few for the PSF<sub>AO</sub> used in the simulations. For scattering regions at larger separation  $r \gtrsim 10 D_{\text{PSF}}$  the  $\Sigma Q_{\phi}$  degradation is at a level of about  $\approx 10\% - 30\%$  according to Table 1 and the tables in the appendix. For AO observations with high PSF Strehl ratio of about  $S \approx 0.8$  or a space instrument with  $S \approx 1$ , the degradation would be closer or comparable to the model results using the Gaussian PSF<sub>G</sub>.

A measurement of the azimuthal polarization  $\Sigma Q_{\phi}/\Sigma I$  should always include an assessment of the convolution effects based on the observational PSF and provide an estimate or even a derivation of the intrinsic circumstellar polarization  $\Sigma Q'_{\phi}/\Sigma I'$ . This allows for individual objects comparisons between results from different observations and enables investigations about temporal variations and the wavelength dependence of the polarized reflectivity (e.g., Ma et al. 2024a,b; Andrych et al. 2025).

The PSF<sub>AO</sub> convolution of inclined disks introduces a cross-talk signal  $Q_\phi \rightarrow U_\phi$ , significant differences between the azimuthal polarization  $Q_\phi$  and the polarized flux  $P$ , extended Stokes  $Q$ ,  $U$  polarization halos, and central Stokes signals  $Q$ ,  $U$  for unresolved inner scattering regions. These extended and central Stokes components produce in the azimuthal polarization maps  $Q_\phi(x, y)$  and  $U_\phi(x, y)$  quadrant patterns with practically zero net  $Q_\phi$ ,  $U_\phi$  signal, if measured in axisymmetric apertures as illustrated in Figs. 9 and 11.

**Stokes polarization parameters.** The integrated Stokes parameters  $\Sigma Q$  and  $\Sigma U$  do not depend on the PSF convolution but the smearing leads to a mutual averaging of the polarization between the positive and negative Stokes  $\Sigma Q_{xxx}$  or  $\Sigma U_{xxx}$  quadrants towards the mean value  $\Sigma Q/4$  or  $\Sigma U/4$ , respectively. This changes also the azimuthal distribution  $Q_\phi(\phi)$  of the circumstellar polarization in step with the degradation of the integrated  $\Sigma Q_\phi$  signal. Differential quadrant values expressed relative to  $\Sigma Q_\phi$ , like  $(\Sigma Q_{xxx} - \Sigma Q/4)/\Sigma Q_\phi$ , are much less changed by the PSF convolution, and therefore they provide for convolved data still strong constraints on the intrinsic azimuthal distribution of  $Q'_\phi(\phi)$ . For complex scattering geometries it is more difficult to account for the mutual averaging effect between the polarization quadrants, but the basic principle is still valid and can be considered for the interpretation of the data.

An unresolved central scattering region can produce a central signal  $\Sigma Q_c$ ,  $\Sigma U_c$  with a spatial distribution like the PSF. This can be compared with the spatially resolved polarization  $Q(x, y)$  and  $U(x, y)$  at  $r \gtrsim D_{\text{PSF}}$  providing potentially strong constraints on the presence and the radius of a central cavity caused by dust sublimation for accretion disks or dust condensation for shells around mass losing stars.

**Polarization offsets and zp-correction.** Measurements of Stokes parameters  $\Sigma Q$ ,  $\Sigma U$  and quadrant values  $\Sigma Q_{xxx}$ ,  $\Sigma U_{xxx}$  are often affected by residual polarimetric offsets  $p_{\text{res}} I(x, y)$  introduced by not so well known amounts of intrinsic stellar polarization, or by interstellar and instrumental polarization. Already, an offset of  $p_{\text{res}} \gtrsim 0.001$  can introduce strong bias effects or even mask the circumstellar polarization signal.

A polarimetric zero point or zp-correction accounts for a fractional Stokes polarization offset  $\langle q \rangle I(x, y)$  and  $\langle u \rangle I(x, y)$ , and this is for many observations a key step to reveal better the circumstellar polarization signal.

A correction offset  $-\langle q \rangle I(x, y)$  has for all four Stokes  $Q$  quadrants the same impact with practically no change for the differential quadrant values  $\Sigma_2 Q_{xxx} - \Sigma_2 Q/4$ . The same would apply for Stokes  $U$  offset, and the corrected Stokes values  $\Sigma Q^z$ ,  $\Sigma U^z$  and quadrant  $\Sigma Q_{xxx}^z$ ,  $\Sigma U_{xxx}^z$  can be recalibrated, if accurate determination of the intrinsic  $\Sigma Q'$  and  $\Sigma U'$  are available.

A zp-correction does not change significantly the integrated azimuthal polarization  $\Sigma Q_\phi$ , but it introduces a bias effect for the azimuthal signal distribution  $Q_\phi(\phi) \neq Q'_\phi(\phi)$ . A negative offset  $-\langle q \rangle I(x, y)$  reduces for the RingI60 and DiskI60 models the positive  $Q_{090}$  and  $Q_{270}$  quadrants and makes the negative quadrants  $Q_{000}$  and  $Q_{180}$  even more negative. For  $Q_\phi(\phi)$ , this is equivalent to a weakening around  $\phi \approx 90^\circ$  and  $\approx 270^\circ$ , while the signals around  $\phi \approx 0^\circ$  and  $\approx 180^\circ$  are enhanced. The zp-corrected RingI60 model shows for the quadrant ratio  $\Sigma Q_{180}^z/\Sigma Q_{090}^z$  a value which is more than 50 % enhance when compared to the model without zp-correction (Fig. 19, Table E.1), equivalent to a much enhanced front side brightness. This effect must be taken into

account for the derivation of the polarized scattering phase functions for the dust in the disk.

A positive Stokes  $U$  offset would enhance the  $U_{135}$  and  $U_{315}$  components and make the negative quadrants  $U_{045}$  and  $U_{225}$  even more negative as shown in Fig. 16 and in principle similar to the case of Stokes  $Q$ . However, because the  $U$  direction is not aligned with the symmetry of the adopted model geometries an  $U$  offset distorts the antisymmetric or symmetric appearance of the  $U$ ,  $U_\phi$  and  $Q_\phi$  maps.

Important for the zp-correction are well defined correction region  $\Sigma_{\text{zp}}$  and different useful cases are illustrated in the sketch in Fig. 24. The reference case is a circumstellar signal without intrinsic stellar polarization and observational polarization offset. A system normalization  $\Sigma_{\text{zp}} = \Sigma$  sets the net polarization to zero  $\Sigma Q^z = 0$ , and introduces for the RingI60 model a negative polarization for the which compensates the circumstellar signal  $\Sigma_1 Q^z = -\Sigma_2 Q^z$ .

Practically the same  $Q^z$  maps are obtained for the same circumstellar model, but “affected” by an offset from interstellar, instrumental or intrinsic stellar polarization. Therefore, the zp-correction is very useful to mitigate offsets and calibration uncertainties, because one can search for an intrinsic  $Q'(x, y)$ ,  $U'(x, y)$  model, which matches after convolution and a zp-correction the observed and zp-corrected data despite some undefined offsets.

If other data provide accurate values  $(\Sigma Q', \Sigma U') = (\Sigma Q, \Sigma U)$ , then one can correct the zp-corrected data and derive  $Q(x, y)$ ,  $U(x, y)$  maps without offsets. Alternatively, if the central star can be used as zero polarization standard, then a zp-correction based on the star  $\Sigma_{\text{zp}} = \Sigma_1$  provides directly the intrinsic Stokes signal  $\Sigma Q'_d = \Sigma Q^{z1}$  and  $\Sigma U'_d = \Sigma U^{z1}$ .

A good solution for coronagraphic observations or data with saturated star is the use of the halo region  $\Sigma_{\text{zp}} = \Sigma_3$  for the zp-correction, because the fractional polarization of the smeared signal in the halo approximates well the value for the whole system  $\langle q_3 \rangle \approx \langle q \rangle$ . This correction provides then a good match for the reference case  $Q^{z3}(x, y) \approx Q^z(x, y)$  outside of the coronagraphic mask (Fig. 24). This procedure requires enough signal and the absence of significant systematic errors in the halo for the determination of  $\langle q_3 \rangle$ , what may be critical for some observations. In addition, one needs also a separate PSF calibration to estimate the smearing degradation of the derived  $Q_\phi$  signal.

For partially resolved scattering regions a zp-correction based on a few brightest pixels of the PSF peak  $\Sigma_{\text{zp}} = \Sigma_0$  can be very favourable. This approach splits the signal into two components: (i) an unresolved polarization for the central source  $Q_0$ ,  $U_0$  with a spatial distribution like the PSF and zero azimuthal polarization  $\Sigma Q_{\phi,0} \approx 0$  and (ii) an extended polarization maps  $Q^{\text{ex}}(x, y)$ ,  $U^{\text{ex}}(x, y)$  and  $Q_\phi$  with a central zero, and quadrant values  $\Sigma Q_{xxx}^{\text{ex}}$ ,  $\Sigma U_{xxx}^{\text{ex}}$  constraining the azimuthal distribution of  $Q_\phi(\phi)$  down to a separation of  $r \approx D_{\text{PSF}}$ . The center correction accounts for offsets introduced by interstellar and instrumental polarization, and for the contributions from the intrinsic polarization of the unresolved, central source. The resulting maps represent the resolved part of the circumstellar polarization signal  $Q^{\text{ex}}(x, y) \approx Q_d(x, y)$  and  $U^{\text{ex}}(x, y) \approx U_d(x, y)$ .

**Conclusions.** The presented model simulations explore systematically the PSF convolution effects and the impact of polarization offsets for imaging polarimetry of circumstellar scattering regions. The used simple models are ideal for a description of the basic principles which also apply for more complex systems and should be considered for the planning of new observations and for the interpretation and analysis of observational

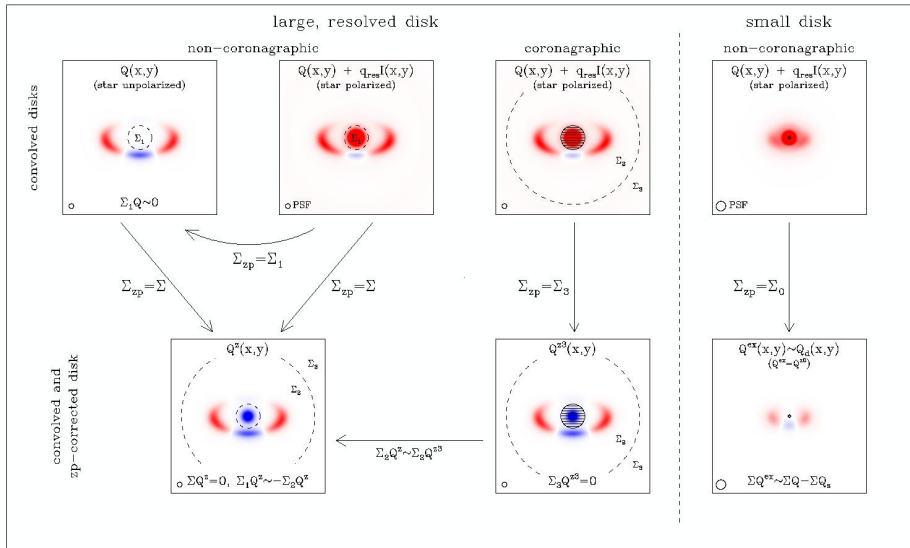


**Fig. 24.** Sketch for the polarimetric zp-corrections procedures for Stokes  $Q$ . The system correction  $\Sigma_{zp} = \Sigma$  gives the same  $Q^z$  for the first two cases, while a star correction  $\Sigma_{zp} = \Sigma_1$  can recover the convolved  $Q^{z1} = Q$  case for data with a polarization offset. A halo correction  $\Sigma_{zp} = \Sigma_3$  is a good approach for coronagraphic data ( $Q^{z3} \approx Q^z$  outside of the coronagraphic disk). A center correction  $\Sigma_{zp} = \Sigma_0$  provides the resolved circumstellar signal  $Q^{ex}$  for compact regions.

data. Important is, that observational data are taken which can be corrected for the instrumental PSF convolution using PSF calibrations, and that polarimetric offsets are corrected with a well defined zp-correction procedure. In particular, for coronagraphic high contrast observations a good PSF calibration and polarimetric measurements for the central bright object with non-coronagraphic exposures could provide higher quality results.

Future instruments may target more demanding objects and effects introduced by non-axisymmetric features in the PSF convolution and field dependent polarimetric offsets could affect significantly the data. Analysis procedures considering only axisymmetric PSFs and simple fractional polarization offset may not be sufficient. However, an important first step are investigations of the achievable limits using the procedures discussed in this work for available data, which have barely been started despite the existence of many high quality observations in data archives (e.g., Benisty et al. 2023). This will provide useful insights on the next level of challenges to be considered for future improvements in polarimetric imaging.

*Acknowledgements.* We thank the referee, Frans Snik, for very thoughtful and supportive comments, which improved the manuscript. JM thanks the Swiss National Science Foundation for financial support under grant number P500PT\_222298.

## References

Andrych, K., Kamath, D., Kluska, J., et al. 2023, MNRAS, 524, 4168  
 Andrych, K., Kamath, D., Van Winckel, H., et al. 2025, PASA, 42, e125  
 Andrych, K., Kamath, D., Van Winckel, H., et al. 2024, MNRAS, 535, 1763  
 Angel, J. R. P. & Martin, P. G. 1973, ApJ, 180, L39  
 Arriaga, P., Fitzgerald, M. P., Duchêne, G., et al. 2020, AJ, 160, 79  
 Avenhaus, H., Quanz, S. P., Garufi, A., et al. 2018, ApJ, 863, 44  
 Avenhaus, H., Quanz, S. P., Schmid, H. M., et al. 2017, AJ, 154, 33  
 Avenhaus, H., Quanz, S. P., Schmid, H. M., et al. 2014, ApJ, 781, 87  
 Bastien, P., Robert, C., & Nadeau, R. 1989, ApJ, 339, 1089  
 Benisty, M., Dominik, C., Follette, K., et al. 2023, in Astronomical Society of the Pacific Conference Series, Vol. 534, Protostars and Planets VII, ed. S. Inutsuka, Y. Ikawa, T. Muto, K. Tomida, & M. Tamura, 605  
 Beuzit, J. L., Vigan, A., Mouillet, D., et al. 2019, A&A, 631, A155  
 Birnstiel, T. 2024, ARA&A, 62, 157  
 Canovas, H., Ménard, F., de Boer, J., et al. 2015, A&A, 582, L7  
 Cantalloube, F., Dohlen, K., Milli, J., Brandner, W., & Vigan, A. 2019, The Messenger, 176, 25  
 Chen, C. H., Mittal, T., Kuchner, M., et al. 2014, ApJS, 211, 25  
 Crotts, K. A., Matthews, B. C., Duchêne, G., et al. 2024, ApJ, 961, 245  
 de Boer, J., Langlois, M., van Holstein, R. G., et al. 2020, A&A, 633, A63

Draine, B. T. 2003, ARA&A, 41, 241  
 Engler, N., Schmid, H. M., Thalmann, C., et al. 2017, A&A, 607, A90  
 Esposito, T. M., Kalas, P., Fitzgerald, M. P., et al. 2020, AJ, 160, 24  
 Ferrarotti, A. S. & Gail, H. P. 2006, A&A, 447, 553  
 Fétick, R. J. L., Fusco, T., Neichel, B., et al. 2019, A&A, 628, A99  
 Garufi, A., Avenhaus, H., Pérez, S., et al. 2020, A&A, 633, A82  
 Garufi, A., Dominik, C., Ginski, C., et al. 2022, A&A, 658, A137  
 Gáspár, A., Wolff, S. G., Rieke, G. H., et al. 2023, Nature Astronomy, 7, 790  
 Ginski, C., Tazaki, R., Dominik, C., & Stolker, T. 2023, ApJ, 953, 92  
 Graham, J. R., Kalas, P. G., & Matthews, B. C. 2007, ApJ, 654, 595  
 Heikamp, S. & Keller, C. Ü. 2019, A&A, 627, A156  
 Hinkley, S., Oppenheimer, B. R., Soummer, R., et al. 2009, ApJ, 701, 804  
 Hodapp, K. W., Suzuki, R., Tamura, M., et al. 2008, in Society of Photo-Optical Instrumentation Engineers (SPIE) Conference Series, Vol. 7014, Ground-based and Airborne Instrumentation for Astronomy II, ed. I. S. McLean & M. M. Casali, 701419  
 Höfner, S. & Olofsson, H. 2018, A&A Rev., 26, 1  
 Hughes, A. M., Duchêne, G., & Matthews, B. C. 2018, ARA&A, 56, 541  
 Hunziker, S., Schmid, H. M., Ma, J., et al. 2021, A&A, 648, A110  
 Hunziker, S., Schmid, H. M., Mouillet, D., et al. 2020, A&A, 634, A69  
 Kalas, P., Graham, J. R., Fitzgerald, M. P., & Clampin, M. 2013, ApJ, 775, 56  
 Khouri, T., Vlemmings, W. H. T., Paladini, C., et al. 2020, A&A, 635, A200  
 Kuhn, J. R., Potter, D., & Parise, B. 2001, ApJ, 553, L189  
 Kwon, J., Tamura, M., Hough, J. H., et al. 2014, ApJ, 795, L16  
 Lawson, K., Schlieder, J. E., Leisenring, J. M., et al. 2023, AJ, 166, 150  
 Lenzen, R., Hartung, M., Brandner, W., et al. 2003, in Society of Photo-Optical Instrumentation Engineers (SPIE) Conference Series, Vol. 4841, Instrument Design and Performance for Optical/Infrared Ground-based Telescopes, ed. M. Iye & A. F. M. Moorwood, 944–952  
 Lucas, M., Norris, B., Guyon, O., et al. 2024, PASP, 136, 114504  
 Ma, J., Ginski, C., Tazaki, R., et al. 2024a, A&A, 691, L16  
 Ma, J. & Schmid, H. M. 2022, A&A, 663, A110  
 Ma, J., Schmid, H. M., & Stolker, T. 2024b, A&A, 683, A18  
 Ma, J., Schmid, H. M., & Tschudi, C. 2023, A&A, 676, A6  
 Milli, J., Engler, N., Schmid, H. M., et al. 2019, A&A, 626, A54  
 Milli, J., Vigan, A., Mouillet, D., et al. 2017, A&A, 599, A108  
 Monnier, J. D., Harries, T. J., Bae, J., et al. 2019, ApJ, 872, 122  
 Montargès, M., Cannon, E., de Koter, A., et al. 2023, A&A, 671, A96  
 Murakawa, K., Suto, H., Tamura, M., et al. 2004, PASJ, 56, 509  
 Ohnaka, K., Weigelt, G., & Hofmann, K. H. 2016, A&A, 589, A91  
 Perrin, M. D., Duchêne, G., Millar-Blanchaer, M., et al. 2015, ApJ, 799, 182  
 Perrin, M. D., Graham, J. R., Kalas, P., et al. 2004, Science, 303, 1345  
 Perrin, M. D., Sivaramakrishnan, A., Makidon, R. B., Oppenheimer, B. R., & Graham, J. R. 2003, ApJ, 596, 702  
 Pinilla, P., Benisty, M., de Boer, J., et al. 2018, ApJ, 868, 85  
 Poteet, C. A., Chen, C. H., Hines, D. C., et al. 2018, ApJ, 860, 115  
 Quanz, S. P., Avenhaus, H., Buenzli, E., et al. 2013, ApJ, 766, L2  
 Quanz, S. P., Schmid, H. M., Geissler, K., et al. 2011, ApJ, 738, 23  
 Rapson, V. A., Kastner, J. H., Millar-Blanchaer, M. A., & Dong, R. 2015, ApJ, 815, L26  
 Ren, B. B., Benisty, M., Ginski, C., et al. 2023, A&A, 680, A114  
 Schmid, H. M. 2021, A&A, 655, A83  
 Schmid, H. M. 2022, arXiv e-prints, arXiv:2207.14511  
 Schmid, H. M., Bazzon, A., Roelfsema, R., et al. 2018, A&A, 619, A9  
 Schmid, H. M., Joos, F., & Tschud, D. 2006, A&A, 452, 657  
 Schneider, G., Grady, C. A., Hines, D. C., et al. 2014, AJ, 148, 59  
 Simmons, J. F. L. & Stewart, B. G. 1985, A&A, 142, 100  
 Stolker, T., Dominik, C., Avenhaus, H., et al. 2016, A&A, 595, A113  
 Tinbergen, J. 2007, PASP, 119, 1371  
 Tschudi, C. & Schmid, H. M. 2021, A&A, 655, A37  
 Tschudi, C., Schmid, H. M., Nowak, M., et al. 2024, A&A, 687, A74  
 van Boekel, R., Henning, T., Menu, J., et al. 2017, ApJ, 837, 132  
 van Holstein, R. G., Girard, J. H., de Boer, J., et al. 2020, A&A, 633, A64  
 Woitke, P., Kamp, I., Antonellini, S., et al. 2019, PASP, 131, 064301  
 Zhou, Y., Bowler, B. P., Yang, H., et al. 2023, AJ, 166, 220

## Appendix A: Polarization parameters

Stokes polarization parameters  $Q$ ,  $U$  and azimuthal polarization parameters  $Q_\phi$ ,  $U_\phi$  are used in this work for the description of the model results. Convolution and polarization offset are simple mathematical operations for the Stokes parameters, but quite complex for the azimuthal parameters. Therefore, a comprehensive quantitative description of the circumstellar scattering polarization requires an extensive framework of parameters, which is outlined in Table A.1 for the convolved models and in Table A.2 for zp-corrected models in the system aligned  $x, y$ -coordinates.

A few remarks on the entries in the tables. The integration regions  $\Sigma_{\text{int}}$  and the zp-calibration regions  $\Sigma_{\text{zp}}$  are defined on a model by model basis, with the aim to quantify the polarization signal for the whole system  $\Sigma$ , or only the central source  $\Sigma_1$ , the disk  $\Sigma_2$ , and the halo  $\Sigma_3$ , and combination of these subregions like  $\Sigma_{1+2}$ .

It is also important to distinguish between  $\Sigma P$  and  $\mathcal{P}(\Sigma)$ .  $\Sigma P$  is the sum of the degree of linear polarization measured for each pixel in the resolved map in the integration region  $\Sigma$  (Eq. 10). This does not consider the position angle  $\theta$  of the polarization. In addition, the polarization  $\Sigma P$  depends in a complex way on the spatial resolution, on instrumental noise, and on polarization offsets.

Therefore it is useful to characterize the “aperture” polarization  $\mathcal{P}(\Sigma_i)$  for a given integration region  $\Sigma_i$  using the sums of the Stokes parameters according to

$$\mathcal{P}(\Sigma_i) = ((\Sigma_i Q)^2 + (\Sigma_i U)^2)^{1/2} \quad (\text{A.1})$$

with the corresponding position angle

$$\theta(\Sigma_i) = 0.5 \text{ atan2}(\Sigma_i U, \Sigma_i Q). \quad (\text{A.2})$$

The fractional polarization can then be defined by  $p_i = \mathcal{P}(\Sigma_i)/\Sigma_i I$  or for the Stokes components by  $q_i = \Sigma_i Q/\Sigma_i I$  and  $u_i = \Sigma_i U/\Sigma_i I$ , from which one can also derive a position angle  $\theta_i$ . The polarization of the star, or all the fractional polarization parameters like  $q_{is}$ ,  $\langle q_i \rangle$ , or  $q_0$ , are defined with these “aperture” polarization parameters.

## Appendix B: Faint PSF<sub>AO</sub> artifacts

The extended halo of the PSF<sub>AO</sub>, in particular the strong speckle ring at a separation of about  $0.45''$ , can introduce weak artefacts in the convolved polarization maps. For an axisymmetric, compact system with  $r_0 < 100$  mas the positive-negative Stokes  $Q$  and  $U$  quadrant patterns are not resolved by the PSF halo and therefore there is no net  $\Sigma Q$  and  $\Sigma U$  signal which can produce a polarized halo ghost signal. However, for more extended scattering regions the quadrant patterns are also resolved by the PSF halo and this can produce various kinds of weak spurious features.

One example is illustrated in Fig. B.1 for the Ring0 model with  $r_0 = 201.6$  mas convolved with PSF<sub>AO</sub>, but also with PSF<sub>1</sub> representing the full 2D speckle structure of a single frame from SPHERE/ZIMPOL (see Schmid et al. 2018, for PSF details). If multiple polarimetric measurements are taken in field rotation mode and then combined in a derotated data set, then the patterns in PSF<sub>1</sub> will average towards the case PSF<sub>AO</sub>. The panels in Fig. B.1 emphasize the weak outer structure in the convolved  $Q_\phi(x, y)$  and  $Q(x, y)$ ,  $U(x, y)$  maps using a strongly saturated color scale. The insets on the lower right show the central ring signals with a  $200 \times$  wider color scale.

**Table A.1.** Polarization parameters for convolved and intrinsic models.

param.	description
parameters for the convolved maps	
$I(x, y)$	intensity
$Q(x, y)$	linear Stokes polarization $Q = I_0 - I_{90}$
$U(x, y)$	linear Stokes polarization $U = I_{45} - I_{135}$
$Q_\phi(x, y)$	azimuthal parameters for the linear polarization
$U_\phi(x, y)$	with respect to $x_0, y_0$ (Eqs. 8,9).
$P(x, y)$	intensity of the polarized flux (Eq. 10)
$X(x, y)$	expression for different parameter maps, e.g., $X = \{I, Q, U, P, Q_\phi, U_\phi\}$
$\Sigma_{\text{int}} X$	summed parameter in integration region $\Sigma_{\text{int}}$
used centro-symmetric apertures $\Sigma_{\text{int}}^a$	
$\Sigma$	round aperture for whole system
$\Sigma_1$	small, round aperture centered on the star
$\Sigma_2$	annular aperture including the disk
$\Sigma_3$	annular aperture for the halo
$\Sigma_i$	expression for all apertures $\Sigma_i = \{\Sigma, \Sigma_1, \Sigma_2, \Sigma_3\}^b$
quadrant polarization parameters <sup>c</sup>	
$\Sigma_i Q_{xxx}$	Stokes $Q$ quadrants $\Sigma_i Q_{000}, \Sigma_i Q_{090}, \Sigma_i Q_{180}, \Sigma_i Q_{000}^d$
$\Sigma_i U_{xxx}$	Stokes $U$ quadrants $\Sigma_i U_{045}, \Sigma_i U_{135}, \Sigma_i U_{225}, \Sigma_i U_{315}$
$\Sigma_i X_{xxx}$	expression for all quadrant parameters
$\Sigma_i X_{xxx _\phi}$	azimuthal quadrant parameters considering sign for positive $Q_\phi$ contribution (Sect. 4.3.2)
$\Delta Q_{xxx}$	differential quadrant value for Stokes $Q$ (Eq. 15)
$\Delta U_{\pm}$	differential quadrant values for Stokes $U$ (Eq. 17)
azimuthal polarization in radial and azimuthal coordinates	
$Q_\phi(r, \phi)$	used in the discussion for the $Q_\phi$ distribution in radial apertures $\Sigma_i Q_\phi$ and the angular distribution in quadrants $\Sigma_i X_{xxx _\phi}$
components of intrinsic models	
$I'_s, I'_d$	stellar and circumstellar (dust or disk) intensity
$I'$	total intensity $I'(x, y) = I'_d(x, y) + I'_s(x_0, y_0)$
$Q'_s, Q'_d$	same for Stokes $Q'$ (Eq. 3)
$U'_s, U'_d$	same for Stokes $U'$ (Eq. 4)
$Q'_\phi$	circumstellar azimuthal polarization $Q'_\phi = Q'_{\phi,d}$
$U'_\phi$	$U'_\phi = 0$ in the adopted models
$\mathcal{P}'_d(\Sigma)$	aperture polarization and position angle for disk (Eqs. A.1 and A.2)
$\theta'_d(\Sigma)$	
$\mathcal{P}'_s, \theta'_s$	same for point like star ( $\mathcal{P}'_s = P'_s(x_0, y_0)$ )

**Notes.** The polarization parameters are aligned with the  $x, y$ -coordinates of the scattering models. <sup>(a)</sup> see Fig. 21; <sup>(b)</sup> there is  $\Sigma = \Sigma_1 + \Sigma_2 + \Sigma_3$ ;

<sup>(c)</sup> see Figs. 9, 21; <sup>(d)</sup> there is  $\Sigma_i Q = \Sigma_i Q_{000} + \Sigma_i Q_{090} + \Sigma_i Q_{180} + \Sigma_i Q_{000}$ .

The PSF<sub>AO</sub> speckle ring, indicated in Fig. B.1 for the PSFs by a dashed circle, produces in the Stokes maps for the positive or negative Stokes quadrants of the circumstellar polarization ring, a corresponding circular positive and negative ghost on top of the disk signal. This is indicated in the  $U(x, y)$  maps with four dashed circles centered on the  $U$  ring quadrants. These ghosts add up to a weak positive/negative tile pattern for the convolution with PSF<sub>1</sub> with its quadratic substructure, while the pattern is much smoother for the PSF<sub>AO</sub> convolved  $U$  maps. The same ghosts, but rotated by  $45^\circ$ , are present in the Stokes  $Q$  maps. Therefore, there results for the convolved  $Q_\phi(x, y)$  map a weak, negative ring (a radial polarization signal!) just outside the disk ring, and a weak positive ring further out. This is a special case

**Table A.2.** Polarization parameter for the zp-corrected models.

param.	description
$\Sigma_{\text{zp}}$	zero-point correction region $\Sigma_{\text{zp}} = \Sigma_i$
fractional polarization correction factor	
$\langle q_i \rangle$	equal to $\Sigma_i Q / \Sigma_i I$
$\langle u_i \rangle$	equal to $\Sigma_i U / \Sigma_i I$
fractional Stokes polarization offsets	
$q_{\text{is}}, u_{\text{is}}$	for interstellar polarization (Eqs. 6 and 7)
$q_{\text{inst}}, u_{\text{inst}}$	for instrumental polarization
$q_s, u_s$	for intrinsic stellar polarization
$q_{d,c}, u_{d,c}$	for intrinsic, unresolved circumstellar polarization
zp-corrected maps	
$Q^{\text{zi}}(x, y)$	zp-corrected Stokes $Q$ map for $\Sigma_{\text{zp}} = \Sigma_i$
$U^{\text{zi}}(x, y)$	same for zp-corrected Stokes $U$ map
$Q_{\phi}^{\text{zi}}(x, y)$	$\Sigma_i$ zp-corrected azimuthal polarization maps
$U_{\phi}^{\text{zi}}(x, y)$	derived from $Q^{\text{zi}}(x, y)$ and $U^{\text{zi}}(x, y)$ <sup>a</sup>
integrated zp-corrected parameters	
$\Sigma_i X^{\text{zi}}$	$\Sigma_{\text{zp}} = \Sigma_i$ corrected $X$ -parameter integrated in $\Sigma_i$
$\Sigma_i X_{xxx}^{\text{zi}}$	same for quadrant parameters
special quantities for center zp-correction	
$\Sigma_0$	aperture for central pixels of the stellar PSF peak
$q_0, u_0$	fractional polarization for central pixels
$Q_0(x, y)$	Stokes flux $q_0 \Sigma I(x, y)$ and
$U_0(x, y)$	Stokes flux $u_0 \Sigma I(x, y)$
$Q^{\text{ex}}(x, y)$	Stokes $Q$ and $U$ maps for center corrected, spatially
$U^{\text{ex}}(x, y)$	resolved polarization <sup>b</sup>
$Q_{\phi}^{\text{ex}}(x, y)$	azimuthal polarization maps for center corrected,
$U_{\phi}^{\text{ex}}(x, y)$	spatially resolved polarization
integrated zp-corrected parameters	
$\Sigma Q^{\text{ex}}$	integrated Stokes polarization for center corrected,
$\Sigma U^{\text{ex}}$	resolved polarization signal
$\Sigma X_{xxx}^{\text{ex}}$	corresponding quadrant polarization values
$\Sigma Q_{\phi}^{\text{ex}}$	integrated azimuthal polarization for center
$\Sigma U_{\phi}^{\text{ex}}$	corrected, resolved polarization signal
$\Sigma Q, \Sigma U$	total signal $\Sigma Q = \Sigma Q_0 + \Sigma Q^{\text{ex}}$ and $\Sigma U = \Sigma U_0 + \Sigma U^{\text{ex}}$

**Notes.** The polarization parameters are aligned with the  $x, y$ -coordinates of the scattering models. <sup>(a)</sup> see Table E.1 for all possible combinations; <sup>(b)</sup>  $Q^{\text{ex}}$  and  $U^{\text{ex}}$  are equal to  $Q^0$  and  $U^0$ .

because the polarization is concentrated in a narrow ring with a radius of about half the size of the  $\text{PSF}_{\text{AO}}$  speckle ring. The SB of the spurious negative  $Q_{\phi}$ -signal at  $r \approx 460$  mas is at the level of  $-0.2\%$  of the positive  $Q_{\phi}$  SB peak signal of the disk ring. The negative  $Q_{\phi}$  signal introduces also a small discrepancy between the integrated  $\Sigma Q_{\phi}$  and  $\Sigma P$  values despite the strict axisymmetry.

Another type of circular ghost pattern appears for the large Ring0 model with  $r_0 \approx 800$  mas, where the  $\text{PSF}_{\text{AO}}$  convolution produces two weak, positive  $Q_{\phi}$  ghost rings, one just outside and one just inside of the bright disk ring. These features are also very faint and can often be neglected in typical polarimetric data taken with current AO systems. However, one should be careful with the interpretation of faint structures near bright scattering regions. The protoplanetary disk around HD 169142 is a case with a narrow bright ring, where this type of ghost had to be taken into account in the measurements of Tschudi & Schmid

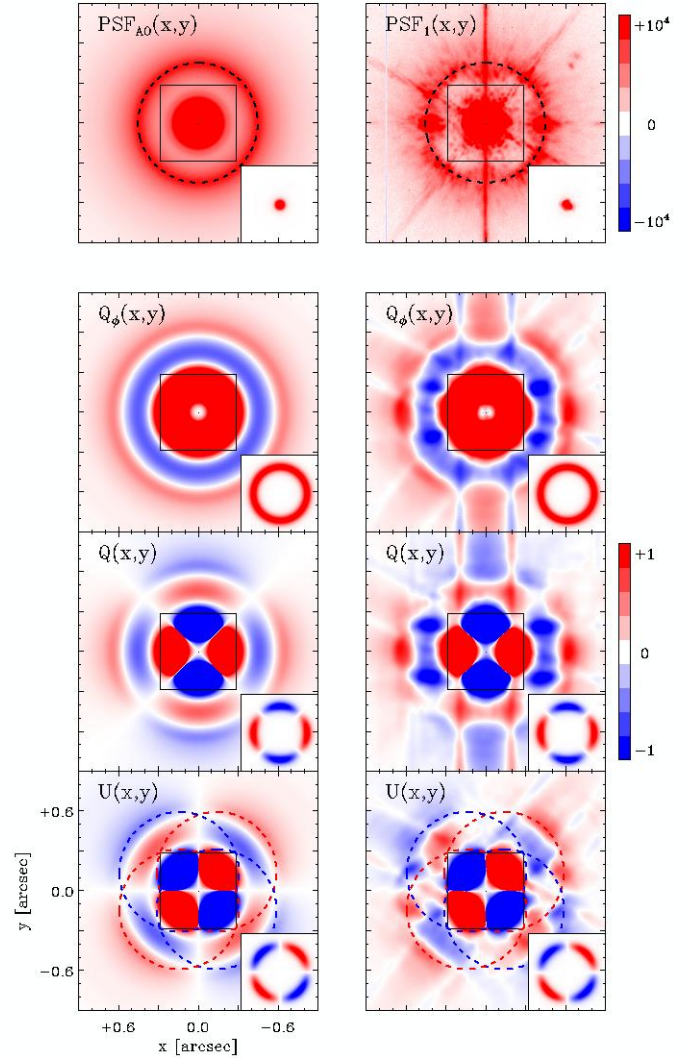


**Fig. B.1.** Faint polarization artifacts in the maps  $Q_{\phi}(x, y)$ ,  $Q(x, y)$ ,  $U(x, y)$ ,  $U_{\phi}(x, y)$  of the Ring0 model  $r_0 = 201.6$  mas produced by the axisymmetric  $\text{PSF}_{\text{AO}}(x, y)$  (left column), and a 2D single frame speckle  $\text{PSF}_1$  of an AO system (right column). Dashed circles are indicated for the PSFs and the Stokes  $U$  maps to indicate the location of the halos produced by the speckle ring. The color scale is strongly saturated in the centre of the main maps and therefore this region is plotted as inset on the lower right with a  $200 \times$  wider color scale.

(2021) for the determination of the faint signal from the disk region located further out.

## Appendix C: Parameters for Disk0 models

Table C.1 gives numerical values for the simulation of the axisymmetric, extended models Disk0 $\alpha$ 0, Disk0 $\alpha$ -1, and Disk0 $\alpha$ -2 described in Sect. 3.1.2. For all models with the same  $\alpha$ -index the intrinsic  $\Sigma Q'_{\phi}$ , and the  $\text{PSF}_G$  and  $\text{PSF}_{\text{AO}}$  convolved  $\Sigma Q_{\phi}$  values are given relative to the reference value  $Q'_{\phi, \text{ref}} = \Sigma Q'_{\phi}(r_{\text{in}} = 0.5 D_{\text{PSF}})$ .

The intrinsic  $\Sigma Q'_{\phi}/Q'_{\phi, \text{ref}}$  value for the Disk0 $\alpha$ 0 model with flat surface brightness (SB) plotted in Fig. 7 changes not much between  $r_{\text{in}} = 0$  and  $0.5 D_{\text{PSF}}$ . For the convolved signal there is almost no difference in  $\Sigma Q_{\phi}/Q'_{\phi, \text{ref}}$  for  $r_{\text{in}} \lesssim D_{\text{PSF}}$  and one cannot distinguish easily between different  $r_{\text{in}}$  cases. One can use the hole radius  $r_h(Q_{\phi})$  to distinguish between models with  $r_{\text{in}} =$

**Table C.1.** Results for the axisymmetric models Disk0 $\alpha$ 0, Disk0 $\alpha$ -1, and Disk0 $\alpha$ -2.

$r_{\text{in}}$ [mas]	$D_{\text{PSF}}$	$\Sigma Q'_\phi / Q'_{\phi,\text{ref}}$ intrinsic [%]	$\Sigma Q'_\phi / Q'_{\phi,\text{ref}}$ PSF <sub>G</sub> [%]	$\Sigma Q'_\phi / Q'_{\phi,\text{ref}}$ PSF <sub>AO</sub> [%]	$r(\max(Q_\phi))$ PSF <sub>AO</sub> [ $D_{\text{PSF}}$ ]	$r_h(Q_\phi)$ PSF <sub>AO</sub> [ $D_{\text{PSF}}$ ]
Disk0 $\alpha$ 0						
0	0	101	91.6	51.1	(2.70)	0.84
12.6	.5	$Q'_{\phi,\text{ref}}$	91.3	51.0	(2.70)	0.88
25.2	1	95.2	88.9	50.0	(2.73)	1.09
50.4	2	76.2	73.0	42.4	(2.98)	1.86
Disk0 $\alpha$ -1						
0	0	114	86.4	46.0	1.05	0.43
3.15	.125	111	86.4	46.0	1.05	0.43
6.30	.25	107	86.2	45.9	1.09	0.44
12.6	.5	$Q'_{\phi,\text{ref}}$	85.0	45.4	1.23	0.50
25.2	1	85.7	78.0	42.5	1.70	0.86
50.4	2	57.1	54.6	31.4	2.63	1.77
Disk0 $\alpha$ -2						
3.15	.125	171	81.1	40.0	0.77	0.34
6.30	.25	133	79.5	39.3	0.80	0.35
12.6	.5	$Q'_{\phi,\text{ref}}$	74.1	37.1	0.91	0.41
25.2	1	66.6	58.6	30.6	1.41	0.77
50.4	2	33.3	31.7	18.1	2.48	1.71
err		$\pm 0.3$	$\pm 0.2$	$\pm 0.2$	$\pm 0.01$	$\pm 0.01$

**Notes.** Results for the intrinsic azimuthal polarization  $\Sigma Q'_\phi$ , and the PSF<sub>G</sub> and PSF<sub>AO</sub> convolved values  $\Sigma Q_\phi$ , are listed for models with different inner radii  $r_{\text{in}}$ . The  $\Sigma Q'_\phi$  and  $\Sigma Q_\phi$  values for a given model type Disk0 $\alpha$ 0, Disk0 $\alpha$ -1, or Disk0 $\alpha$ -2 are normalized to the corresponding reference values  $Q'_{\phi,\text{ref}} = \Sigma Q'_\phi(r_{\text{in}} = 0.5D_{\text{PSF}})$ . Also given are the characteristic radii  $r(\max(Q_\phi))$  and  $r_h(Q_\phi)$  for PSF<sub>AO</sub> convolved models.

0.5  $D_{\text{PSF}}$  and 1.0  $D_{\text{PSF}}$ , but this would require for observational studies high quality data.

For the Disk0 $\alpha$ -2 the intrinsic  $\Sigma Q'_\phi / Q'_{\phi,\text{ref}}$  signal for a small cavity  $r_{\text{in}} = 0.125 D_{\text{PSF}}$  is much larger than the reference value, because the brightness increases rapidly towards the center (see Fig. 8). For the convolved signal  $\Sigma Q_\phi / Q'_{\phi,\text{ref}}$  the contributions from the central disk regions are strongly suppressed by polarimetric cancellation, but there is still a difference of about 20 % to 30 % between the model with  $r_{\text{in}} = 0.5 D_{\text{PSF}}$  and 1.0  $D_{\text{PSF}}$ . Also the radii  $r(\max(Q_\phi))$  and  $r_h(Q_\phi)$  are quite different between these two cases. For the Disk0 $\alpha$ -1 models these relative differences are intermediate between Disk0 $\alpha$ 0 and Disk0 $\alpha$ -2.

## Appendix D: Parameters for inclined disks

### Appendix D.1: RingI60 models

Results of the RingI60 simulations discussed in Sect. 3.2 are listed in Table D.1. All values for the integrated polarization parameters are normalized  $\Sigma X / \Sigma Q'_\phi$  to the intrinsic azimuthal polarization with  $X = \{Q_\phi, Q, P, |Q_\phi|, |U_\phi|, |Q|, |Q|\}$ .

The same normalization is applied to the five quadrant polarization values  $\Sigma X_{\text{xxx}} / \Sigma Q'_\phi$  with  $X_{\text{xxx}} = \{Q_{000}, Q_{090}, Q_{180}, U_{045}, U_{135}\}$ . Also given is the ratio between  $\Sigma |U_\phi| / \Sigma |Q_\phi|$  as measure for the  $Q_\phi \rightarrow U_\phi$  convolution cross-talk. The values in Table D.1 were numerically integrated for an aperture with  $r = 1.5''$ .

The first line in Table D.1 gives the values for the intrinsic model and the second line for a convolved but spatially

unresolved RingI60 model. For  $\Sigma |Q_\phi|$  and  $\Sigma |U_\phi|$  of the unresolved model the value  $(2/\pi)\Sigma Q$  is given, which follows from the analytic solution for the azimuthal integration of  $Q_\phi(\phi) = -Q \cos(2\phi)$  and  $U_\phi = -Q \sin(2\phi)$  of a “perfect” quadrant pattern for a PSF convolved point source with a polarization  $Q$ .

The  $\Sigma X / \Sigma Q'_\phi$ -values for the PSF<sub>G</sub> and PSF<sub>AO</sub> convolved models with different  $r_0$  correspond to the diagrams in Fig. 10, while the curves for the quadrant values  $\Sigma X_{\text{xxx}} / \Sigma Q'_\phi$  are shown in the upper panels of Fig. 13.

For the PSF<sub>AO</sub> convolved model with  $r_0 = 50.4$  mas not only values for an aperture with  $r = 1.5''$  are given, but also the splitted values for the disk region using a circular aperture with  $r = 0.2''$  and for the halo region using an annular aperture from  $r = 0.2''$  to  $1.5''$ . These values are given to support the discussion of the weak halo signal in Sect. 3.2.2 and Fig. 11.

The numerical integration of the polarization fluxes is affected for the smallest rings by the limited spatial sampling of 0.9 mas  $\times$  0.9 mas per pixel. This produces errors larger than two units in the last indicated digit for some tabulated values for the PSF<sub>G</sub> convolved model with  $r_0 = 3.15$  mas and for the PSF<sub>AO</sub> convolved model with  $r_0 = 6.3$  mas.

Smearing for PSF<sub>AO</sub> convolved models puts some flux outside of the aperture radius  $r = 1.5''$ . The strength of this effect follows from convolved small disk models  $r_0 \leq 201.6$  mas which give  $\Sigma Q / \Sigma Q'_\phi \approx 41.4$  % instead of the intrinsic value 42.1 %. For extended disks with  $r_0 > 200$  mas additional disk polarization is “lost” outside the aperture because of the convolution.

The differential Stokes quadrant values  $\Delta Q_{000}$ ,  $\Delta Q_{090}$ ,  $\Delta Q_{180}$ , and  $\Delta U_+$  are listed in Table D.2. They are expressed as ratio relative to  $\Sigma Q_\phi$  for the RingI60 models with different  $r_0$  based on the values given in Table D.1. They are derived according to the Eqs. 15 and 17 and are also plotted in the lower panels of Fig. 13.

### Appendix D.2: DiskI60 models

Table D.3 gives integrated polarization parameters for the extended,  $i = 60^\circ$  inclined disk models DiskI60 $\alpha$ 0, DiskI60 $\alpha$ -1, and DiskI60 $\alpha$ -2 for different cavity sizes  $r_{\text{in}}$ . The outer disk radius is in all cases  $r_{\text{out}} = 100.8$  mas. The model with  $r_{\text{in}} = 0.5 D_{\text{PSF}}$  (12.6 mas) represents for all models with the same  $\alpha$ -index the reference value  $Q'_{\phi,\text{ref}} = \Sigma Q'_\phi(r_{\text{in}} = 0.5 D_{\text{PSF}})$  as in Table C.1.

The model parameters  $\alpha$ ,  $r_{\text{in}}$ , and  $r_{\text{out}}$  for the inclined disks corresponds to Table C.1 for pole-on models, except for the disk inclination. Therefore, the intrinsic polarization values  $\Sigma Q'_\phi / Q'_{\phi,\text{ref}}$  are practically the same apart for some numerical sampling errors for disks with bright ( $\alpha = -2$ ) and barely resolved ( $r_{\text{in}} < 0.5 D_{\text{PSF}}$ ) inner regions. For the selected disk inclination the ratio  $\Sigma Q' / \Sigma Q'_\phi$  is for all intrinsic models 0.421. The Stokes value  $\Sigma Q$  is not changed by the convolution  $\Sigma Q / \Sigma Q' = 1$ , but for the PSF<sub>AO</sub> convolved results this value is  $\Sigma Q / \Sigma Q' = 0.98$  because a small amount of the smeared  $Q$ -signal is located outside the used aperture with  $r = 1.5''$ .

The values for  $\Sigma Q_\phi$ ,  $\Sigma Q$  ( $\approx \Sigma Q' = 0.421 \Sigma Q'_\phi$ ) and  $\Sigma P$  are plotted for convolved DiskI60 $\alpha$ -2 models in Fig. 15 as function of  $r_{\text{in}}$ . Of interest is the ratio  $\Sigma Q_\phi / \Sigma Q$ , which depends on the cancellation of the  $Q_\phi$  signal in particular for bright, barely resolved inner disk regions. Table D.3 gives the values for this dependence also for the models DiskI60 $\alpha$ 0 and DiskI60 $\alpha$ -1.

The convolved polarized flux  $\Sigma P$  differs for DiskI60 models significantly from  $\Sigma Q_\phi$ , unlike for the pole-on models where  $\Sigma P \approx \Sigma Q_\phi$ . The polarized flux  $\Sigma P$  represents a complex mix

**Table D.1.** Results for RingI60 models with different  $r_0$ .

$r_0$ mas	integrated parameters $\Sigma X/\Sigma Q'_\phi$						cross talk		quadrant values $\Sigma X_{xxx}/\Sigma Q'_\phi$				note
	$\Sigma Q_\phi$ [%]	$\Sigma Q$ [%]	$\Sigma P$ [%]	$\Sigma  Q_\phi $ [%]	$\Sigma  U_\phi $ [%]	$\Sigma  Q $ [%]	$\Sigma  U $ [%]	$\Sigma  U_\phi $ [%]	$Q_{000}$ [%]	$Q_{090}$ [%]	$Q_{180}$ [%]	$U_{045}$ [%]	$U_{135}$ [%]
intrinsic RingI60 model													
all	100	42.1	100	100	0	70.3	56.6	0	-0.7	+28.1	-13.4	-4.1	+24.3
unresolved RingI60 model													
unres.	0	42.1	42.1	26.8 <sup>a</sup>	26.8 <sup>a</sup>	42.1	0	1	+10.5	+10.5	+10.5	0	0
PSF <sub>G</sub> convolved													
3.15 <sup>b</sup>	1.5	42.1	42.6	27.1	27.1	42.1	5.1:	1.00	+10.0	+11.1	+10.4	+1.1	+1.5
6.3	5.7	42.1	43.7	28.0	27.7	42.1	10.0	0.99	+9.2	+11.9	+9.5	+1.9	+3.1
12.6	19.2	42.1	47.4	31.9	28.5	42.1	18.7	0.89	+7.1	+14.3	+5.7	+2.7	+6.7
25.2	51.3	42.1	62.8	52.7	26.1	47.8	32.0	0.50	+2.1	+20.7	-1.6	+1.4	+13.4
50.4	83.2	42.1	86.6	83.4	18.0	62.8	46.6	0.22	-0.3	+25.7	-9.0	-2.0	+20.4
100.8	95.7	42.1	98.4	95.7	8.5	68.3	53.9	0.09	-0.6	+27.4	-12.2	-3.6	+23.3
201.6	98.7	42.1	98.9	98.7	3.2	69.6	55.8	0.03	-0.7	+28.0	-13.3	-3.9	+24.0
PSF <sub>AO</sub> convolved													
6.3 <sup>b</sup>	2.5	41.2	41.7	26.6	26.6	41.2	4.8	1.00	+9.5	+11.3	+10.0	+1.0	+1.7
12.6	8.4	41.4	43.2	28.1	27.0	41.4	9.2	0.96	+8.4	+12.4	+8.9	+1.3	+3.2
25.2	22.3	41.4	48.0	35.1	25.9	42.1	15.5	0.74	+6.5	+14.9	+5.5	+1.1	+6.5
50.4	40.4	41.4	58.7	49.5	22.4	47.7	23.7	0.45	+4.5	+18.0	+1.0	0.0	+10.6
disk	40.3	29.4	46.7	41.8	14.8	35.7	22.9	0.35	+1.5	+15.0	-1.9	0.0	+10.4
halo	0.1	12.0	12.0	7.7	7.7	12.0	0.9	1.00	+3.0	+3.0	+3.0	+0.1	> 0.2''
100.8	55.9	41.4	70.2	63.7	17.9	54.3	32.5	0.28	+3.2	+20.5	-2.8	-1.2	+14.0
201.6	63.9	41.1	76.1	71.1	13.8	57.4	37.9	0.19	+2.7	+21.6	-4.9	-1.9	+15.9
403.2 <sup>c</sup>	68.6	40.9	78.1	73.9	10.1	57.9	40.7	0.14	+2.2	+22.4	-6.1	-2.0	+17.2
806.4 <sup>c</sup>	74.9	39.8	79.6	76.4	8.4	57.8	43.1	0.11	+0.9	+23.4	-7.9	-2.0	+18.7

**Notes.** The table lists the integrated polarization  $\Sigma X$  and quadrant polarization parameters  $\Sigma X_{xxx}$ , and the  $\Sigma |U_\phi|/\Sigma |Q_\phi|$  convolution cross talk ratios for RingI60 models with different  $r_0$  convolved with PSF<sub>G</sub> and PSF<sub>AO</sub>. All  $\Sigma X$  and  $\Sigma X_{xxx}$  values are normalized by the intrinsic polarization  $\Sigma Q'_\phi = 100\%$ . <sup>(a)</sup> Analytical result for an unresolved model convolved with an extended PSF, <sup>(b)</sup> small models with uncertainties larger than two unit in the last digit for some parameters because of the limited numerical sampling for the innermost region, <sup>(c)</sup> large disks, for which more than 2 % of  $\Sigma Q$  falls outside of the  $r < 1.5''$  integration region.

**Table D.2.** Differential quadrant values  $\Delta Q_{xxx}$  and  $\Delta U_+$  for RingI60 models.

$r_0$ mas	$\Delta Q_{xxx}/\Sigma Q_\phi$			$\Delta U_+/\Sigma Q_\phi$	
	$Q_{000}$	$Q_{090}$	$Q_{180}$		
intrinsic RingI60 model					
all	-0.112	+0.176	-0.239	+0.284	
convolved with Gaussian PSF <sub>G</sub>					
12.6	-0.178	+0.197	-0.251	+0.208	
25.2	-0.164	+0.198	-0.236	+0.238	
50.4	-0.130	+0.182	-0.235	+0.269	
100.8	-0.116	+0.176	-0.237	+0.281	
convolved with extended PSF <sub>AO</sub>					
12.6	-0.232	+0.244	-0.173	+0.226	
25.2	-0.173	+0.204	-0.217	+0.241	
50.4	-0.145	+0.189	-0.231	+0.262	
100.8	-0.128	+0.182	-0.235	+0.272	
201.6	-0.119	+0.177	-0.237	+0.279	
403.2	-0.117	+0.177	-0.238	+0.280	
806.4	-0.121	+0.180	-0.238	+0.276	

**Notes.** The differential quadrant values are normalized to  $\Sigma Q_\phi$  of the corresponding RingI60 models characterized by  $r_0$  and the used convolution PSF<sub>G</sub> or PSF<sub>AO</sub>. The intrinsic values do not depend on  $r_0$ .

(Eq. 10) of the azimuthal polarization  $Q_\phi$  and  $U_\phi$  or of the Stokes  $Q$  and  $U$  components.

## Appendix E: ZP-corrected disk models

### Appendix E.1: RingI60 model with $r_0 = 100.8$ mas

Table E.1 lists polarization parameters  $Q_\phi$ ,  $Q$ ,  $P$  and Stokes  $Q$  quadrant values  $Q_{000}$ ,  $Q_{090}$ ,  $Q_{180}$  for the RingI60 models with  $r_0 = 100.8$  mas. Results for many combination of used regions for the zp-correction  $\Sigma_{zp}$  and integration regions  $\Sigma_{int}$  are given as described in Sects. 4.3.1 and 4.3.2 and partly shown in Figs. 18 and 19.

The integration apertures are defined as follows: round apertures  $\Sigma$  with  $r \leq 1.5''$  for the entire system and  $\Sigma_1$  with  $r \leq 0.027''$  for the star, and annular aperture  $\Sigma_2$  with  $0.027'' < r \leq 0.2''$  for the disk region and  $\Sigma_3$  with  $0.2'' < r \leq 1.5''$  for the halo. There is  $\Sigma_1 + \Sigma_2 + \Sigma_3 = \Sigma$ . All polarization values in Table E.1 are given relative to  $\Sigma Q'_\phi$ .

The first line gives values for the intrinsic model which are identical to the first line in Table D.3, where also the Stokes  $U$  quadrant values  $\Sigma U'_{045}$  and  $\Sigma U'_{135}$  are given. For the intrinsic model the values for  $\Sigma_2$  are identical to the system values  $\Sigma$ , because the polarization signal in  $\Sigma_1$  and  $\Sigma_3$  are zero.

The lines 2 to 5 in Table E.1 list the polarization for the PSF<sub>AO</sub> convolved RingI60 model for different integration re-

**Table D.3.** Results for the DiskI60 $\alpha$ 0, DiskI60 $\alpha$ -1, and DiskI60 $\alpha$ -2 models.

$r_{\text{in}}$ [mas]	$D_{\text{PSF}}$	intrinsic		PSF <sub>G</sub> conv.		PSF <sub>AO</sub> conv.	
		$\Sigma Q'_\phi$ [%]	$\Sigma Q'$ [%]	$\Sigma Q_\phi$ [%]	$\Sigma P$ [%]	$\Sigma Q'_\phi$ [%]	$\Sigma P$ [%]
<b>DiskI60<math>\alpha</math>0</b>							
0	0	102	42.8	85.9	88.0	45.6	62.2
12.6	0.5	$Q'_{\phi,\text{ref}}$	42.1	85.8	87.5	45.5	61.7
25.2	1	95.6	40.0	83.9	85.3	44.7	59.8
50.4	2	76.2	32.1	70.2	71.1	38.4	50.1
<b>DiskI60<math>\alpha</math>-1</b>							
0	0	114	47.4	78.5	85.5	40.2	62.2
3.15	0.125	111	46.9	78.5	84.8	40.2	61.5
6.30	0.25	107	45.0	78.4	83.5	40.1	60.1
12.6	0.5	$Q'_{\phi,\text{ref}}$	42.1	77.5	81.0	39.7	57.6
25.2	1	85.6	36.0	72.4	74.2	37.5	51.8
50.4	2	57.2	24.1	52.3	53.0	28.3	37.2
<b>DiskI60<math>\alpha</math>-2</b>							
3.15	0.125	167	73.7	69.1	101	33.6	80.6
6.30	0.25	135	55.6	68.2	84.4	33.2	64.5
12.6	0.5	$Q'_{\phi,\text{ref}}$	42.1	64.5	71.6	31.5	52.3
25.2	1	66.6	28.0	53.2	55.2	26.6	38.5
50.4	3	33.4	14.1	30.4	30.8	16.3	21.5

**Notes.** The table lists integrated azimuthal polarization  $\Sigma Q'_\phi/Q'_{\phi,\text{ref}}$  for the intrinsic models, and  $\Sigma Q_\phi/Q'_{\phi,\text{ref}}$  and the polarization  $\Sigma P/Q'_{\phi,\text{ref}}$  for the models convolved with the Gaussian PSF<sub>G</sub> and PSF<sub>AO</sub>. The reference values are defined by  $Q'_{\phi,\text{ref}} = \Sigma Q'_\phi = 100$  % for the model with  $r_{\text{in}} = 0.5 D_{\text{PSF}}$  (12.6 mas). The values for the models DiskI60 $\alpha$ -2 are plotted in Fig. 15.

gions  $\Sigma_i$ . The values for  $\Sigma$  are identical to entries in the fourth last line of Table D.3, which gives also the Stokes  $U$  quadrant values  $\Sigma_2 U_{045}/\Sigma Q'_\phi = -1.2$  % and  $\Sigma_2 U_{135}/\Sigma Q'_\phi = +14.0$  %. The values for the halo are  $\Sigma_3 U_{045}/\Sigma Q'_\phi = +0.2$  %,  $\Sigma_3 U_{135}/\Sigma Q'_\phi = +0.3$  %, while they are zero for the  $\Sigma_1$  region. The values for  $\Sigma_i = \Sigma_1, \Sigma_2$ , and  $\Sigma_3$  show how the convolution changes the distribution of the polarization radially.

The following lines in Table E.1 give the same parameters as for the convolved model, but after zp-correction using different reference regions  $\Sigma_{\text{zp}} = \Sigma, \Sigma_1, \Sigma_2, \Sigma_{2+3}$  and  $\Sigma_3$ . It is obvious that the different zp-correction offsets change strongly the values for  $\Sigma_i Q$ ,  $\Sigma_i P$ , and the Stokes quadrants  $\Sigma_i Q_{\text{xxx}}$ .

An important result is, that the azimuthal polarization  $\Sigma_i Q^z$  is practically not changed by the applied correction offsets. Also the Stokes  $U$  quadrant values are not changed because only offsets for the Stokes  $Q$  polarization component are applied in these simulations. The  $Q$  quadrant values  $\Sigma_3 Q^z_{000}, \Sigma_3 Q^z_{090}$ , and  $\Sigma_3 Q^z_{180}$  for the halo region have after a zp-correction practically the same value, because all quadrants are offset by the same amount. The same also applies roughly for the Stokes  $Q^z$  quadrants integrated in the stellar aperture  $\Sigma_i = \Sigma_1$ .

#### Appendix E.2: ZP-corrected model RingI60 with $r_0 = 403.2$ mas

Table E.2 gives polarization parameters for the very large RingI60 model with  $r_0 = 403.2$  mas of Fig. 20 in Sect. 4.3.3, and they quantify the impact of different zp-correction for a disk with  $r_0$  similar to the radius of the PSF speckle ring of an AO-system.

**Table E.1.** Results for the RingI60 models with  $r_0 = 100.8$  mas using different zp-corrections.

$\Sigma_{\text{zp}}$	$\Sigma_{\text{int}}$	$\Sigma_{i'} X/\Sigma Q'_\phi$ [%]	$P$	$\Sigma_{i'} Q_{\text{xxx}}/\Sigma Q'_\phi$ [%]			
$\Sigma_i$	$\Sigma_{i'}$	$Q_\phi$	$Q$	$Q_{000}$	$Q_{090}$	$Q_{180}$	
intrinsic parameters							
$\Sigma$		100.	+42.1	100.	-0.7	+28.1	-13.4
PSF <sub>AO</sub> convolved parameters							
$\Sigma$		55.9	+41.4	70.2	+3.2	+20.5	-2.8
$\Sigma_1$		0.2	-0.2	0.3	0.0	0.0	-0.2
$\Sigma_2$		55.2	+29.3	57.5	+0.3	+17.3	-5.6
$\Sigma_3$		0.5	+12.2	12.4	+3.0	+3.2	+3.0
$\Sigma_{\text{zp}}$ : whole system							
$\Sigma$	$\Sigma$	55.8	0.0	82.6	-6.6	+9.6	-13.6
$\Sigma$	$\Sigma_1$	0.2	-18.4	18.4	-4.2	-4.9	-5.1
$\Sigma$	$\Sigma_2$	55.2	+18.1	61.7	-2.3	+14.4	-8.6
$\Sigma$	$\Sigma_3$	0.5	+0.3	2.4	0.0	+0.2	0.0
$\Sigma_{\text{zp}}$ : central star							
$\Sigma_1$	$\Sigma$	55.8	+41.8	70.4	+3.4	+20.6	-2.6
$\Sigma_1$	$\Sigma_1$	0.2	0.0	0.4	0.0	0.0	-0.1
$\Sigma_1$	$\Sigma_2$	55.2	+29.7	57.5	+0.3	+17.3	-5.5
$\Sigma_1$	$\Sigma_3$	0.5	+12.4	12.5	+3.0	+3.2	+3.0
$\Sigma_{\text{zp}}$ : disk							
$\Sigma_2$	$\Sigma$	55.8	-66.3	140.	-22.3	-7.7	-31.1
$\Sigma_2$	$\Sigma_1$	0.2	-47.6	47.6	-11.0	-12.7	-12.9
$\Sigma_2$	$\Sigma_2$	55.1	0.0	73.2	-6.6	+9.6	-13.4
$\Sigma_2$	$\Sigma_3$	0.5	-18.7	18.9	-4.8	-4.6	-4.8
$\Sigma_{\text{zp}}$ : disk and halo							
$\Sigma_{2+3}$	$\Sigma$	55.8	-32.9	109.	-14.4	+1.1	-22.3
$\Sigma_{2+3}$	$\Sigma_1$	0.2	-32.8	32.9	-7.6	-8.8	-8.9
$\Sigma_{2+3}$	$\Sigma_2$	55.1	+9.1	67.1	-4.4	+12.0	-10.9
$\Sigma_{2+3}$	$\Sigma_3$	0.5	-9.1	9.5	-2.4	-2.2	-2.4
$\Sigma_{\text{zp}}$ : halo							
$\Sigma_3$	$\Sigma$	55.8	-1.2	83.3	-6.8	+9.3	-13.9
$\Sigma_3$	$\Sigma_1$	0.2	-18.9	18.9	-4.3	-5.0	-5.2
$\Sigma_3$	$\Sigma_2$	55.2	+17.7	61.9	-2.4	+14.3	-8.6
$\Sigma_3$	$\Sigma_3$	0.5	0.0	2.5	-0.1	+0.1	-0.1

**Notes.** The table lists integrated polarization  $X = Q_\phi, Q, P$  and quadrant polarization values  $Q_{\text{xxx}}$  for different integration regions  $\Sigma_{\text{int}}$  of the PSF<sub>AO</sub> convolved model, and for corresponding zp-corrected models using different zp-correction regions  $\Sigma_{\text{zp}}$ . The parameters  $\Sigma_{i'} X$  and  $\Sigma_{i'} X_{\text{xxx}}$  for the table columns stand for intrinsic values  $X = X'$  and  $Q_{\text{xxx}} = Q'_{\text{xxx}}$ , for convolved values  $X$  and  $Q_{\text{xxx}}$ , and for values  $X^{zi}$  and  $Q^{zi}_{\text{xxx}}$  with zp-corrections based on region  $\Sigma_{\text{zp}} = \Sigma_i$ , integrated in region  $\Sigma_{i'}$  (Table A.2). All values are normalized to the intrinsic azimuthal polarization  $\Sigma Q'_\phi$ .

The first line in Table E.2 gives values identical to the second last line of Table D.1, where also the  $\Sigma U_{\text{xxx}}$  quadrant parameters for this model are given. The values for  $\Sigma_{\text{int}} = \Sigma_1, \Sigma_2$ , and  $\Sigma_3$  give the radial distribution of the PSF<sub>AO</sub>-convolved polarization signal. The integration regions are defined by the circular aperture  $r \leq 0.1''$  for  $\Sigma_1$  representing the star or the coronagraphic mask, and by the annular apertures  $0.1'' < r \leq 0.5''$  for  $\Sigma_2$  and  $0.5'' < r \leq 1.5''$  for  $\Sigma_3$ . For the Stokes  $U$  quadrants there is  $\Sigma_2 U_{045}/\Sigma Q'_\phi = -2.5$  % and  $\Sigma_2 U_{135}/\Sigma Q'_\phi = +17.2$  %, the corresponding  $\Sigma_1$  values are zero and the  $\Sigma_3$  values are the differences

**Table E.2.** Comparison for different zp-corrections for the extended model RingI60 with  $r_0 = 403.2$  mas.

$\Sigma_{\text{zp}}$	$\Sigma_{\text{int}}$	$\Sigma_{i'}X/\Sigma Q'_\phi$ [%]		$\Sigma_{i'}Q_{xxx}/\Sigma Q'_\phi$			
$\Sigma_i$	$\Sigma_{i'}$	$Q_\phi$	$Q$	$P$	$Q_{000}$	$Q_{090}$	$Q_{180}$
PSF <sub>AO</sub> convolved parameters							
$\Sigma$		68.6	+40.9	78.1	+2.2	+22.4	-6.1
$\Sigma_1$		0.0	+0.2	0.2	+0.1	0.0	0.0
$\Sigma_2$		65.9	+31.9	68.6	+0.5	+19.5	-7.7
$\Sigma_3$		2.7	+8.9	9.6	+1.7	+2.8	+1.6
$\Sigma_{\text{int}} = \Sigma_2$ parameters for different $\Sigma_{\text{zp}}$							
$\Sigma$	$\Sigma_2$	65.9	+26.0	67.5	-0.9	+18.1	-8.2
$\Sigma_1$	$\Sigma_2$	65.9	+31.9	68.6	+0.5	+19.5	-7.7
$\Sigma_2$	$\Sigma_2$	65.9	0.0	83.9	-7.2	+11.6	-16.0
$\Sigma_{2+3}$	$\Sigma_2$	65.9	+14.1	74.2	-3.8	+15.1	-12.3
$\Sigma_3$	$\Sigma_2$	65.9	+25.0	68.0	-1.1	+17.8	-9.5

**Notes.** The upper part gives results for the PSF<sub>AO</sub> convolved model and the lower part the  $\Sigma_2$  values after zp-correction based on different regions  $\Sigma_{\text{zp}}$  for the models shown in Fig. 20. All values are normalized relative to the intrinsic azimuthal polarization  $\Sigma Q'_\phi$ .

between the  $\Sigma$  and  $\Sigma_2$  values. The distribution of the intensity  $\Sigma_i I / \Sigma I'_s$  in the PSF<sub>AO</sub> convolved images are 66.2 %, 13.5 % and 18.1 % for the integration regions  $\Sigma_1$ ,  $\Sigma_2$  and  $\Sigma_3$ , respectively. The intrinsic disk signal is  $\Sigma I'_d / \Sigma I'_s = 1$  % and  $\Sigma Q'_\phi / \Sigma I'_s = 0.1$  %.

The last five lines in Table E.2 give the polarization values for the disk aperture  $\Sigma_i = \Sigma_2$  after zp-correction in different apertures  $\Sigma_{\text{zp}}$ . The  $\Sigma_2 U_{xxx}$  values given above for the convolved model are not changed by a Stokes  $Q$  zp-correction.

The ideal case is the zp-correction using the unpolarized star signal in  $\Sigma_{\text{zp}} = \Sigma_1$ , which yields the same result as the (initial) PSF<sub>AO</sub> convolved model. For coronagraphic observations a zp-correction including the  $\Sigma_1$  region is not possible. The  $\Sigma_{\text{zp}} = \Sigma_2$  correction sets the Stokes  $\Sigma_2 Q$  signal to zero and this introduces for this model a very large polarization offset. Using the halo for the zp-correction  $\Sigma_{\text{zp}} = \Sigma_3$  is practically equivalent to the case  $\Sigma_{\text{zp}} = \Sigma$  for a total system correction, which is a good approach to account for undefined instrumental polarization effects, which may be re-calibrated with aperture polarimetry. A  $\Sigma$  or system zp-correction means also  $\Sigma Q^z = 0 \approx \Sigma_3 Q^z$  and  $\Sigma_2 Q^z \approx -\Sigma_1 Q^z$  (Table E.1). Measuring the halo polarization signal can be problematic, if the halo signal is noisy. A zp-correction based on a region including disk and halo regions  $\Sigma_{\text{zp}} = \Sigma_{2+3}$  is also problematic because this depends on the PSF-convolution.

For all  $\Sigma_{\text{zp}}$  regions practically the same azimuthal polarization  $\Sigma_2 Q_\phi$  is obtained, emphasizing the important invariance of  $\Sigma Q_\phi$  with respect to polarization offset. Of course, this property is based on the use of an axisymmetric PSF and axisymmetric integration regions in the simulations. Contrary to this, the integrated polarization  $\Sigma_2 P$  changes by the use of different integration region by up to about 20 %, and this does not include the problem of the noise bias, which might be very significant for observations of extended, low SB scattering regions.

### Appendix E.3: Center corrected DiskI60 $\alpha$ -2 models

The Table E.3 gives numerical values for the PSF<sub>AO</sub> convolved DiskI60 $\alpha$ -2 models, and for center corrected  $\Sigma_{\text{zp}} = \Sigma_0$  and system corrected  $\Sigma_{\text{zp}} = \Sigma$  models. For the size of the inner disk cavity the two cases  $r_{\text{in}} = 0.125 D_{\text{PSF}}$  (3.15 mas) and  $r_{\text{in}} = 0.5 D_{\text{PSF}}$

**Table E.3.** Comparison of values for two compact DiskI60 $\alpha$ -2 models without and with two types of zp-correction.

$\Sigma_{\text{int}}$	$\Sigma_{i'}X/\Sigma Q'_{\phi,\text{ref}}$ [%]	$\Sigma_{i'}Q_{xxx}/\Sigma Q'_{\phi,\text{ref}}$ [%]					
$\Sigma_{i'}$	$Q_\phi$	$Q$	$Q_{000}$	$Q_{090}$	$Q_{180}$	$U_{045}$	$U_{135}$
cavity size $r_{\text{in}} = 0.125 D_{\text{PSF}}$							
intrinsic disk							
$\Sigma$	167.	73.7	-1.2	+47.0	-22.3	-6.8	+40.5
convolved disk							
$\Sigma$	33.7	72.5	+12.6	+25.0	+10.9	+1.0	+9.6
$\Sigma_{1+2}$	33.6	51.6	+7.4	+19.7	+5.7	+0.9	+9.5
$\Sigma_3$	0.1	20.9	+5.2	+5.3	+5.2	+0.1	+0.1
$\Sigma_{\text{zp}} = \Sigma$ : system corrected disk							
$\Sigma$	33.6	0.0	-4.6	+6.0	-8.1	+1.0	+9.6
$\Sigma_{1+2}$	33.5	0.0	-4.6	+6.0	-8.1	+0.9	+9.5
$\Sigma_3$	0.1	0.0	0.0	0.0	0.0	+0.1	+0.1
$\Sigma_{\text{zp}} = \Sigma_0$ : center corrected disk							
$\Sigma$	33.6	42.7	+5.6	+17.2	+3.1	+1.3	+9.9
$\Sigma_{1+2}$	33.5	30.4	+2.5	+14.1	0.0	+1.1	+9.7
$\Sigma_3$	0.1	12.3	+3.1	+3.1	+3.1	+0.2	+0.2
cavity size $r_{\text{in}} = 0.5 D_{\text{PSF}}$							
intrinsic disk							
$\Sigma$	$Q'_{\phi,\text{ref}}$	42.1	-0.7	+28.1	-13.4	-4.1	+24.3
convolved disk							
$\Sigma$	31.5	41.4	+5.6	+16.4	+3.2	+0.4	+8.5
$\Sigma_{1+2}$	31.4	29.4	+2.6	+13.4	+0.2	+0.3	+8.4
$\Sigma_3$	0.1	12.0	+3.0	+3.0	+3.0	+0.1	+0.1
$\Sigma_{\text{zp}} = \Sigma$ : system corrected disk							
$\Sigma$	31.4	0.0	-4.2	+5.6	-7.6	+0.4	+8.5
$\Sigma_{1+2}$	31.5	0.0	-4.2	+5.6	-7.6	+0.3	+8.4
$\Sigma_3$	-0.1	+0.1	0.0	0.0	0.0	+0.1	+0.1
$\Sigma_{\text{zp}} = \Sigma_0$ : center corrected disk							
$\Sigma$	31.5	37.5	+4.7	+15.4	+2.2	+0.5	+8.7
$\Sigma_{1+2}$	31.4	26.6	+2.0	+12.7	-0.5	+0.4	+8.5
$\Sigma_3$	0.1	10.9	+2.7	+2.7	+2.7	+0.1	+0.2

**Notes.** Result for models with  $r_{\text{in}} = 0.125 D_{\text{PSF}}$  (upper part) and  $r_{\text{in}} = 0.5 D_{\text{PSF}}$  (lower part) are given using different integration regions  $\Sigma_{\text{int}}$ . Values for the intrinsic and PSF<sub>AO</sub> convolved models are given, and for models zp-corrected for the whole system and the center. All values are normalized to  $Q'_{\phi,\text{ref}} = \Sigma Q'_\phi = 100$  % for the model with  $r_{\text{in}} = 0.5 D_{\text{PSF}}$  (12.6 mas). The models for  $r_{\text{in}} = 0.125 D_{\text{PSF}}$  (3.15 mas) are plotted in Fig. 21.

(12.6 mas) were selected. The latter case is the reference disk with  $\Sigma Q'_\phi = Q_{\text{ref}} = 100$  % for the intrinsic azimuthal polarization. For the model with the small cavity the intrinsic polarization  $\Sigma Q'_\phi = 167$  % is much larger when compared to  $Q_{\text{ref}}$ , but most of the additional azimuthal polarization is not resolved (see Table D.3). Also the  $\Sigma Q$  signal is high for the  $r_{\text{in}} = 0.125 D_{\text{PSF}}$  model and Fig. 21 shows the PSF<sub>AO</sub> convolved polarization maps  $X(x, y)$  for  $X = \{Q, U, Q_\phi, U_\phi\}$ , and the resulting maps after a system zp-correction  $X^z$  and a center zp-correction  $X^{\text{ex}}$ . The integration regions  $\Sigma_i$  are defined by round apertures  $r \leq 1.5''$  for the whole system  $\Sigma$ , and  $r \leq 0.2''$  for the star and disk region  $\Sigma_{1+2}$ , and by an annular aperture  $0.2'' < r \leq 1.5''$  for the halo region  $\Sigma_3$ .

The system zp-correction  $\Sigma_{\text{zp}} = \Sigma$  sets the  $\Sigma Q$  signal to zero and this reduces for both  $r_{\text{in}}$  cases strongly the  $\Sigma Q_{xxx}$  quadrant

values. The center corrected values for the disk with the small cavity  $r_{\text{in}} = 0.125D_{\text{PSF}}$  are very similar (within 15 %) to the case of the reference model with a cavity size of  $r_{\text{in}} = 0.5D_{\text{PSF}}$ . Thus, the center zp-correction accounts practically for the Stokes  $Q$  polarization offset introduced by the unresolved central region. This correction offset is  $-\langle q_0 \rangle \Sigma I / Q'_{\phi,\text{ref}} = 29.8 \%$  for the model with  $r_{\text{in}} = 0.125D_{\text{PSF}}$  and 3.9 % for  $r_{\text{in}} = 0.5D_{\text{PSF}}$ . The quadrant values for  $U_{045}$  and  $U_{135}$  are practically unchanged for a zp-correction of a Stokes  $Q$  polarization.